Small-scale Deformation and Fracture of Hard Biomaterials

Thesis by
Ottman A. Tertuliano

In Partial Fulfillment of the Requirements for the
Degree of
Doctor of Philosophy

CALIFORNIA INSTITUTE OF TECHNOLOGY
Pasadena, California

2019
Defended October 2, 2018

Ottman A. Tertuliano
ORCID: 0000-0003-0524-3944

ACKNOWLEDGEMENTS

We are constantly asked to overcome obstacles in life. I believe the people around us are why we progress. I have been immensely fortunate to have had such positive support.

To Dr. Elon Terrell and Dr. Emil Sandoz-Rosado, I am grateful for being granted a chance to learn from you. Julia, you have been an incredible advisor and mentor. You are constantly breaking barriers, and I admire your dedication to providing so many people the opportunity to explore their scientific curiosity. To Christy, thanks for making me feel like I belong. To the KNI staff, particularly Matt, Melissa, Tiffany and Jennifer, I truly appreciate everything you've taught me. To the Greer group, you have made my time at Caltech incredibly fun, and I thank you all for being my work family. David, Lucas, Viki, Eric, Wendy, Rachel, and Zach, thank you for being amazing resources and friends when I started in the group. Bryce thank you for being patient with me; you've taught me more than you probably realize. Carlos and Xioaxing, I appreciate the time you spent helping me academically and personally. Dylan, Daryl, Arturo, Namita, and Ryan, thank you for keeping me sane. Stephanie, Kyle, Sarah, and Monique, I would be lost if I did not look up and start fulfilling my responsibilities; you've also been great friends along the way.

Carol, you are one of the most amazing and resilient people I have met and will likely have the pleasure to meet. Jon and Asher, thank you for simultaneously amazing roommates, friends, and family. Alessandro and Tiffany, thank you for taking care of me.

Mamma, papa, Haqq, and Iya Zikir, I will never stop thanking you. Merci pour tout.

ABSTRACT

Structural materials engineering often aims to realize materials that are simultaneously strong, tough, and lightweight — a combination classically considered mutually exclusive. Natural composite materials such as bone exhibit a combination of these properties far exceeding that of their constituents, a feat generally credited to their hierarchical structure — all the way down the nanoscale. To date, a quantitative description of how this property combination arises in such microstructurally complex materials has remained elusive due to challenges in experimentally isolating and probing the salient deformation and toughening mechanisms at the micro and nanometer scales — length scales on the order the constituents of many natural composites.

In this thesis, we first investigate the site-specific nanoscale structure of human bone using transmission electron microscopy. We show the presence of previously undiscovered disordered arrangement of collagen and mineral — alongside a well known ordered structure — within the trabecular architecture of bone. We perform micro- and nano-mechanical compression experiments to probe strength and deformation of each of these microstructures, revealing a size-dependent strength of bone attributed to the limited number of failure-initiating critical defects (e.g pores) in the small-scale samples relative to macro-scale tissue.

Unlike experiments for investigating strength at small-scales, fracture experiments are standardized for the macroscale. To address this, we developed an in situ SEM/nanoindenter methodology that enables 3-point bending fracture experiments with observation and measurement of crack growth and toughening behavior at nano and micrometer scales. Using this technique, we discuss the crack initiation and growth toughness arising primarily from the underlying fibril microstructure in bone. In the context of a crack growth resistance, we describe a transition in the toughening behavior of bone originating from different levels of hierarchy. Given its versatility, this experimental technique establishes a platform for understanding the coupling between structure and fracture behavior of micron-sized materials.

PUBLISHED CONTENT AND CONTRIBUTIONS

[1] Tertuliano, O. A. & Greer, J. R. The nanocomposite nature of bone drives its strength and damage resistance. *Nature Materials* **15**, 1195–1202 (2016). URL http://www.nature.com/doifinder/10.1038/nmat4719.
O.A.T performed the experiments, analyzed the data, and developed model and wrote the manuscript.

[2] Tertuliano, O. A., Edwards, B. W., Meza, L., Deshpande, V. & Greer, J. R. Microscale 3-point bending fracture experiments reveal the emergent damage tolerance of bone. *in preparation*
O.A.T performed the experiments, analyzed the data, and wrote the manuscript.

TABLE OF CONTENTS

LIST OF ILLUSTRATIONS

LIST OF TABLES

Chapter 1

INTRODUCTION

1.1 Achieving Strength and Toughness

A common aim of structural materials engineering is to design materials that are simultaneously strong and tough, commonly denoted "damage tolerance" [1]. Strength is the material's stress that characterizes resistance to non-recoverable deformation. In the case of metals this is often defined as the onset of plasticity; in ceramics it represents the maximum attainable stress of the material. Fracture toughness characterizes the material's energetic resistance to growing an existing crack. The classical mutual exclusivity of these properties is exemplified in a common "workhorse" ceramic like alumina which is to be stronger than tougher engineering metals like aluminum alloys. From a materials engineering perspective, we often resolve this by turning to composite materials and employing "toughening" strategies, increasing the energetic cost for a crack to propagate through a material. To understand toughening strategies we first provide a very brief description of crack growth criteria in linear elastic materials.

A Brief Description of Fracture Toughness

Fracture mechanics has its origins in Griffith theory, stating that the toughness of a material under loading is a competition between the decrease in stored elastic energy and energy gained from creating new surfaces from a pre-existing crack [2]. This toughness defined as a strain energy release rate $G = 2\gamma$ — where γ is the surface energy — empirically describes the behavior of brittle materials; Irwin realized it fell short for ductile materials. Due to the concentrated stresses at the crack tip, ductile materials develop a plastic zone which dissipates energy and contributes to the energy balance in addition to the surface energy gained, requiring an increased energy release rate for growth of a crack. An alternative approach to the energy description was introduced whereby the intensity of the crack tip denoted K in front of the crack tip is considered as the criteria for crack extension. Irwin described the stress field at some distance r and angle θ in front of the crack tip as $\sigma_{ij} \rightarrow K/\sqrt{2\pi r}\, f_{ij}(\theta)$ as $r \rightarrow 0$ [3]. K defines the magnitude of the local stress. Alternatively we can consider this stress intensity in terms of the remotely applied stress σ_{app}, such that $K = Q\sigma_{app}\sqrt{a}$. Here a is the length of the crack and Q is

a term that accounts for the geometry of the material being loaded (i.e., Q = 1 for an infinite plate loaded in tension) [4]. In this context, crack growth occurs if the applied stress results in some stress intensity $K = K_C$. In linear elastic materials, and for tensile opening conditions (denoted mode I), the strain energy release rate and the stress intensity factor are simply related by $G = K^2/E$, where E is the elastic modulus of the material. In simple terms, toughening a material thus requires some mechanism to cause an increase in applied driving for per unit crack extension.

Damage Tolerance in Composites

Well characterized engineering toughening strategies include fiber-reinforcements[5] in ceramic and polymer matrix materials and ductile particle inclusions[6] in ceramics. Mechanistically fiber reinforcements tend to bridge the surfaces of opening cracks. Through debonding and frictional sliding against the matrix, this bridging can dissipate additional energy, increasing the strain energy release rate for crack growth. This can also be considered as shielding the crack tip from applied stresses, thus lowering the K. The result of toughening in composites is quite evident; Figure 1.1 shows a materials space of toughness and strength normalized by density. We see that engineering composites (shown in red) performed better than the constituent materials described above (polymers, metals, and cermamics). What is also evident is that natural materials exhibit a wide range of specific toughness at relatively high specific strength, seemingly unattainable by engineering materials. This raises the question: what can we learn from nature in terms of designing damage tolerance?

1.2 Strong and Tough Biomaterials

Natural heterogeneous materials like bone and nacre are widely coveted as structural design examples, as they exhibit an unparalleled combination of strength, toughness, and density. This is generally attributed to an extremely hierarchical structure of most of these materials [8]. What is unique about many of these materials is that the structure-property relation in natural materials goes all the way down to the nanoscale, a length scale that has been challenging to isolate, probe, and understand. For example, bone is composed of soft and compliant collagen fibrils mineralized by a hard and stiff bioapatite at the nanoscale that form the heterogeneous building block (~100 nm diameter) for the different morphologies of bone across the various length scales; nacre is a simpler "brick-and mortar" structure of aragonite platelets held together by chitin biopolymer [9]. It has been hypothesized that the nanoscale constituents of these natural materials are instrumental for their macroscale proper-

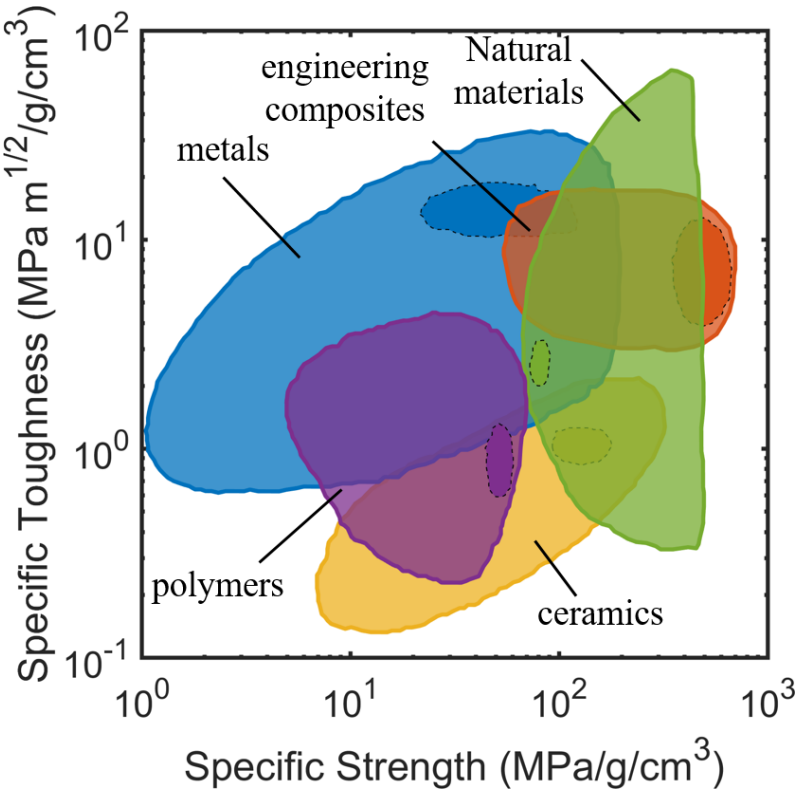

Figure 1.1: Materials Properties Space of Toughness vs Strength. *Adapted from [7]*

ties; for example, the nanoscale characteristic dimensions of the minerals in these materials could lead to flaw tolerance [10]. Mimicking hierarchical materials to achieve similar damage tolerance has gained substantial traction over the past two decades; the main challenge has been introducing hierarchy starting from nanoscale features to produce bulk materials [11]. Some of the most notable methods involve kinetically controlled freeze casting[12] and magnetically assisted slip casting [13] of alumina to create nacre-like materials. While these biomimetic studies have focused on overcoming hierarchical manufacturing challenges, the fundamental question of the structural biomaterials and biomimetic communities remains experimentally unanswered (particularly for bone): how do the underlying nano and microscale components of these hierarchical natural materials give rise the desirable property combination?

1.3 Thesis Overview

The aim of this thesis is to gain a deeper understanding of the small-scale mechanics of human bone. Overall we attempt to gain some insight as to how it is designed in the context of an engineering material. Specifically, we aim to understand the

origin of strength and fracture toughness. In the first chapter we have provided an brief overview of the engineering interest in biological materials. In the second chapter we investigate the structure of bone a provide a revised hierarchy of human bone based on new findings. This revised hierarchy serves as a framework for the mechanical experiments in the thesis. In the third chapter we investigate the site specific deformation and strength of bone at length scales $\sim 10\mu m$ and smaller. In the fourth chapter we develop an approach for performing fracture on microscopic specimens and investigate the fracture behavior of bone in its macroscopically naturally crack arresting or "toughest" orientation. In the fifth chapter we provide a brief summary of the work presented in this thesis. We also discuss the employing the new way of thinking about fracture of materials at small length scales as well as the phenomenological scaling behavior of toughening mechanisms for designing toughness in synthetic materials.

Chapter 2

A REVISED HIERARCHY OF TRABECULAR BONE: NANOSCALE DISORDER

Chapter Abstract

The hierarchical organization of components within bone has been credited with its remarkable combination of strength and toughness that outperforms those of its two main nanoscale constituents, hydroxyapatite and collagen. The process by which these two constituents form what we know at the macroscale as bone is still unknown. The simple description of the emergent theory is that the polymeric collagen forms a scaffold for mineralization by the hydroxyapatite. Investigations into the mineral phase in other biogenic materials like nacre have revealed an amorphous microstructure in the mineralization stage. It has been proposed that in human bone, an amorphous mineral serves as a precursor to the formation of crystalline hydroxyapatite, i.e., bone growth, yet the mechanism for amorphous-to-crystalline transformation mechanism remains unknown. Here we use Transmission Electron Microscopy (TEM) to provide direct evidence of 100-300 nm-sized amorphous calcium phosphate (ACP) regions. These regions are present in a disordered nanocomposite phase within the bone located in the nodes of the trabecular network. When the disordered phase is deprotienated, we observe crystallization within the ACP. Based on these we present a revised hierarchical structure of trabecular bone.

Adapted from:

Tertuliano, O. A. & Greer, J. R. The nanocomposite nature of bone drives its strength and damage resistance. *Nature Materials* **15**, 1195–1202 (2016). URL http://www.nature.com/doifinder/10.1038/nmat4719.

O.A.T performed the experiments, analyzed the data, and developed model and wrote the manuscript.

2.1 Current understanding of bone mineralization in bone

Hard biological solids, such as nacre, dentin, and bone, possess an extraordinary combination of toughness and strength that has been not fully replicated by existing biomimetic efforts [11, 14, 15] . Multiple studies suggest that this property amplification arises from the hierarchical sub-structure —- all the way to the nanometer level — within the hard biocomposites [10, 16, 17]. At the nanoscale, bone is composed of collagen triple helices mineralized by hydroxyapatite (HA) nanocrystals [18, 19]. This nanocomposite forms the functional units, ~ 100 nm-diameter mineralized collagen fibrils, which assemble into the lamellar structure of bone [20], as shown in Figure 2.1c. The lamellae are arranged in various ways to compose the two distinct types of bone, cortical and trabecular. Cortical bone, the most abundant at 80% of the total bone mass, composes the shaft of all long bones, such as femur (Fig 2.1a), and of shell material in flat bones, such as cranial plates11. The remaining 20% is trabecular bone, which is the highly porous (40-90%) network of beams and plates confined to the ends of the long bones (Fig 2.1a,b) and between the flatter bones [14, 21].

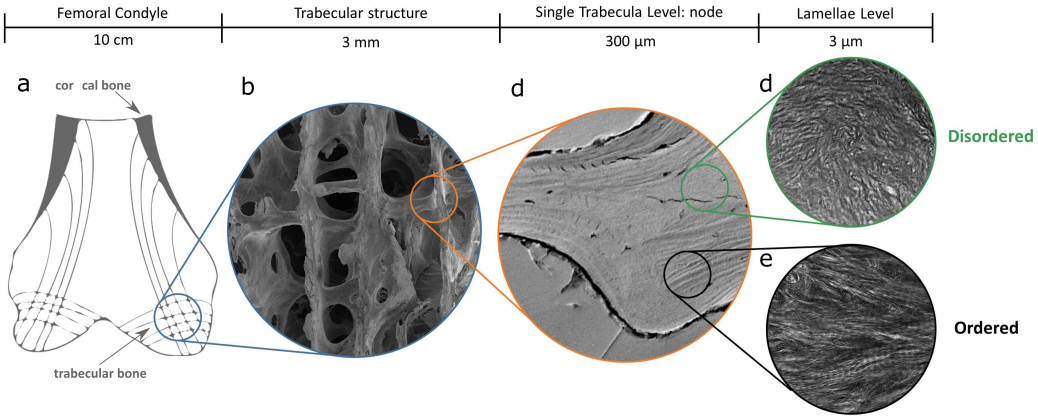

Figure 2.1: Revised hierarchy of trabecular bone. a) A cross-sectional schematic of the lower femoral condyle shows the trabecular structure is confined in spaces not occupied by cortical bone. b) At the millimeter scale it is composed of beams and plates while at the microstructural level (c) there is a combination of an ordered lamellar structure (e) in the beams and a disordered structure (d) at the center of the nodes, where the beams intersect.

The biomineralization literature to date reveals that crystalline hydroxyapatite (cHA) is present at the nanometer length scale within the bone hierarchy, yet the mechanism for bone mineralization has not been fully understood or postulated [22].

The presence and function of an amorphous mineral phase at the nanoscale in bone has garnered much attention in biomineralization research. Amorphous calcium phosphate (ACP) has been observed in zebrafish bone via transmission electron microscopy (TEM) and was proposed to serve as a transient precursor to the formation of nanocrystalline cHA [23, 24]. Solid state nuclear magnetic resonance (ssNMR) studies provide evidence for a more permanent form of ACP functioning as a distinct surface domain around a carbonated hydroxyapatite core in bone mineral [25, 26]. These biomineralization studies were conducted by dispersing either bone mineral or biomimetic apatites in ethanol, which renders determining the relationship between the amorphous mineral phase and the collagen within the bone nanocomposite ambiguous.

In this chapter, we report site-specific TEM analysis of the human trabeculae and identify an ordered bone phase in the lamellae and a disordered phase in the nodes of the trabeculae, which contains an amorphous mineral. We provide electron diffraction evidence for the direct transformation of biogenic ACP to crystalline HA with time. Finally we discuss the importance of theses findings in the context of the structure of bone.

2.2 Preparation of human bone for site-specific TEM

We acquired fresh human trabecular bone from the femoral medial condyle of a 50 year old female donor with no history of bone disease (Articular Engineering). Pieces of the trabecular structure are cut to ~ 3x3x3 mm3 samples. The samples are cleaned with detergent in an agitator for 24 hours at 37^{o} C to remove bone marrow and the fatty tissue infiltrating the porous trabecular structure. To expose the interior of the nodes and beams the bone is embedded in polymethylmethacrylate (PMMA) and polished in 5 steps: diamond lapping paste (9, 6, 3 and 1 μm) and finished with a 0.05 μm diamond lapping paper. We next evaporate 40 nm of gold on the polished surface to reduce charging effects in scanning electron microscopy (SEM) and Focused Ion Beam (FIB) milling.

A TEM lift-out technique is employed to prepare sections for TEM analysis. Using FIB milling (FEI Versa 3D DualBeam), initial 2 μm thick sections are carved from the nodes and the trabeculae lamellae, with sections being parallel to the lamellae orientation. The sections are excised and attached to nanomanipulator using gas injected Pt deposition. The sections are then attached to a copper grid with Pt deposition and freed from the manipulator using FIB milling. Once on the grid,

the sections are FIB-milled to a thickness of 100 nm in 4 steps using the following voltage and current conditions respectively: 30 kV 1 nA; 20 kV 300 pA; 15 kV 10 pA; 15kV 1.5 pA. TEM is performed on these sections at 300Kv.

2.3 Microstructure of the Ordered and the Disordered Phases

TEM microstructural analysis of the bone reveals two distinct microstructures at the nanoscale, ordered and disordered. Figure 2.2a shows a lamellar structure with a preferred orientation of collagen fibrils along the lamellar axis. The periodic banding structure of collagen with a 67nm pitch is indicated by alternating dark and light contrast in the image. This banding pattern originates from the overlapping of collagen molecules during fibrillogenisis (the formation of collagen fibrils); the banding is thus orthogonal to the fibril alignment. The inset electron diffraction pattern shows the (002) and mixed (112), (211), and (300) diffractions of cHA crystals. We refer to this general microstructure as the *ordered phase*. Figure 2.2b shows TEM micrographs of sections extracted from the nodes of the trabeculae, exposing a densely entangled arrangement of collagen fibrils. No preferential orientation or detectable arrangement of the fibrils was observed. The diffraction pattern in the inset shows weak (002) reflections and a diffuse ring with a calculated spacing, d, of 2.85 Å, indicative of amorphous calcium phosphate (ACP) [27]. We will refer to this microstructure as the *disordered phase*.

2.4 Mineral structure of the ordered and disordered phase

To further probe the microstructure of the mineral within the respective ordered and the disordered phases of the bone, we deproteinate the trabecular samples in NaOCl.To deproteinate samples we employed a protocol similar to that described in [28] . The samples are submerged in a 5% NaOCl solution for 72 hours with the solution changed at 24 hr intervals and subsequently rinsed in Hanks Buffered Saline Solution (HBSS). This solution is similar in ionicity and pH to extracellular matrix that surrounds bone *in vivo*. Depreotination of the structure was verified via Raman spectroscopy before and after the NaOCl treatment as show in 2.3. Pre-treatment Raman analysis shows characteristic PO_4^{-3} peaks at 438, 589, and 959 cm^{-1} and a peak at 1075 cm^{-1} indicating CO_3^{-2} substitutions. It also shows amide III, C-H, and amide I peaks as well as proline and hydroxyproline. After the NaOCl treatment, these polymer peaks are no longer visible.

Figure 2.4 shows a TEM micrograph of the deproteinated mineral phase within a thin section extracted from an ordered lamella. In the absence of collagen, the ordered

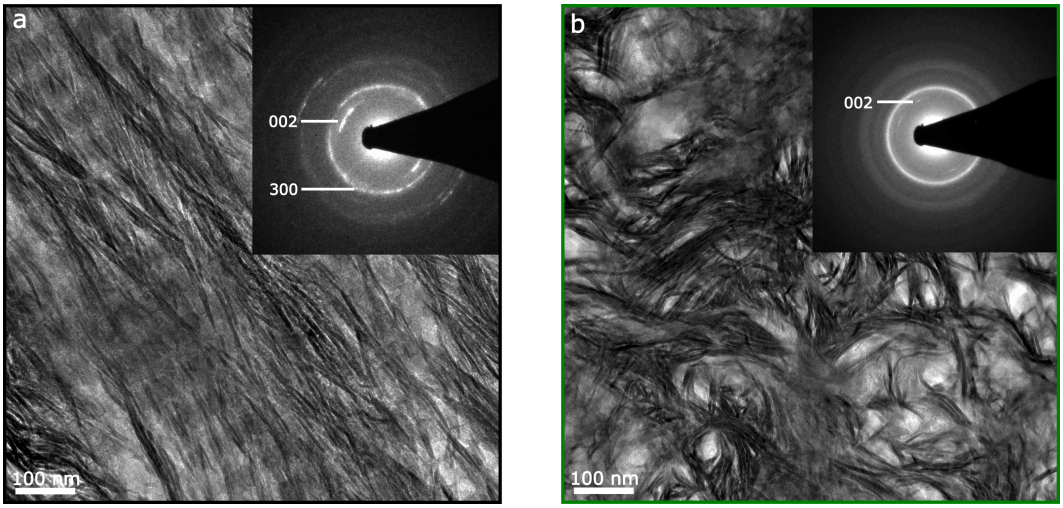

Figure 2.2: a) Ordered or lamella phase showing arrangement of collagen fibrils and corresponding electron diffraction pattern illustrating (002) and mixed (112), (211), and (300) reflections of cHA nanocrystals . b) Disordered composite phase showing entangled collagen fibrils with lack of preferential orientation or characteristic banding pattern. The diffuse ring in the diffraction pattern inset indicates an amorphous mineral (ACP) and less intense (002) reflections of cHA.

microstructure appears to be composed of multiple nanocrystallites; the diffraction pattern in the inset shows intense (002) reflections, which correspond to crystalline cHA, identical to those in the untreated sample in 2.2a. The high-resolution TEM image in the inset of Figure 2.4a reveals the periodic fringes of the crystallites, with this particular crystal having a spacing of 2.78 Å, corresponding to the (112) planes of the crystalline hydroxyapatite. Figure 2.4b reveals a combination of amorphous calcium phosphate and nanocrystalline mineral within the disordered phase. We identified multiple isolated fully amorphous regions, which span roughly 100 to 300 nm in size. Adjacent to these amorphous regions are nanocrystals, which appear to be embedded in an amourphous calcium phosphate matrix themselves. The diffraction pattern from this region shows (112), (211), and (300) reflections from the embedded crystal corresponding to the cHA, and the HRTEM inset confirms the atomic scale disorder in the isolated amorphous regions.

To probe the stability of the observed amorphous calcium phosphate in disordered phase with respect to the adjacent hydroxyapatite nanocrystals, we performed TEM analysis of the same region after a 30-day time lapse. During the 30 days, the TEM sample was stored at room temperature in a N_2 environment. Figure 2.5a shows the initial arrangement of ACP (left) and HA nanocrystals (right), as well as the

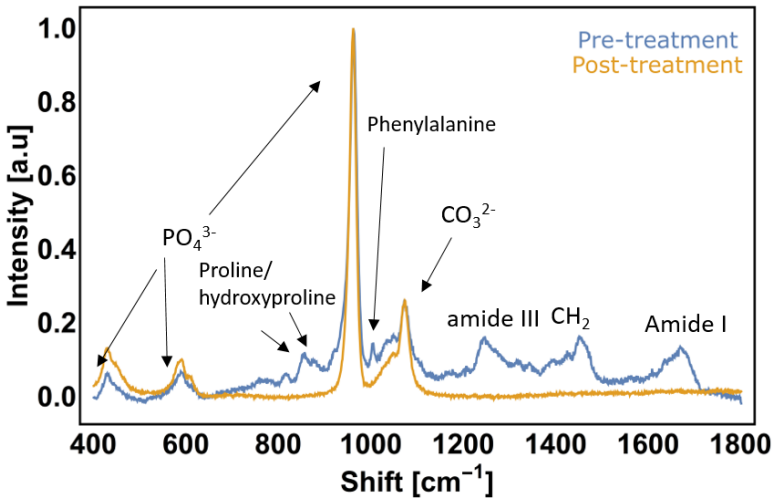

Figure 2.3: Raman spectra before and after NaOCl deprotination of bone showing disappearance of all protein peaks after the treatment.

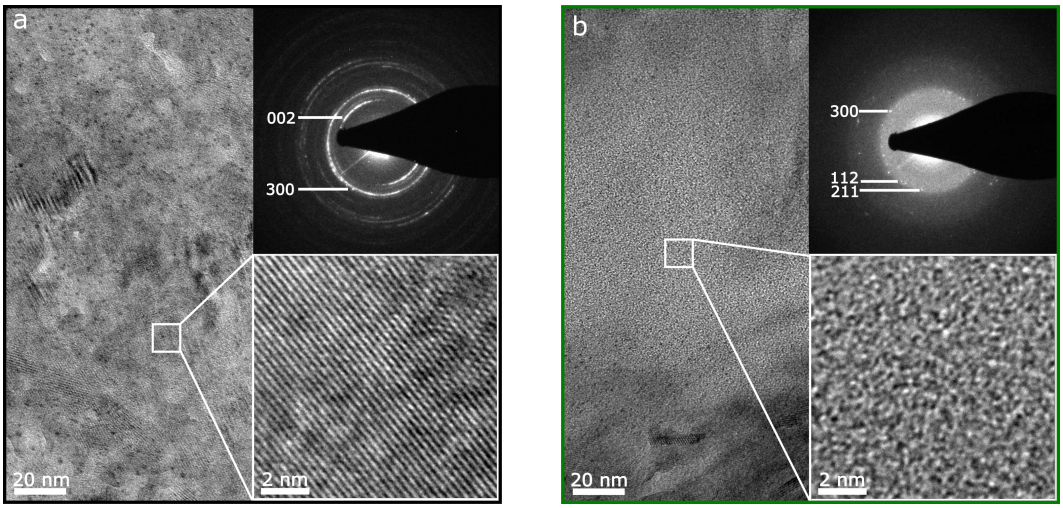

Figure 2.4: Mineral structure of bone. a) Deproteinated mineral of ordered bone showing a nanocrystalline microstructure as evidenced by the diffraction pattern and atomic scale order in the HRTEM inset. b) Deproteinated mineral of disordered bone showing ACP structure along with cHA nanocrystals in an ACP structure. (bottom left). The HRTEM inset shows the corresponding ACP atomic scale disorder and the diffraction pattern shows the (112) (211) and (300).

diffraction pattern inset showing the crystallinity of the HA. Figure 2.5a shows the same region after the 30 day incubation period; the HA nanocrystals on the right appear to have grown, confirmed by the increased (112), (211), (300) intensities in the diffraction pattern inset; we also observe the emergence of (002) reflections after

one month, which further proves the formation of crystals. The significance of the TEM results are now discussed in the following sections.

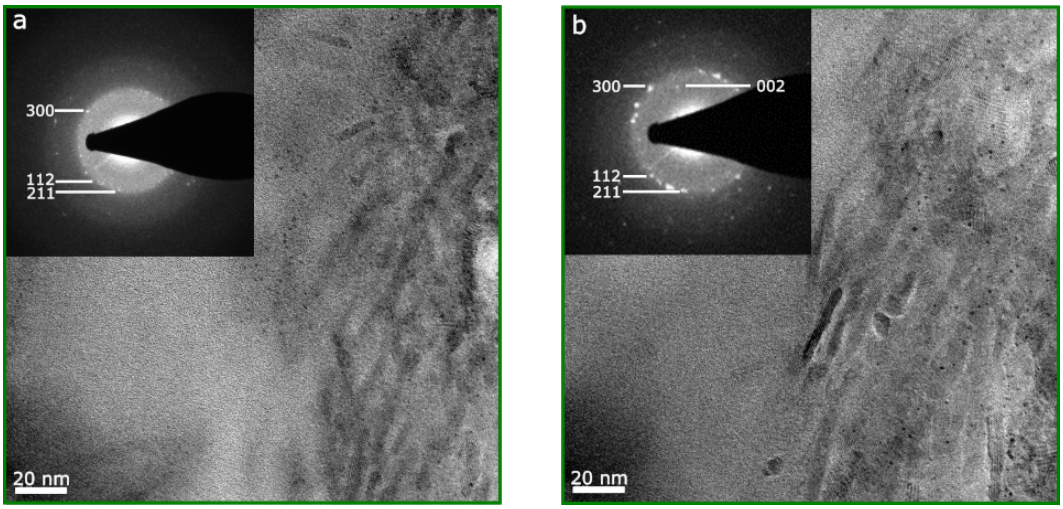

Figure 2.5: Crystallization of amorphous mineral. Deprotonated mineral structure in disordered phase taken before (a) and after (b) a 30 day incubation at room temperature in a nitrogen environment. The electron diffraction pattern after the incubation (b, inset) shows an increase in crystallinity as evidenced by more intense HA reflections and the emergence of the (002) spots when compared to the initial diffraction pattern (a, inset).

2.5 Presence of ordered and disordered microstructure

We observed two distinct phases in trabecular bone, each containing a mineral and collagen nanocomposite: (1) an ordered microstructure, which composes the lamellae, and (2) a disordered phase at the center of the nodes. The TEM image of the ordered phase (Fig. 2.2) shows periodically-arranged mineralized collagen fibril arrays, consistent with previous structural investigations of the lamellar structure of bone[20, 29, 30]. The disordered phase is characterized by entangled collagen fibrils with no preferential arrangement or orientation. Recent studies of the demineralized collagen network in human cortical and trabecular bone reported the presence of a similar disordered collagen structure at the interface in ordered phase lamellae [31, 32]. We demonstrate that this disordered phase is also present in the center of the nodes of the trabecular network. The specific role of this disordered phase in biomineralization and structural responsibilities has not yet been unambiguously established. It was proposed that the disordered phase carries the canaliculi network [32], which allows communication among osteocytes embedded in the bone material via percolation through the bone structure. Our observations of the disordered

nanocomposite phase, in conjunction with the previous observations, suggest the disorder likely permeates throughout the hierarchal structure of the bone: it forms the intra-lamellar interfaces in cortical and trabecular bone and the nodal cores in the trabecular network. Its ubiquitous presence suggests that the disordered cHA-ACP nanocomposite plays a critical role in biomineralization and growth of bone, and likely in its mechanical resilience. This latter will be thoroughly investigated in Chapter 3.

2.6 Structure of the mineral in the bone hierarchy

The effect of the collagen scaffold on the mineralization of bone is still under debate because it has been challenging to replicate relevant *in vivo* conditions. However this has become clearer with use of organized, high collagen fibril density biomineralization models [33–35]. Wang et al. suggest that a 3-dimensional periodic structure of collagen fibrils, with its characteristic gaps and overlaps providing space to accommodate new material, is instrumental for the mineralization of fibrils by cHA *in vitro*. Our TEM results show that in the ordered phase, the collagen scaffold is periodically arranged and contains visible gap and overlap regions, predominantly mineralized by nanocrystalline hydroxyapatite. In contrast, in the disordered phase we observe a densely entangled collagen scaffold that contains both amorphous calcium phosphate as well as hydroxyapatite. The lack of a banding pattern contrast in the disordered phase, shown in Figure 2.2b, suggests that the mineral is located uniformly within the collagen scaffold, even when the fibrils are not periodically arranged. This contrast also suggests the mineral is not mainly concentrated in the gap regions as in the ordered lamellar bone. A similar disappearance of the banding pattern observed in the *in vitro* biomineralization models has been attributed to a higher degree of mineralization of fibrils [36, 37]. This would substantially reduce the diffraction contrast between the gap and overlap regions in the fibril structure. Our TEM observations of the contrasting biogenic minerals in ordered and disordered collagen scaffolds support the conjecture that an ordered fibril structure array may govern the mineralization process.

2.7 Summary and Outlook

The TEM analysis presented in this chapter revealed the presence of a disordered phase in distinct locations in the trabecular network. We also found that the microstructure within the mineral in the disordered phase contains a mix of amorphous calcium phosphate regions and nanocrystalline hydroxyapatite. This enables an ad-

dendum to our understanding of the microstructure of bone. In Figure 2.1, which illustrates a femoral condyle at the macroscale, we show a porous trabecular network at the mesoscale, a lamellae and nodal structure at the micron scale, an ordered collagen/cHA in the lamellae, and now also disordered collagen/ACP/cHA in the nodes at the nanoscale. These findings enhance the existing understanding of trabecular bone hierarchy reported by [32]. This description of the hierarchical structure of bone serves as the basis for the mechanical investigations in the following chapters.

The contribution of the 3-dimensional fibril organization to the process of mineralization in bone appears to be of interest to the biomineralization community [28, 35, 36, 38]. One current hypothesis of the collagen mineralization mechanism is that the ordered fibrils give rise to the nanocrystalline mineral structure currently observed in bone [35]. The TEM analysis presented in this work enhances the current state of the art by implying that disordered fibrils may give rise to a mix of amorphous and crystalline mineral (i.e., disordered fibrils may play a role in stabilizing ACP). This is a meaningful observation in real bone that also poses the question of how disordered bone forms i.e/, what is the role of cells in fibrillogenesis of disordered fibrils.

Chapter 3

MICRO- AND NANOSCALE DEFORMATION AND STRENGTH OF BONE

Chapter Abstract

The stiffness and strength of bone tissue are generally described to stem from the properties of its main constituents, the inherently nanoscale collagen and hydroxyapatite. Yet little has been done to understand the isolated deformation behavior of bone at these relevant length scales. In this chapter, nanomechanical experiments on cylindrical samples (3000 to 250 nm in diameter) of the bone's ordered and disordered phases revealed a transition from plastic deformation to brittle failure and at least a factor-of-2 higher strength in the smaller samples. We postulate that this transition in failure mechanism is caused by the suppression of extrafibrillar shearing in the smaller samples, and that the emergent smaller-is-stronger size-effect is related to the sample-size scaling of the distribution of flaws. Our findings should elucidate the multiscale nature of bone strength.

Adapted from:

Tertuliano, O. A. & Greer, J. R. The nanocomposite nature of bone drives its strength and damage resistance. *Nature Materials* **15**, 1195–1202 (2016). URL http://www.nature.com/doifinder/10.1038/nmat4719.

O.A.T performed the experiments, analyzed the data, and developed model and wrote the manuscript.

3.1 Intro

The introductory chapter described that strength and toughness of materials are classically deemed as inversely related, but hard biogenic materials like bone and nacre are reported to mitigate this conflict at the macroscopic tissue level [1]. It is suggested that this damage tolerance — the combination of high strength and toughness - in natural materials arises from their complex hierarchical sub-structure — all the way to the nanometer level [10, 16, 17]. This is in part because the damage tolerance of bone outperforms that of collagen and hydroxyapatite: its fracture toughness is at least an order of magnitude higher than that of either constituent, and its reported macroscopic failure strength varies with mineral volume fraction in a manner that is not yet described by simple composite models [39]. These points suggest that understanding the collagen and mineral interplay in bone is integral to understanding its mechanical response. To date, most research efforts on the mechanical properties of bone have primarily focused on its macroscale response and have been unable to decouple the hierarchical structural response from a material level deformation. Thus a mechanistic understanding of how bone deforms and fails at the length scale of its fundamental constituents remains elusive.

While toughness of bone has been generally reported to arise from the complex multi-scale hierarchy (subject of Chapter 4), its relatively high strength and stiffness are linked to the nanoscale spacial arrangement of collagen and hydroxyapatite [40, 41]. In trying to explain these enhanced mechanical attributes, the existing nanoscale composite deformation models are based on the assumption of an ordered model of HA crystals and collagen [41]. A popular model for describing the composite nature of collagen and HA involves considering minerals embedded in a collagen matrix as follows: minerals are arranged in a staggered motif within the collagen matrix; the minerals are rigid and rigidly bonded to the collagen matrix; tensile stress of the tissue accommodated by shearing of the collagen matrix that is located between the embedded mineral. this shearing transmits stress to rigid mineral. This model suggests a continuum model of bone in which the elemental unit is not a mineralized collagen fibril but instead a composite of collagen and HA; is consequentially is unable to account for extrafibrillar mineralization as well as a disordered nanocomposite previously described in this thesis. In Chapter 2 we used our TEM findings of disorder at the nanoscale to expand on the previously understood hierarchical structure of bone. The recently discovered presence of amorphous calcium phosphate in the sub-lamellae length scales calls for a re-evaluation of these models, especially in understanding the contribution of amorphous calcium

phosphate (ACP) and other microstructural components to the mechanical response of the bone, i.e., its strength and failure mechanism, at each characteristic length scale.

In this chapter, we report the size-dependent deformation behavior of bone under compression. We fabricated cylindrical micro- and nano-pillars with diameters of 250 to 3000 nm from each phase, ordered and disordered, using Focused Ion Beam (FIB) and performed dry uniaxial compression experiments using the methodology commonly used to probe nanoscale mechanical properties of rigid solids [42, 43]. Our experiments revealed a ductile-to-brittle transition and a higher strength form the micro- to the nanoscale in both phases. We found the elastic modulus of the disordered phase, measured via nanoindentation, to be 1.3 times higher than that of the ordered phase. We developed a stochastic model, which treats the existing flaws in sample morphology, i.e., pores, as stress concentrators in initiating yielding and deformation, which quantitatively captures the emergent size effect. We discuss the increase in the yield stress at smaller sample dimensions, observed in both ordered and disordered phases, in the framework of this model.

Performing nanomechanical experiments on bone

FIB milling is employed to fabricate cylindrical micro- and nano-pillars for uniaxial compression experiments. In the nodes and beams of the untreated trabecular architecture, concentric annuli of decreasing diameter are milled using decreasing beam currents. Using an accelerating voltage of 30kV, the annuli were milled at 5000, 1000, 100, and 10 pA. A 1pA final cleaning cut was used for the 500 and 250 nm pillars. We fabricate pillars with nominal diameters of 3000, 2000, 1000, 500, and 250 nm (N=5 for each) with length to diameter aspect ratios of 3 to 1 to eliminate buckling and edge effects in the compression data. This process is shown on a 250 nm pillar in Figure 3.1 and Supplemntal Video 1. Samples fabricated from the ordered phase were made so the pillar axis is orthogonal to the lamellae; the fibril orientation in the nano-pillars made from the disordered phase was inherently random.

Compression experiments were performed on dry pillars with a 10 μm diamond flat punch tip in an Agilent G200 Nanoindenter. A quasi static strain rate of 10^{-3} s^{-1} is used on all pillars to eliminate strain rate dependence that could arise from viscoelastic properties of collagen. The uniaxial compression experiments allow us to measure load (p) and displacement (d) and convert those to stress (σ) and strain

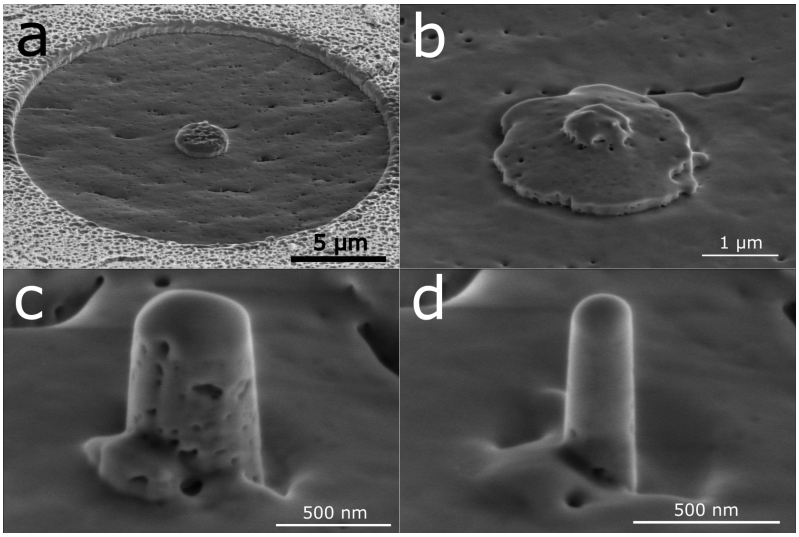

Figure 3.1: Fabrication of bone nanopillar via FIB milling- a-d show the evolution of the pillar as we make smaller concentric cuts using the FIB at decreasing currents. The final cleaning cut is done at 10 pA.

(ϵ) using the simple engineering relations $\sigma = p/area$ and $\epsilon = (h_0 - d)/h_o$. Here the area refers to the cross sectional area of the pillar and and h_o is the original height of the pillar. Yield strength is measured via the 0.2% offset method. The elastic portion is taken as the strain prior to this yield while plastic strain is strain after this yield.

We used nanoindentation to measure the elastic modulus of each phase. A diamond Berkovich tip is used to perform indentation experiments on polished surface. This technique also allows measurement of load vs displacement; however, the stress state is no longer generally uniaxial as in the compression experiments. Hertzian contact mechanics solutions for axis-symmetric indenters into elastic half-spaces serve as the bases for extracting the elastic response from the load vs displacement data [44]. We use the well established Oliver and Pharr methodology for an elastic solid [45]. In this context the elastic modulus is defined in 3.1. Here E and E_i are the elastic moduli of the material and indenter, respectively, while E_r is the reduced or effective modulus of the contact in the experiment. Additionally S is the unloading stiffness from the load vs displacement response, A is the area of the contact, and β is a correction factor for indenter tips that are not perfectly axis symmetric; this is generally around unity (~ 1.07 for a Berkovich).

$$E_r = S\left(\frac{\pi}{A}\right)^{\frac{1}{2}}\frac{1}{2\beta} = \left(\frac{1-\nu^2}{E}+\frac{1-\nu_i^2}{E_i}\right)^{-1} \tag{3.1}$$

3.2 Nanomechanical Response of Ordered and Disordered phases

Figure 3.2 shows representative pre- and post-compression images and stress vs. strain data for 3000, 500, and 250 nm-diameter pillars. In the ordered phase, the two largest pillars, with diameters of 3000 and 500 nm, failed via shear offsets with an average shear angle of 46.6 ± 7.8° with respect to the loading orientation (Fig.3.2a,b), and the 250 nm-diameter sample catastrophically collapsed (Fig.3.2c). As show in Figure 3.3, the stress vs. strain data of the 3000 nm samples is characterized by an initial linear elastic response followed by yielding and plastic flow region where most of the shear-off processes occurred. The 500 nm-diameter samples exhibit similar features, with more abrupt shearing events. The data for the smallest, 250 nm-diameter pillars displays linear elastic behavior to failure via brittle fracture. We determined averages and standard deviations of the characteristic yielding strengths of these samples to be 327 ± 20 MPa for 3000 nm samples at 5.1 ± 0.9% strain, 247 ± 32 MPa for 500 nm samples at 3.4 ± 0.8% strain, and 591 ± 91 MPa for 250 nm samples at 6.7 ± 0.5% strain.

In the disordered bone, we measured the characteristic strengths of 313 ± 8 MPa at 4.1 ± 0.3% strain, 320 ± 20 MPa at 4.7 ± 1.4 % strain, and 658 ± 160 MPa at 4 ± 1.9 % strain, for the same respective diameters. Post-compression images of the 3000 nm samples, shown in Figure 3.2d, reveal that failure occurred via a shear offset at 44.0 ± 1.2°. The two smallest-sized samples, with diameters of 500 nm and 250 nm, displayed failure that likely initiated at the pores (Fig. 3.2f,e). Characteristic strength vs. pillar diameter for ordered and disordered pillars is plotted in Figure 3.4. We observed higher characteristic yield strengths with decreasing pillar diameter and compared with bulk (3000nm) in both microstructures; the disordered bone strength increases by a factor of 2 and the ordered one by a factor of 2.4 from the 500 to 250 nm diameter samples. The elastic loading slope in the compression experiments may be misleading because it is sensitive to the typical experimental artifacts associated with this methodology, like slight misalignment between the nanoindenter tip and the pillar and/or the compliance of the substrate [42]. To reduce susceptibility to these issues, we used nanoindentation to measure the elastic

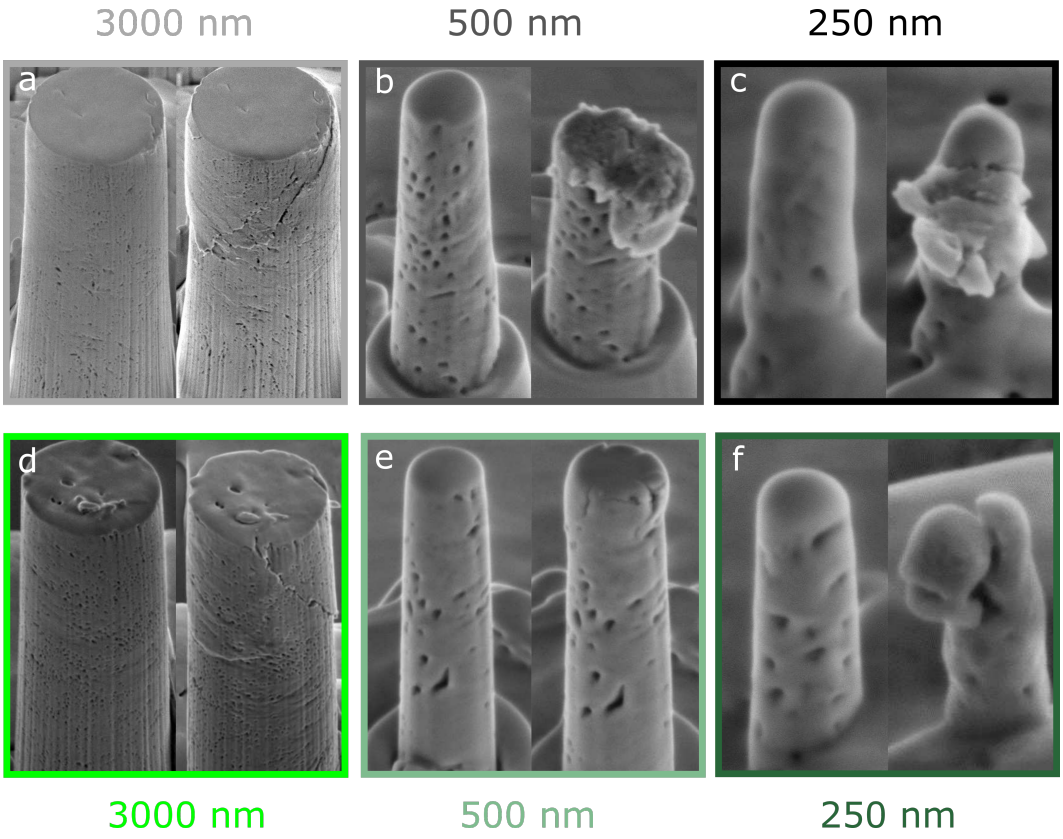

Figure 3.2: Deformation of Ordered and Disordered pillars. a-e) Pre- and post-compression (left and right, respectively) of ordered (a,b,c) and disordered (d,e,f) pillars showing samples exhibiting distinct failure modes: shearing in a,b,d) and brittle failure in c,e, and f)

modulus of each phase, which was 16.3 ± 1.5 GPa for the ordered phase and 21 ±1.8 GPa for the disordered one. We now discuss the relevance of these mechanical results in the following sections.

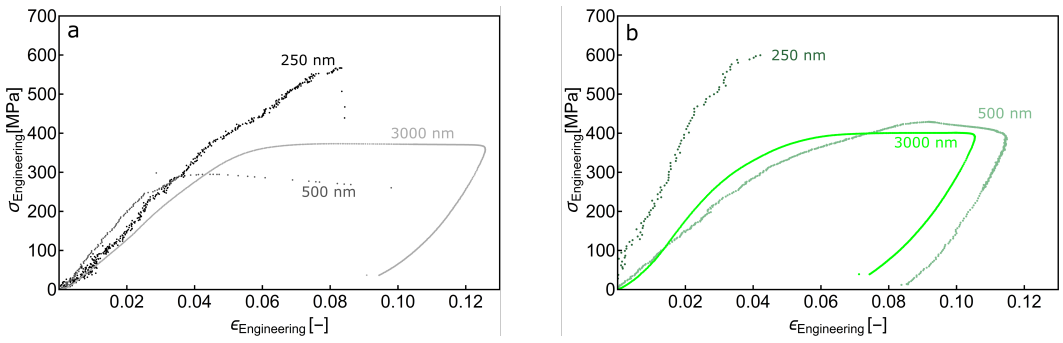

Figure 3.3: Characteristic stress vs. strain responses of the ordered a) and disordered b) 3000, 500 and 250 nm pillars

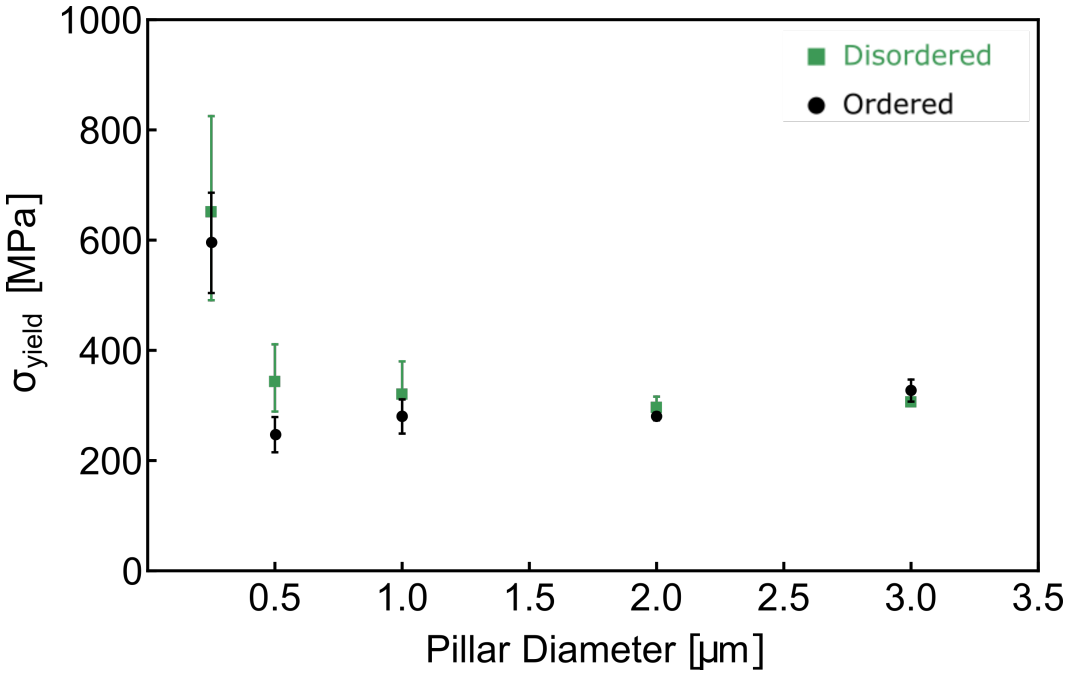

Figure 3.4: Yield strengths across pillar diameters. Both the ordered and disordered samples exhibit size independent yield strengths up until the nanometer regime in which there is a dramatic increase in strength.

3.3 Deformation and stiffness in ordered and disordered phases

SEM images of the compressed samples, shown in Figure 3.2 (a,b, and d), suggest that failure occurred via a series of shear events in the samples with diameters of 3000 nm down to 1000 nm in the disordered phase and over the same range of sizes down to 500 nm in the ordered phase. The corresponding stress vs. strain data shows that both phases displayed linear elastic loading followed by ductile deformation, with plastic (inelastic in the case of bone) strains up to 5.1 % in the ordered bone and 6.3 % in the disordered bone. All 250 nm-diameter nano-pillars displayed a linear elastic response up to brittle failure regardless of microstructure. The deformation mechanisms of bone vary throughout its hierarchy; to date, isolating those active at the smallest relevant scales has proven challenging. Gupta et al. conducted small-angle x-ray scattering (SAXS) and wide-angle x-ray diffraction (WAXD) measurements of the local strain within bone tissue during *in situ* tensile experiments and found that the strain within the collagen fibrils remained constant after the yield point of the bone tissue. These authors proposed inter-fibrillar sliding through shearing of the extra-fibrillar matrix as the mechanism of inelasticity in nanoscale bone [46–48]. Recently compression experiments of 500 nm-diameter bone micro-pillars were able to isolate lamella scale deformation, showing shearing

occurs at this level [49]. The dominant deformation mechanism of shearing in the 3000 - 500 nm diameter micro-pillars found in the present study is consistent with this literature. Adding to the existing state of knowledge, we postulate that the ductile to brittle transition from micro- to nano-pillars can be interpreted as an extension of the previously reported deformation mechanisms to the nano-scale regime, where dimensional reduction suppresses inter-fibrillar sliding.

The change in the mechanical response in ordered bone when sample size is reduced from the micro- to nano-scale hints at a transition in the deformation mechanism from inter-fibrillar sliding in 3000 - 500 nm diameter pillars, which accommodates shear strains, to brittle failure of mineralized fibril in the 250 nm-diameter ones. We propose this mechanism to be as follows: as the pillar size decreases from 3000 to 250 nm, the average number of mineralized collagen fibrils spanning the diameter decreases from 30 to 2.5, assuming a collagen fibril diameter of 100 nm. This reduces the number of possible inter-fribrillar sliding events by an order of magnitude and substantially reduces the amount of inelastic strain it is able to accommodate. As a result, the mineralized collagen fibrils in the 250 nm-diameter pillars are elastically strained to failure. This deformation mechanism explains the change in failure mode from shearing to brittle fracture in the ordered bone. Our results demonstrate that the deformation of bone depends on the sample size down to the fibril level at the nanoscale in dry, ordered bone.

The deformation of isolated disordered phase of the bone has not been reported. The results of this work demonstrate similarities in the mechanical response of the 3000 mm-diameter samples extracted from the ordered and the disordered phases of the bone (Fig. 3.3a,b), which suggests the shearing of the extra-fibrillar matrix to be the dominant microscale inelastic mechanism in both phases. The extra-fibrillar matrix is composed of non-collagenous proteins and extra-fibrillar mineral and is reported to serve as a "glue" between the mineralized fibrils [19]; this would lead to a similar contribution in the microscale deformation in the ordered and disordered phases, consistent with the results observed here.

The nanoscale mechanical response between the two phases is similar in post-elastic deformation but varies in the elastic regime. We observed a higher linear elastic loading slope of 18 ± 2.4 GPa in the 250 nm-diameter disordered samples, compared with 8.9 ±1.3 GPa for the 3000 nm-diameter pillars. This difference is significant and likely not related to the experimental artifacts because the loading slopes of the samples fabricated from the ordered phase were 8.9 ±1.1 GPa, sampled over 6

pillars of all sizes, similar to those of the larger disordered bone pillars. We attribute this difference in the elastic modulus between the two phases, which emerges at the nanoscale, to the amount of mineralization within the fibrils; by rule of mixtures, the more mineralized the fibril, the stiffer the sample. We can recall results from Chapter 2 to expand on this.

TEM images in Figure 2.2 a,b reveal that the contrast caused by the periodic arrangements of the mineralized collagen fibrils is not present in the disordered phase; In Chapter 2 we proposed that this absence of striations is caused by the higher degree of mineralization of the disordered fibrils, similar to previous observations of highly mineralized ordered fibrils [35, 36]. In the compression experiments, the suppression of the extra-fibrillar deformation in nano-sized samples results in the straining of the fibrils, and the stiffer elastic response. Our nanoindentation measurements performed on the surface of each phase revealed an elastic modulus of 16.3 ± 1.5 GPa for the ordered bone, which is consistent with reported values for dry lamella bone via nanoindentation [49, 50] , and 21.0 ±1.8 GPa for the disordered one, which indicates that the disordered phase is 30% stiffer than the ordered one. The compression experiments indicate the disordered phase is 50% stiffer. The absolute value of the elastic loading slope in any nano- or micro-pillar compression data should be taken judiciously because it is subject to errors caused by minor misalignments between the indenter-pillar interface and imperfect contact. For example all measurements of elastic modulus made via pillar compression were lower than those made via nanoindentation (i.e 8 vs 16 GPa for the disordered phase). The disparity in stiffness between the ordered and disordered phases is apparent based on both types of nanomechanical experiments. Along with the TEM analysis from Chapter 2, these findings suggest that the fibrils in the disordered phase are stiffer than those in the ordered one, likely caused by a higher degree of mineralization.

3.4 The effect of microstructure and size on strength

The stress vs. strain data shown in Figures 3.3 demonstrate that the yield strengths of all micro-pillars with diameters of 500 to 3000 nm are nearly equivalent for both underlying microstructures, ordered and disordered. An increase in yield stress occurs when the pillar diameter is reduced from the micro- to the nano-scale in both phases. The ordered phase shows a 2.4-fold increase in strength for samples with 250 nm diameter compared to those of 500 nm diameter, and the disordered phase shows a 2-fold increase for the same respective size comparison. We determined the average strength of the disordered phase to be 10% higher than of the ordered

one at the nanoscale; their mean values agree within error. Our measurements of strength in the ordered phase are consistent with the micro-pillar compression studies of cortical lamellar bone, which report strengths ranging from 300 to 490 MPa depending on the anatomical orientation of the pillar[49]. Those authors also reported a strength increase from the macro- to micro-scale, but the strength of bone at the lowest level of hierarchy, the nano-scale, and its relation to strength at larger scales has not been reported. The nano-pillar compression experiments in this work uncover the "smaller is stronger" size effect present down to the nano-scale.

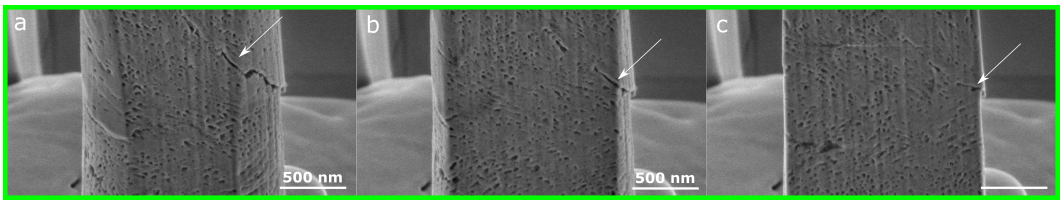

Figure 3.5: Surface flaws as points of initiation of failure

We postulate that this micro- to nano-scale size effect can be connected with the initiation of deformation. The similarity in size effect in both phases points to similar mechanisms for the initial yielding event, which initiates at a flaw or pore. Figures 3.5a-c show SEM images of the cross-sections of a compressed disordered 3000 nm-diameter pillar at lateral depths of 250, 750, and 1500 nm into the pillar to facilitate tracking the failure plane throughout the pillar; this is also available as Supplemental Video 2. We observe that an incipient crack becomes discontinuous, or bridged, when the cross-section sweeps from 250 to the 750 nm into the pillar and is only visible near the surface of the pillar at the 1500 nm section. Based on these post-mortem observations, we hypothesize that failure and deformation during compression initiate at the surface flaws, and the size effect emerges from the lower probability of having these critical flaws in the smaller samples.

3.5 Estimating sources of stress concentration

We propose that the yield strength, σ_{yield}, decreases as the probability of having a flaw (i.e., a pore) on the pillar surface increases; that is, surface flaws serve as probabilistic stress concentrators, which initiate failure during compression. This is manifested most prevalently in the larger pillars, with diameters > 500 nm. At these nano and micro length scales, it is reasonable to consider bone as a fiber-reinforced composite; hence we should also consider microstructural stress concentrations, i.e. ones that arise from stiff fiber reinforcements in a more compliant matrix. To

quantify these effects and to capture their effect on the observed size dependent strength, we calculate the stress concentrations for two different representations of bone: 1) we model the ordered and disordered phases as fiber-reinforced composites to evaluate the stress concentrations that arise from stiff fibers and 2) we consider the small-scale samples as a homogeneous continuum medium with randomly distributed pores to evaluate the stress concentrations caused by surface flaws, i.e., pores. We then compare the stress concentrations from each of these components and employ the strongest stress concentrator to quantitatively describe the emergent size effects in ordered and disordered phases of bone.

Although the main result is the surface flaws serve as the strongest stress concentrator (which is used in the section 3.7), we first discuss the bone in following subsections as a simple unidirectional fiber composite and extra parameters relevant to understand how stress may be concentrated due to elastic heterogeneity at the nanometer substructure.

Stress Concentration from fibers

The stress concentration factor that arises from the stiff fiber reinforcements in a composite, k_f, can be represented as

$$k_f = \frac{1 - \phi_f \left(\frac{E_m}{E_f}\right)}{1 - \left(\frac{\phi_f}{\phi_{fmax}}\right)^{\frac{1}{2}} \left(\frac{E_m}{E_f}\right)} \tag{3.2}$$

where ϕ_f is the volume fraction of the fibers, ϕ_{fmax} is the close-packing fraction of the fibers based on the assumed packing configuration of the fibers (i.e., hexagonal, square, random), and E_m and E_f are the matrix and fiber elastic moduli, respectively[51] . Equation 3.2 is only valid for the cases when the fibers are stiffer than the matrix. To employ this principle, we must first define the functional fibril and matrix in the bone composite. The gap and the overlapping regions within the collagen fibril structure, shown and labeled in Figure 3.6a, have been reported to contain some amount of mineral [36, 41]. This gives rise to a mineralized fibril structure, for which we use the subscript "MF" in our model construction. The mineral that is located externally to the fibril can be tightly bound to the surface of the MF [29] , which gives rise to a coated mineralized fibril, here referred to as "CMF". This external fibril could otherwise be a part of the extrafibrillar matrix, which we refer to as "EFM" . The CMFs have been experimentally observed in bone,

bridging sheared regions in [49] and on failure surfaces [52]. Those experimental observations both suggest that it is important and relevant to calculate the stress concentration due to CMFs, k_{CMF}.

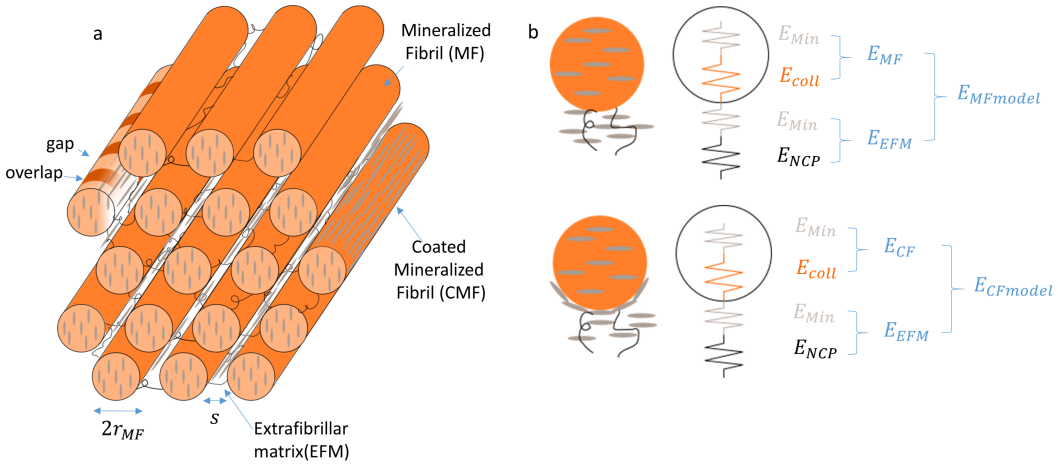

Figure 3.6: Fibrils diagrams. a) Hexagonally arranged ordered fibrils with MF radii r_MF and some spacing s. B) Schematics of the MF and CMF models showing a Reuss, or series, model of the stiffness contributions from the mineral, collagen, and NCPs.

To date, we have not been able to find any literature that reports the elastic properties or volume fractions of CMFs or the complementary EFM; this is likely due to the difficulty of isolating these constituents in experiments and the lack of consensus on the spatial distribution of bone mineral in models and computational efforts. The exact spatial distribution of mineral (intrafibrillar vs extrafibrillar) in bone is still under debate in the literature, ranging from 30% to 75% of the total mineral being extrafibrillar [38, 53]. The amount of extrafibrillar mineral bound to the surface of the fibril has received little attention [54] . Most elastic models of bone at these nano- and micro- length scales do not take into consideration extrafibrillar mineralization [41, 55]. Those that do assume some initial extrafibrillar vs intrafibrillar mineral distribution [54, 56] without a true mechanical basis. Understanding the spatial distributions of bone constituents at these length scales is necessary for calculating k_{CMF}. We calculate k_{CMF} without assuming an initial mineral distribution by modeling bone as a fiber-reinforced composite in two stages: 1) a *MF model* with MFs contained in an EFM, composed of non-collagenous proteins(NCPs), mineral, and pores, and 2) a *CMF model,* in which some mineral from the MF's model EFM is tightly bound to the surface of the CMF, i.e., the initial MF is grown into a

stiffer CMF by effectively absorbing mineral from the EFM. These two models are illustrated in Figure 3.6.

We use the MF model to determine the volume fractions of each fundamental constituent, i.e., collagen, mineral, and non-collagenous proteins (NCPs), as well as the extrafibrilar vs intrafibrillar distribution the mineral. We accomplish this by using the elastic moduli measured in our experiments as constraints for the eigenstress (Ruess) elastic model of the composite. Next, we re-allocate the mineral from the EFM to the MF to "create" a stiff CMF in a more compliant EFM, which allows us to calculate k_{CMF}

MF model

The ordered phase composite is depicted as hexagonally arranged fibrils in the EFM, similar to the arrangement assumed by Nikolov and Raabe (ref [54] and Fig. 3.6a). Then, the elastic modulus of the overall composite in terms of the elastic properties of the MF and the EFM is

$$E_{MFmodel} = \left(\frac{\phi_{MF}}{E_{MF}} + \frac{1 - \phi_{MF}}{E_{EFM}} \right)^{-1} \tag{3.3}$$

where

$$E_{MF} = \left(\frac{\phi_{Min}^{MF}}{E_{Min}} + \frac{1 - \phi_{Min}^{MF}}{E_{Coll}} \right)^{-1} \tag{3.4}$$

and

$$E_{EFM} = \left(1 - \phi_{pores}^{EFM}\right) \left(\frac{\phi_{Min}^{EFM}}{E_{Min}} + \frac{1 - \phi_{Min}^{EFM}}{E_{NCP}} \right)^{-1} \tag{3.5}$$

Here E_{coll}, E_{Min}, and E_{NCP} are the elastic moduli of the collagen, mineral, and non-collagenous proteins, respectively.

To account for the porosity in the composite models, we assume that all pores are located in the extrafibrillar space as opposed to within the fibers; the prefactor in Equation 3.5 accounts for a reduction of E_{EFM} caused by the volume fraction of pores in the EFM, ϕ_{pores}^{EFM}. This fraction can be determined from the total volume fraction of pores, ϕ_{pores} , measured in our experiments. The pore volume fraction

is measured by analyzing focused ion beam enabled tomographic SEM images of bone pillars. More detail on this process is available in Section 3.7.

To calculate ϕ_{MF}, we note that in a hexagonal array of fibers, the relative fraction of the matrix as a function of the spacing between the fibers, s , is given by

$$\phi_{pores}^{EFM} = \frac{\phi_{pores}}{\phi_{EFM}} \tag{3.6}$$

$$\phi_{EFM} = 1 - \phi_{MF}\phi_{EFM}\,[s] = 1 - \frac{2\pi r_{MF}^2}{3^{\frac{1}{2}}\,(2r_{MF} + s)^2} \tag{3.7}$$

where ϕ_{MF} is the volume fraction of MFs. The average radius of the pores is some linear fraction, x, of the spacing between fibrils, so we can relate s and x through:

$$x\,[s] = \frac{s - s_{solid}}{2r_{pores} + s_{solid}} \tag{3.8}$$

Here, s_{solid} is the extrafibrillar linear spacing if no pores were present; we assume s_{solid} to be $\sim$ 12 nm based on [54] and r_{pores} is 20.8 nm, measured in this work for the ordered phase. It is reasonable to assume that the linear fraction of the pores can be related to their volume fraction in the EFM through $x^3 \sim \phi_{flaw}^{EFM}$, which allows us to calculate $s = 36.5nm$, $\phi_{EFM}^{ord} = 0.51$ and $\phi_{flaw}^{EFM} = 0.096$ for the ordered phase.

For the disordered phase, the hexagonal geometrical argument is not applicable, but by constraining the pores to the EFM as described earlier, we can assume that ϕ_{EFM} scales with ϕ_{pores} ; that is ϕ_{pores}^{EFM} is constant across both phases. To calculate the fraction of EFM in the disordered phase, ϕ_{EFM}^{disord} , we scale ϕ_{EFM}^{ord} by the ratio of pore volume fractions in the two phases 3.9, resulting in $\phi_{EFM}^{disord} = 0.63$.

$$\phi_{EFM}^{disord} = \frac{\phi_{pores}^{disord}}{\phi_{pore}^{ord}}\phi_{EFM}^{ord} \tag{3.9}$$

Next, we can resolve the remaining volume fractions from Equations 3.3-3.5 in terms of the fraction of total mineral that is extrafibrillar, as ϕ_{EF}^{Min} . In this context, the fraction of the mineral that is intrafibrillar is simply

$$\phi_{IF}^{Min} = 1 - \phi_{EF}^{Min} \tag{3.10}$$

To determine the total mineral volume fraction, ϕ_{Min}, we define the total intrafibrillar mineral fraction, ϕ_{MinIF} in two ways:

$$\begin{aligned} \phi_{MinIF} &= \phi_{MF}\phi_{Min}^{MF} \\ &= \phi_{Min}\phi_{IF}^{Min} \end{aligned} \tag{3.11}$$

where ϕ_{Min}^{MF} is the fraction of the MF that is mineral and ϕ_{IF}^{Min} is the fraction of the total mineral that is intrafibrillar (note ϕ_{MinIF} and ϕ_{IF}^{Min} are not equivalent). Equating the parts of Equation 3.11 , we get

$$\phi_{Min} = \frac{\phi_{MF}\phi_{Min}^{MF}}{\phi_{IF}^{Min}} \tag{3.12}$$

Using similar relations for the EFM, we can solve for the fraction of EFM that is mineral, ϕ_{Min}^{EFM}

$$\begin{aligned} \phi_{MinEF} &= \phi_{EFM}\phi_{Min}^{EFM}\phi_{MinEF} \\ &= \phi_{Min}\phi_{EF}^{Min}\phi_{Min}^{EFM} \\ &= \frac{\phi_{Min}\phi_{EF}^{Min}}{\phi_{EFM}} \end{aligned} \tag{3.13}$$

With this series of relations dependent inherently on ϕ_{EF}^{Min} , all variables that define $E_{MFmodel}$ can be solved for. The main assumed parameter in the MF model is the fraction of the MF that is mineral. We physically use this as a constraint as it is this is that is the amount of mineral that a MF can internally accommodate. We assume this to be ~ 0.42 as analytically calculated by Jäger and Fratzl [41] and corroborated by Nair et al. [55] via molecular dynamics simulations. We tabulate the elastic properties of the fundamental constituents, E_{coll} , E_{Min} , and E_{NCP} , as well as other assumed parameters, used in the calculations presented here in Table 3.5. We account for the anisotropy in the elastic contributions of collagen and mineral by using the transverse orientation values of E_{coll} and E_{Min} , respectively, for the ordered phase. For the disordered phase we use the mean values of the transverse and axial E_{coll} and E_{Min}

Using *Mathematica*, the system of equations is solved for both the ordered and disordered phase by setting $E_{MFmodel}$ equal to their respective mean elastic moduli as measured in this work via nanoindentation, 16.3 GPa for ordered, and 21.0 GPa

for disordered(See Section 3.2). It is important to note that the eigenstress model formulation above accounts for porosity by effectively reducing the E_{Min} and E_{NCP} contributions to E_{EFM} (Eq. 3.5) but the flaw volume fraction is initially not an inherent part of ϕ_{EFM} . We account for this by adjusting the volume fractions, as shown in Appendix A. The final resulting volume fractions and distributions are reported in Table 2 for both phases. We calculate that $\sim$ 68.8% of the mineral is extrafibrillar in the ordered phase and 77.9% in the disordered phase. This falls in line with the literature that suggests most the mineral is located outside the fibril [53, 57]. Although this model only considered dry bone, it is noteworthy that the ϕ_{EF}^{Min} is just the percentage of total mineral fraction ϕ_{Min} that is outside the fibril and thus could remain constant even if ϕ_{Min} decreased by introducing water.

Parameter	Description	Value	Reference
ϕ_{Min}^{MF}	fraction of MF that is mineral	0.42	[41]
ϕ_{Col}^{MF}	fraction of MF that is collage	0.58	[41]
ϕ_{pores}	fraction of bone that is porous ord,disord	0.58	present study
$r_{MF}[nm]$	radius of MF	50	[29]
$r_{flaws}[nm]$	average radius of flaws {ord, disord}	{20.8,18.6}	present study
s_{solid}	non-porous linear spacing between ordered MF	12	[54]
$E_{Min}[GPa]$	elastic modulus of mineral	{100,128}	[54]
$E_{coll}[GPa]$	elastic modulus of dry collagen	{7.5,10.65}	[58, 59]
$E_{NCP}[Gpa]$	elastic modulus of non-collagenous proteins	1	[54]
$E_{ord}[Gpa]$	elastic modulus of ordered phase	16.3	present study
$E_{disord}[Gpa]$	elastic modulus of disordered phase	21	present study

Table 3.1: MF and CMF model parameters

Variable	Description	Ordered	Disordered
ϕ_{Min}	fraction of tissue that is mineral	0.655	0.710
ϕ_{Coll}	fraction of tissue that is collagen	0.282	0.217
ϕ_{NCP}	non-collagenous protiens volume fraction {ord,disord}	0.013	0.013
ϕ_{MF}	mineralized fibril volume fraction	0.486	0.374
ϕ_{CMF}	coated mineralized fibril volume fraction {ord, disord}	0.794	0.640
ϕ_{EFM}	extrafibrillar matrix volume fraction {MF,CMF}	{.541,.206}	{0.626,0.360}
ϕ_{EF}^{Min}	fraction of mineral that is extrafibrillar	.688	.779
ϕ_{IF}^{Min}	fraction of mineral that is intrafibrillar	.312	.221
ϕ_{Min}^{EFM}	fraction of EFM that is mineral {MF,CMF}	{0.878,0.84}	{0.883,0.866}
ϕ_{NCP}^{EFM}	fraction of EFM that is NCP {MF,CMF}	{0.026,0.064}	{0.021,0.038}
ϕ_{pores}^{EFM}	fraction of EFM that is pores {MF, CMF}	0.096	0.096
k_{CMF}	stress concentration factor	1.09	1.08

Table 3.2: Results of MF and CMF models

Stress Concentrators from CMF model

Recalling that a the stress concentration factor (Equation 3.2) in this context is only valid when the reinforcing fiber is stiffer than the matrix. With this in mind, we formulate the CMF model by increasing the volume fraction of the mineral in the MF. This is done by taking the contribution of the mineral from the extrafibrillar matrix (EFM) and reallocating it to the surface of the new CMF (Figure 3.6a). This results in increasing the stiffness of the fibril with respect to the EFM; because the volume fractions of the fundamental constituents are constant from the MF to the CMF model, the two model are equivalent in terms of the elastic properties of the composite, $E_{MFmodel} = E_{CMFmodel}$. Similar to the MF model, we define the elastic modulus of the CMF composite as

$$E_{CMFmodel} = \left(\frac{\phi_{CMF}}{E_{CMF}} + \frac{1 - \phi_{CMF}}{E_{EFM}} \right)^{-1} \tag{3.14}$$

where the elastic modulus of the CMF unit and EFM, E_{CF} and E_{EFM} are represented as

$$E_{CMF} = \left(\frac{\phi_{Coll}^{CMF}}{E_{Coll}} + \frac{\phi_{MinIF}^{CMF}}{E_{Min}} + \frac{1 - \phi_{Col}^{CMF} - \phi_{MinIF}^{CMF}}{E_{Min}\left(1 - \phi_{flaws}^{EFM}\right)} \right)^{-1} \tag{3.15}$$

and

$$E_{EFM} = \left(1 - \phi_{flaws}^{EFM}\right) \left(\frac{\phi_{Min}^{EFM}}{E_{Min}} + \frac{1 - \phi_{Min}^{EFM}}{E_{NCP}} \right)^{-1} \tag{3.16}$$

The first and second terms in Equation 3.14 are the fractions of the CMF that are collagen and internal mineral, respectively, defined as

$$\phi_{Coll}^{CMF} = \phi_{Coll}^{MF} \left(\frac{\phi_{MF}}{\phi_{CMF}} \right) \tag{3.17}$$

$$\phi_{MinIF}^{CMF} = \phi_{Min}^{MF} \left(\frac{\phi_{MF}}{\phi_{CMF}} \right) \tag{3.18}$$

The third term in Equation 3.15 reflects the contribution of the mineral on the external surface of the fibril to the CMF stiffness. As explained in the MF section,

we have restricted porosity to the extrafibrillar matrix. The elastic modulus of the mineral is adjusted for this porosity in the third term.

The remaining mineral in the tissue composes a fraction of the EFM, ϕ_{Min}^{EFM} ; this is given by

$$\phi_{Min}^{EFM} = \frac{\phi_{Min} - \left(1 - \phi_{Coll}^{CMF}\right)\phi_{CMF}}{1 - \phi_{CMF}} \tag{3.19}$$

where the term $\left(1 - \phi_{Coll}^{CMF}\right)\phi_{CMF}$ is the fraction of tissue that is mineral and part of the CMF, with $1 - \phi_{CMF} = \phi_{EFM}$

In a similar fashion to the MF model, the unknown fractions can be solved for in terms of one unknown, in this case ϕ_{CMF} . In order to calculate a physically valid stress concentration factor in this the CMF context, we determine ϕ_{CMF} such the CMF that is stiffer than the EFM in Figure 3.6. We plot E_{CMF} , E_{EFM} , and $E_{Ordered}$ (Fig 3.5a)or $E_{Disordered}$ (Fig 3.5b) as functions of ϕ_{CMF} for $\phi_{MF} \leq \phi_{CMF} \leq \phi_{fmax}$. This range physically represents the limits of ϕ_{CMF} from the no reallocated mineral fraction of CMFs up to the fiber close-packing fraction CMFs. We also plot k_{CMF}, the stress concentration caused by CMFs as a function of ϕ_{CMF}. In the context of this CMF model, the physical lower bound for ϕ_{CMF} is the fraction at which E_{CMF} and E_{EFM} are equal and the upper bound is the close-packing fraction of the fibers; this range is shaded and labeled as the k_{CMF} -valid region in Figure 3.5. For both ordered and disordered phases, k_{CMF} only deviates from linearity with respect to ϕ_{CMF} near the upper bound of the region; we take the average ϕ_{CMF} in this region and calculate k_{CMF} to be 1.09 for the ordered phase and 1.08 for the disordered. These results are recorded in Table 3.5. We now compare these values to the stress concentration that arises from the pores (surface and internal) calculated in the next section.

Stress concentration form flaws

We can define the stress concentrations that arise from the internal flaws as $k_{internal}$ and those from surface flaws as $k_{surface}$. If we simplify the flaws to be round pores in an isotropic continuum, we can approximate $k_{internal}$ as the stress concentration due to the internal spherical voids in a continuum body given by Timoshenko and Goodier [61] as

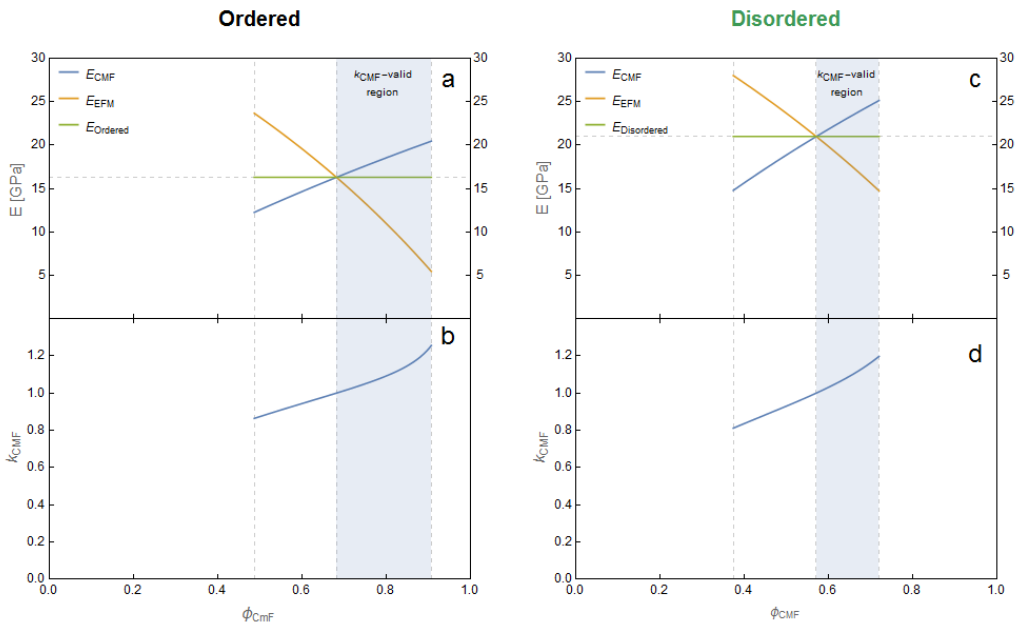

Figure 3.7: Elastic Properties of CMF model. a,c) Show the elastic modulus of the CMF, EFM, and corresponding, composite ordered (a) or disordered (c). The composite moduli are constant because an increase in ϕ_{CMF} corresponds to reallocated mineral from the EFM to the CMF, thus the overall composite properties do not change. The plots are shown with the lower bound of ϕ_{CMF} corresponding to ϕ_{MF} and the upper bound corresponding to the close packing of the fiber, 0.9069 for hexagonally close packed and ~ 0.72 for disordered fibers [60]. b,d) Show the stress concentration k_{CMF} due to the CMF. The shaded region, showing where k_{CMF} is valid, has a lower bound at the fraction at which E_{CMF} and E_{EFM} are equal and an upper bound at the close packing fraction.

$$k_{internal} = \frac{27 - 15\nu}{2\,(7 - 5\nu)} \tag{3.20}$$

where ν is the Poisson's ratio. Taking $\nu = 0.3$ for bone [62], we calculate $k_{internal}$ to be 2.05. With a similar assumption of circular pores in an isotropic continuum, we can approximate an upper bound for $k_{surface}$ as the stress concentration of a hole on the side of a plate, given by Inglis [63] as

$$k_{surface} = 1 + 2\frac{a}{b} \tag{3.21}$$

where a and b are the major and the minor axes of an ellipse. In this context they are approximated as equal and we calculate $k_{surface} = 3.00$

3.6 Comparison of stress concentrators

To recapitulate, we calculated the stress concentrations that arise from each relevant contribution in small-scale trabecular bone samples: the stiff fiber reinforcements in ordered and disordered phases , k_{CMF} = 1.09 and 1.08 , respectively, the internal flaws $k_{internal}$ = 2.05 , and the surface flaws, $k_{surface}$ = 3.00 for both phases. This shows that the strongest stress concentrators in the system are the surface flaws, or pores, consistent with the experimental observations. This result gives us a starting point to justify the hypothesis that serves as the underlying mechanism for failure initiation occurring at the surface flaws in small-scale bone samples. We postulate in the main body of this manuscript that the surface flaws serve as probabilistic stress concentrators and determine the yield stress, or initiation of failure, of the sample.

3.7 Effective stress concentration from surface flaws

In the spirit of a stochastic dislocations source length model constructed by Parthasarathy [64] to predict a smaller-is-stronger size-effect observed in polycrystalline metallic pillars, we conceive a 2D model of a cross-section of radius R and of unit thickness. The cross section is orthogonal the pillar axis (Fig. 3.8b) . We define n flaws, all of which we simplify to circles of mean radii r . The i^{th} flaw is a distance d_i from the surface of the pillar of radius R. There is a surface flaw if the minimum of the set distances, d_i , is less than or equal to r (Equation 3.22). Equivalently, a flaw is effective as a surface flaw if it is a distance $d_i \leq r$ from the boundary of the cross-section. We also define the cumulative distribution function (CDF) of d_i in Equation 3.23 , stating the density of flaws at some distance r drops of with the square of that distance from the surface.

$$min\{d_1, \ldots, d_n\} \leq r \tag{3.22}$$

$$F_{d_i} = 1 - \left(1 - \frac{r}{R}\right)^2 \tag{3.23}$$

We construct Equations 3.24 - 31 to reflect our hypothesis. In Equation 3.24, we define the relation for yield strength, σ_{yield} , as a product of the bulk strength and an effective stress concentration factor, σ_{bulk} and k_{eff} , respectively.

$$\sigma_{yield} = \sigma_{bulk} k_{eff} \tag{3.24}$$

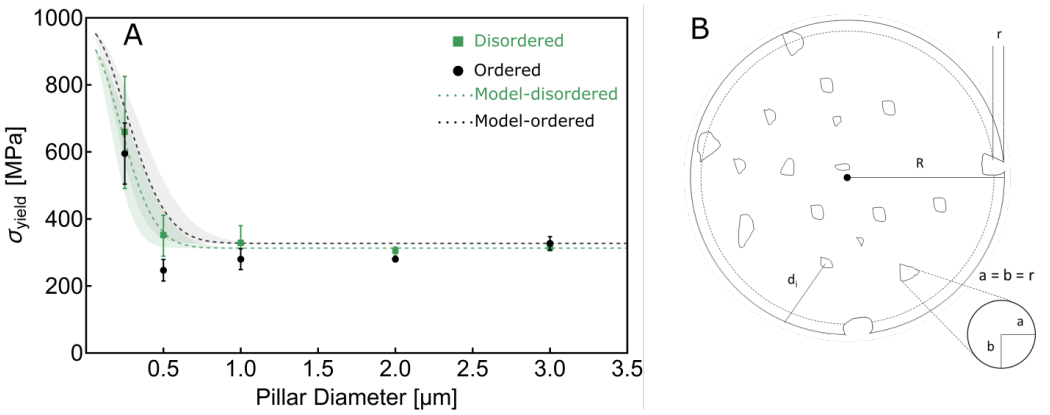

Figure 3.8: Yield strengths across pillar diameters with corresponding model prediction. a) Both the ordered and disordered samples exhibit size independent yield strengths up until the nanometer regime in which there is a dramatic increase in strength. A stochastic flaw-based yielding model is able to quantitatively capture this strengthening in both phases. b) The simplified representation of the 2D slice of unit thickness used in constructing the stochastic surface flaw failure model. The n flaws are approximated to be circular with average radii r and the i^{th} flaw is located a distance d_i from the surface a pillar of radius R. The shaded regions in the model results in (a) indicate upper and lower bound model results when using r values at ± one standard deviation.

For each phase, ordered and disordered, we take the bulk strength to be the experimentally measured yield stress of the 3 μm pillars. We propose that k_{eff} increases with the probability that a surface flaw exists, denoted as P_s in Equation 3.27.

$$k_{eff} = P_s + (1 - P_s)\, k_{surface} \tag{3.25}$$

The upper bound for k_{eff} is $k_{surface} = 3$, as estimated at the end of in Section 3.5.

We substitute Equation 3.25 3.24, stating a pillar becomes stronger as the probability of stress concentration due to surface flaws decreases:

$$\sigma_{yield} = \sigma_{bulk} \left(P_s + (1 - P_s)\, k_{surface}\right) \tag{3.26}$$

We can define the probability, P_s , using the pillar radius by assuming the volume fraction of flaws across the range of pillars is constant. This assumption is reasonable in each phase because the pillars are fabricated in the sub-lamella length scale, meaning the microstructure should be consistent since lamellar interfaces are not present. Keeping in mind the 2D simplification, we define P_s as the probability that

the minimum of the distances of the n flaws in the cross-section is less than or equal to r.

$$\begin{aligned} P_s &= P\left[d_{i_{min}} \leq r\right] = P\left[min\left\{d_1, \ldots, d_n\right\} \leq r\right] \\ &= 1 - P\left[\left\{d_1, \ldots, d_n\right\} > r\right] \\ &= 1 - \left(1 - P\left[d_i \leq r\right]^n\right) \\ &= 1 - \left(1 - F_{d_i}\left[r\right]\right)^n \\ &= 1 - \left(\left(1 - \frac{r}{R}\right)^2\right)^n \end{aligned} \tag{3.27}$$

Here in the third line the D_i are treated as independent variables. Eq. 29 shows the number of flaws, n scales with R^2 , assuming the volume faction of flaws, ϕ , is constant.

$$n = \phi\left(\frac{R}{r}\right)^2 \tag{3.28}$$

To expand the unit thickness cross-section model to a 3D, we can assuming we have l independent slices of unit thickness; this results in nl flaws for the number of flaws in the full pillar. The probability P_s is shown in Equation 3.29.

$$P_s = 1 - \left(\left(1 - \frac{r}{R}\right)^2\right)^{nl} \tag{3.29}$$

The pillars are fabricated to have aspect ratios of 3:1, length to diameter; due to this ratio l scales as $6R$. We can now summarize the yield strength as a function of pillar radius:

$$\sigma_{yield}\left[r\right] = \sigma_{bulk}\left(1 - 2\left(\left(1 - \frac{r}{R}\right)^2\right)^{6\phi\frac{R^3}{r^2}}\right) \tag{3.30}$$

In Matlab, we use image contrast thresholding to identify and quantify the porosity across 42 cross-sections in each phase, ordered and disordered. We calculate and measure ϕ to be 0.0493 for the ordered phase and 0.0590 for the disordered phase and r to be 20.8 ± 11.0 nm for the ordered phase and r = 18.1 ± 9.4 nm for the disordered phase. An example of the cross-sections and identified flaws used for measuring ϕ and r is show in Supplemental Video 3 for disordered phase.

The yield strengths as a function of sample diameter predicted by this model are plotted along with the experimental data in Figure 3.8 and show quantitative agreement between the model and the experimental data. The model predicts a size-dependent yield stress, which is manifested by the ~ 2-fold increase from 327 to 729 MPa in the ordered phase and from 313 to 632 MPa in the disordered phase when pillar diameter is reduced from 3000 nm to 250 nm. This size effect is similar to the 2-fold increase observed experimentally over the same size range. The proposed model is limited in its ability to capture certain deformation processes such as the contribution of porosity to the incipient plasticity, with respect to the postulated extrafibrillar sliding mechanism [46]; more sophisticated modeling, which could incorporate the interactions of all the components of the complex microstructure, would be necessary to fully access these effects. But the agreement between the experiments and the current model supports our hypothesis that the initiation of yielding and failure in small-scale bone samples is governed by the presence of surface flaws and the corresponding scaling with the relative surface area through pillar radius. This is further supported by the our earlier consideration of the possibility of failure initiation from other microstructural stress concentrators, such as internal flaws, $k_internal$, or fibrils, $k_C MF$, in the context of a composite.

To date, measurements of mechanical properties of bone have been primarily focused on larger scales, which would render de-coupling structural and material properties challenging. The investigations of sub-lamellar mechanical properties in trabecular bone have been focused on understanding energy dissipation that arise from unraveling of the non-collagenous proteins in a single molecule context, rather than on strength [19, 65, 66]. The experimentally measured strength of 658 MPa that we report for the 250 nm-diameter disordered samples represent the highest yield strength reported for bone to date. Although the size effect has been suggested [67] and demonstrated [49] for cortical bone ranging from macro- to micro-scale, this work provides insight into the further strength increase in bone samples when their dimensions are reduced from micro- to nano-scale.

All pillars were fabricated in vacuum and the nanomechanical experiments were performed at atmospheric pressure, which caused the bone samples to be dehydrated during compression and indentation. It is expected that the dehydration stiffens the bone due by altering the viscoelastic properties of collagen [50]. We measured the disordered phase of bone to be stiffer than the ordered one and attributed it to a higher degree of mineralization of the fibrils in the former; it can be argued that this

relation will be preserved upon hydration of collagen in both phases. It has also been proposed that water mediates the surface layer nature of HA in bone, providing an amorphous hydrated interface between the nanocrystals [26]. We demonstrate that the post yield behavior is highly contingent on the size of bone samples by attributing the microscale ductility to shearing through the extrafibrillar matrix. Hydration of the mineral surfaces, as well as the non-collagenous proteins in the extrafibrillar matrix, could further increase this ductile behavior response. The role of water on deformation and yielding mechanisms of bone requires a dedicated study, which is outside the scope of the present work.

3.8 Summary and Outlook

Our experiments and results focus on how the post-elastic properties of bone, particularly strength and its variation with sample size, depend on the amount and properties of the extrafibrillar matrix and porosity in two very distinct phases of bone. We observe that each isolated phase of the bone exhibits similar mechanical response in small-scale samples, and we postulate that this occurs because of the common factors within the ordered and the disordered phases, i.e., extrafibrillar matrix and porosity. After considering the effects of other microstructural components, this porosity is what allows the disordered phase of bone to be as mechanically robust as the ordered one. With the ability to isolate, perform TEM analysis (see Chapter 2), and mechanical probe the disordered bone phase we provide new insights about the compressive strength of trabecular bone, specifically that the mechanical strength is virtually identical between the two substantially microstructurally distinct phases because of the prevalent effect of porosity as key mechanism for failure.

Modeling mechanical properties of bone, particularly atomistic ally, has been based on the ordered structure of mineralized collagen fibrils [55] . By investigating ordered and disordered phases of bone, we show that disorder can persist at the nanoscale while microscale yield and post-yield properties are mostly preserved. In this chapter we proposed that this is likely contingent on the presence of an extrafibrillar matrix within the composite structure at these lowest levels of the bone hierarchy.

Efforts at creating biomimetic bone have focused on replicating the ordered arrangement of collagen fibrils to provide a 3D protein scaffold for mineralization [68]. Our results further suggest the microscale arrangement of not just the collagen and mineral, but also the extrafibrillar matrix is paramount for emulating the post-elastic

response of bone in an effort to create mechanically biocompatible scaffolds.

Chapter 4

FRACTURE OF MICRON-SIZED BONE

4.1 Chapter Abstract

The microstructural origins of toughening of bone have not been adequately explored because the challenges associated with performing valid fracture experiments on small-sized samples have precluded developing a quantitative description of bone fracture through its hierarchy. Specific contributions of individual constituents at each level of hierarchy to amplification of bone toughness beyond that of its parts remain elusive. In this chapter, we developed an experimental methodology that probes site-specific fracture behavior of micron-sized specimens. We apply this methodology to investigate and quantify crack initiation and fracture toughness of human bone with sharp cracks. Our findings indicate bone with sharp cracks to be tougher than that with blunt cracks and quantify the crack growth toughness emerging primarily from the underlying fibril microstructure. In the context of the existing R-curve of bone, these experiments reveal a transition between fibril bridging and crack deflection and twist as a function of length scale, providing a quantitative description of how toughness behavior varies with hierarchy.

Adapted from:

Tertuliano, O. A., Edwards, B. W., Meza, L., Deshpande, V. & Greer, J. R. Microscale 3-point bending fracture experiments reveal the emergent damage tolerance of bone. *in preparation*
O.A.T performed the experiments, analyzed the data, and wrote the manuscript.

Meza, L performed FE simulations

4.2 Toughening Mechanisms in Bone

The microstructural origin of bone strength at the tissue level (femur, tibia etc. . .) has been studied extensively in the past four decades; for example it has been generally accepted that its bending strength increases with mineral content [69]. In Chapter 3 micro- and nano-mechanical compression experiments in isolated lamellae have enabled site- and microstructure-specific measurements of bone strength and revealed a "smaller is stronger" trend from the macroscopic tissue down to the nanoscale collagen fibrils [49] . This size effect was attributed to the limited number of failure-initiating critical defects (e.g., pores and interfaces) in small-scale samples relative to macroscale tissue.

Conversely, the complex hierarchy of bone has also been reported to improve toughness, specifically its crack growth resistance. Fracture studies on large-scale, mm-cm bone specimens have revealed toughening mechanisms that are active various length scales: molecular uncoiling and fibril bridging at the nanoscale [70, 71] ; microcracking at the microscale; and uncracked-ligament bridging, crack twist, and deflection at the macroscale. These mechanisms collectively give rise to crack growth resistance manifested by requiring a greater driving force to continuously extend a crack, typically characterized by an "R-curve" [8]. All of these findings are based on experiments conducted on millimeter and larger-sized specimens; these are length scales at which crack twist and deflection around osteons are described as the dominant toughening mechanism. The role of sub-structure at smaller length scales, such as the mineralized collagen fibrils, remains unknown, which precludes the formulation of crack growth resistance in bone as a function of relevant microstructural components within its hierarchical construct.

To determine and quantify the mechanical interplay among features at each level of hierarchy necessitates quantifying their individual contributions to the toughness. Fracture toughness experiments are classically standardized for the macroscale and, for the most part, have not been pursued for small-scale specimens, in contrast to the now-ubiquitous experiments on measuring compressive strengths of nano- and micro-sized materials [42, 43, 72]. This is because 1) linear elastic and elastic-plastic fracture mechanics (LEFM, EPFM) place lower limit restrictions on specimen size and 2) adapting a standard for fracture experiments that provide a valid measure of toughness at the microscale poses significant fabrication and experimental difficulties [73]. Methods based on new fracture geometries have been proposed for the microscale, but the asymmetric loading conditions around the notch tip of micro-

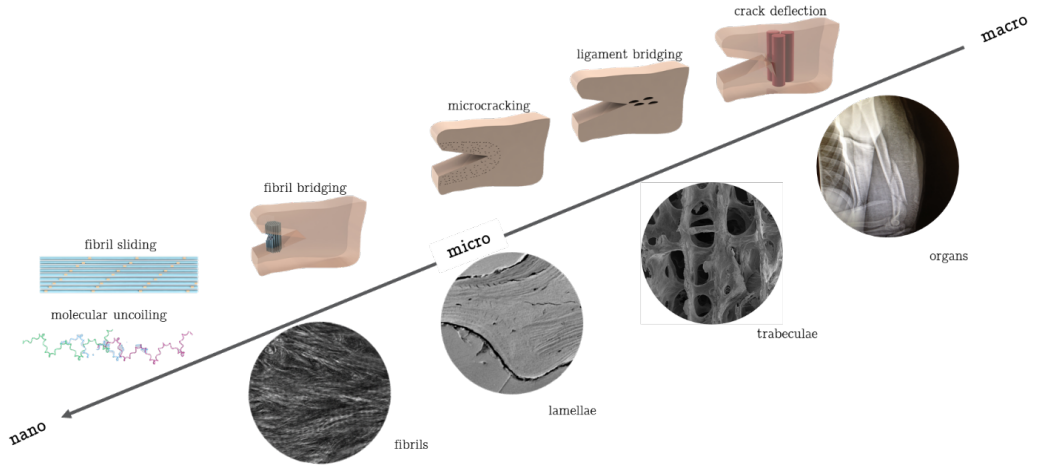

Figure 4.1: Multiscale Toughening Mechanisms in Bone

cantilevers, premature failure at elastically-fixed boundary conditions of clamped beams limit viability of these techniques, particularly for heterogeneous materials like bone [74].

We developed an experimental methodology that enables conducting *in-situ* 3-point bending fracture experiments on free-standing micron-sized beams, similar to the standardized macroscale single edged notched bend experiment15. We validated this methodology using singe crystal silicon as a standard and measured crack initiation and growth toughness of human bone through stable crack growth at the micrometer scale. We describe and quantify this toughness of bone in terms of the underlying fibril microstructure using a bridging zone model [75]. We discuss the emergence of the crack growth toughness in bone through the transition from this fibril bridging mechanism at the microscale to crack deflection and twist mechanisms reported at larger crack lengths.

4.3 Developing Microscale 3-point Bending Fracture Experiment

Specimen Dimensions

As described, performing fracture experiments at the microscopic length scales is challenging partially due to meeting dimensional restrictions set by small scale yielding conditions (SSY) necessary for the applicability linear elastic fracture mechanics (LEFM). To this end, the American Society of Testing and Materials (ASTM) has standardized experimental fracture geometries and cataloged experimental procedures, specimen dimensional ratios, and handbook solutions for reported valid fracture toughness values[76]. These standards have been developed over decades

of round robin experimental and numerical results. The specimen dimensions used in the present work are calculated to meet SSY and dimensional ratios for the standardized single edge notched bending (SENB) fracture geometry as shown in Figure 4.2. To insure a valid measure of critical stress intensity K_{IC}, the relevant beam dimensions must be about an order of magnitude greater than the characteristic plastic (or inelastic in the case of bone) deformation zone r_p. In the context of the SENB geometry, this criteria is given by

$$a_0, b, B \geq 10 r_p \tag{4.1}$$

where B is the thickness (out of plane dimension not show in Fig) and b is the uncracked ligament length $B - a_0$. In plane strain conditions, the plastic radius r_p is defined as

$$r_p = \frac{1}{6\pi} \left(\frac{K_{IC}}{\sigma_y} \right)^2 \tag{4.2}$$

where σ_y is the yield strength of the material. Using the dimensional ratios defined for the SENB geometry by the ASTM handbook, specifically B $0.5W$ - where W is the thickness seen in Fig 4.2a - we get the dimensional criteria that $w \geq r_p$. Given an estimated macroscale K_IC of 1 MPa $m^{1/2}$ for both silicon and bone [77, 78], we show in Figure 4.2b a plot of the estimated allowable specimen thickness for σ_y values up to 7 GPa, which represents the upper bound of failure strengths reported for silicon in literature [79]. We see this allows very small specimen thickness (100s of nms) for silicon. As a conservative estimate for bone we use a σ_y of 320 MPa (recalling our results from Chapter 3) and calculate that minimum specimen thickness $W \sim 10\mu m$ as shown in figure 4.2c.

Generalized Specimen Preparation

In order to create a microscale fracture geometry that adheres to the calculated specimen dimensions, we employ a combination of nanofabrication techniques and a TEM lift out procedure. This procedure is outlined in Figure 4.3. By dry etching rectangular patterns into silicon 4.3a-c, we first create a set of three supports, two of which will define the span (S) of the specimen as in Fig 4.2 and one of which is sacrificial. Next, using focused ion beam (FIB) milling in an SEM, we begin to carve out a beam geometry until a cantilever is produced as shown in Figures 4.3d-f. This is similar to the milling procedure used in Chapter 3 for the cylindrical pillars.

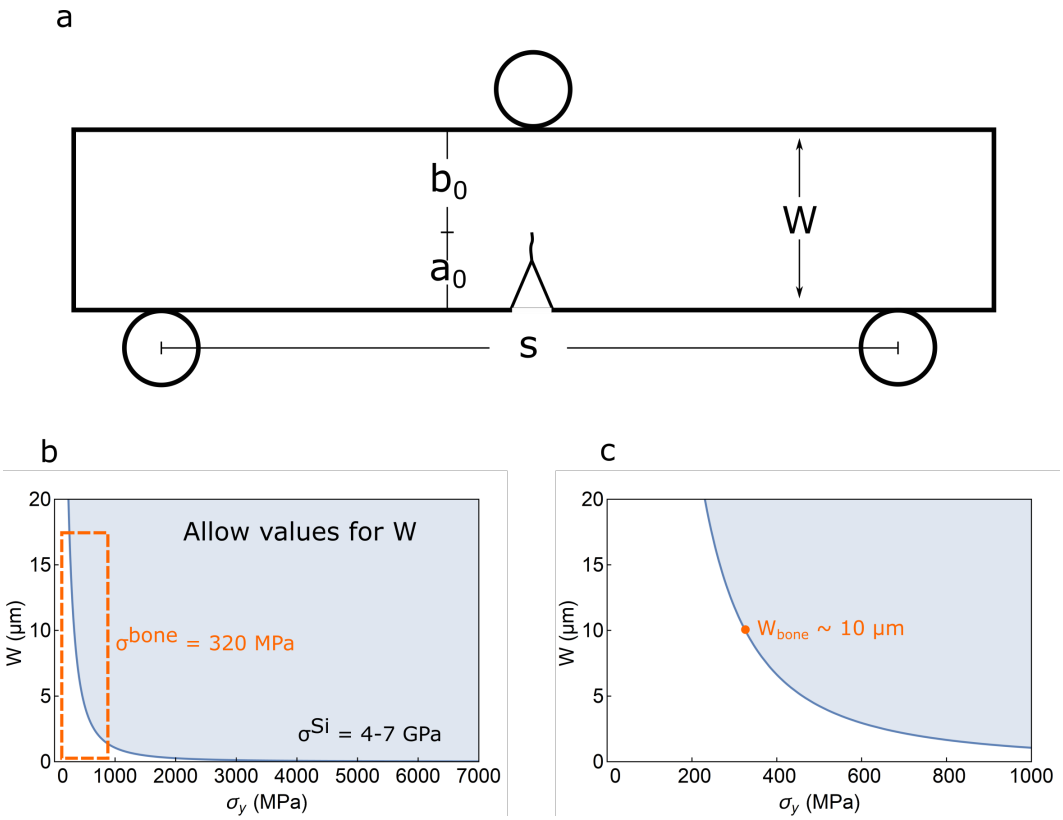

Figure 4.2: SENB LEFM Dimensions. a) diagram of the standardized macroscale single edge notched specimen alongside plots of allowable beam thickness for measuring K_IC of silicon (b) and bone (c) based on plain strain small scale yielding criteria.

We next glue the specimen to a nano-manipulator in the SEM using an Pt based organometallic glue, and subsquentially free the specimen from the bulk material as seen in Figures 4.3d-f. The specimen is transferred on to the 3 silicon supports, glued to the third sacrificial support and freed from the nano-manipulator. We apply a crack starter notch to the specimen using the FIB; we place the manipulator on top of the specimen (without any glue) to hold the it in place while the the sacrificial supported is milled away. This results in the free standing microscale 3-point bend fracture geometry as depicted in Figure 4.3i. Further information on the etching procedure used in this technique can be found in Appendix B.

4.4 Validating Fracture Experiments on Silicon

To validate this new microscale methodology in the context of linear elastic fracture mechanics (LEFM), we first performed experiments on single crystalline silicon beams. We conducted *in situ* 3-point bending fracture experiments in an SEM

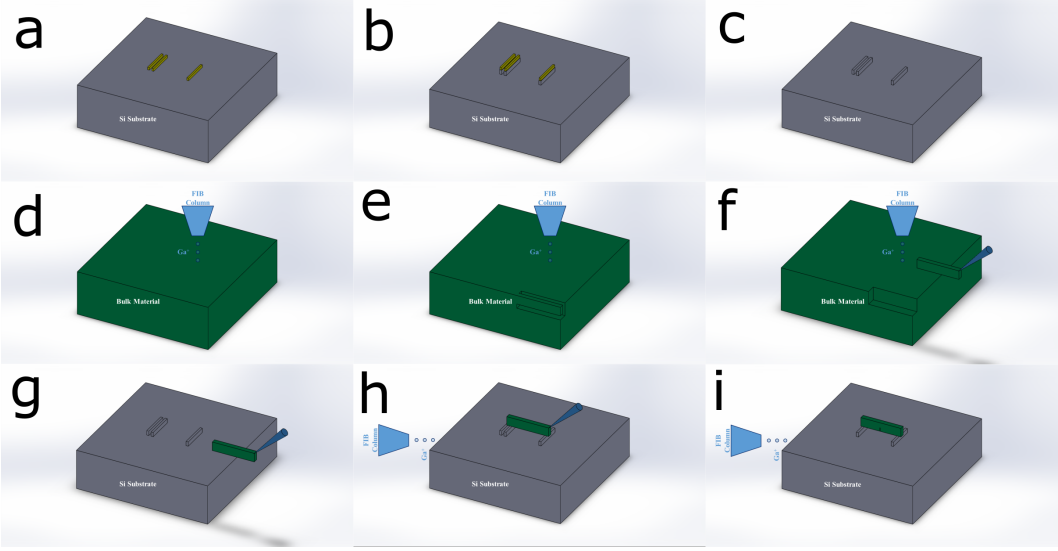

Figure 4.3: TEM Liftout procedure for Fracture Specimens.

using a nanoindenter (Nanomechanics Inc) equipped with rounded diamond wedge indenter tip of radius r = 3.12 µm. This is shown in Figure 4.4 for a silicon beam geometry. The beams are loaded at a displacement rate of 5 nm/s until failure while the load and displacement data is recorded. A dynamic stiffness is also recorded to track the compliance of the specimen. This is done by superimposing a 2 nm displacement amplitude oscillation at 45 Hz on to the monotonically increasing applied displacement; the dynamic displacement and load responses produce a dynamic stiffness[80]. The measured dynamic stiffness is then corrected for the contact stiffness contributions of the wedge and supports in the experiment using Hertzian mechanics solutions [44].We briefly describe this as follows.

Correcting displacement and stiffness for contact compliance

Because the contact points at the wedge tip and supports have finite stiffnesses (non-rigid contact), they contribute to the experimentally measured dynamic stiffness and displacement. Figure 4.5 shows the experimental system is modeled as a series of springs and the contributions to the measured stiffness are given by

$$\begin{aligned} S_{measured} &= \left(S_{specimen}^{-1} + S_{wedgetip}^{-1} + S_{supports}\right)^{-1} \\ S_{specimen} &= \left(S_{supports}^{-1} - S_{wedgetip}^{-1} - S_{supports}\right)^{-1} \end{aligned} \tag{4.3}$$

where the S refers to the respective stiffnesses. To quantify the contributions of the

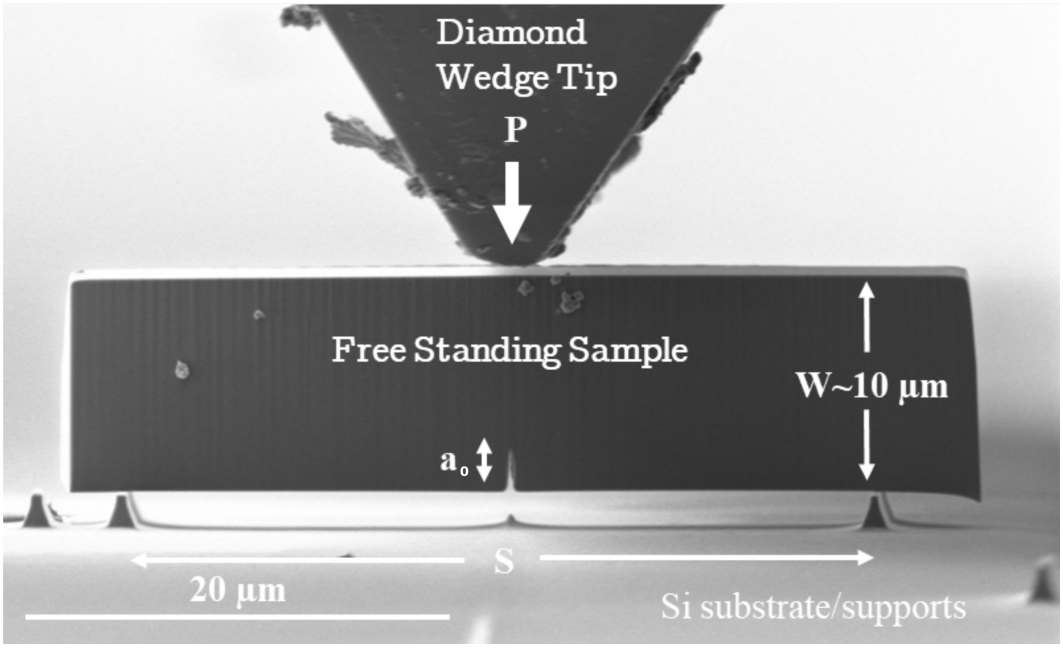

Figure 4.4: Microscale 3pt bend fracture of silicon

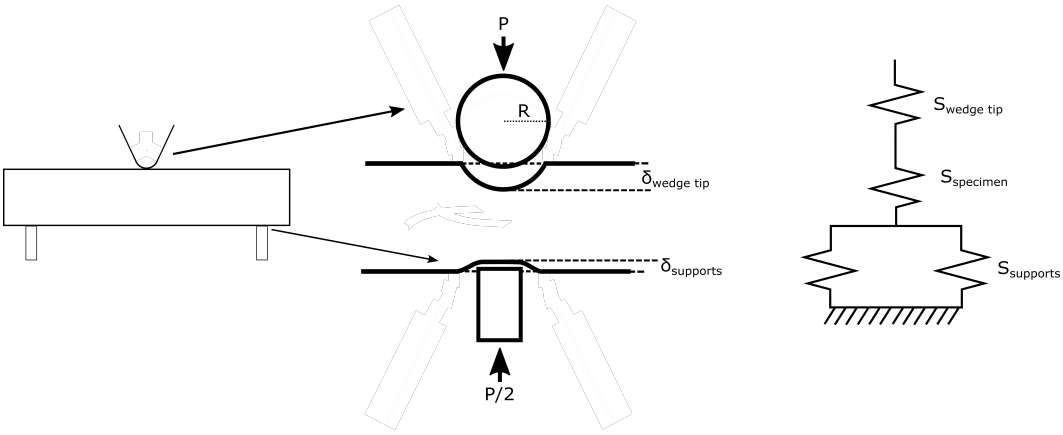

Figure 4.5: Microscale 3pt Bend Contact Model

diamond wedge tip and the silicon supports we use contact mechanics models that provide theoretical contact stiffnesses of the geometries. Each support is considered as a flat punch indenting into an elastic half space[42, 44]. This stiffness is given by

$$S_{supports} = 2E^* \left(\frac{A}{\pi}\right)^{1/2} \tag{4.4}$$

where E^* is the reduced modulus of the materials in contact and A is the area of the contact. The reduced modulus is calculated as follows:

$$E^* = \left(\frac{1 - \nu_1^2}{E_1} + \frac{1 - \nu_2^2}{E_2} \right)^{-1} \tag{4.5}$$

where the E_i and ν_i are the elastic moduli and Poisson's ratios, respectively. The contribution from the wedge tip ($S_{wedgetip}$) is modeled as the contact between a cylinder and a flat plane [81], given by

$$S_{wedgetip} = B\pi E^* \ln \left(\frac{B^3 \pi E^*}{PR} \right)^{-1} \tag{4.6}$$

Here R is the wedge tip radius, B is the thickness of the beam, and P is the load. We use 1190 MPa for the elastic modulus of the diamond tip, and for (100) silicon, we use 130 MPa for E_i and 0.22 for ν_i [82]. We validate this model in the present work by performing indentation experiments on a silicon walls as shown in Figure 4.6a. These walls are the geometries of the silicon beams prior to being extracted for the 3-point bending experiment (See Appendix B). The indentation experiment allows isolation of the wedge contact from the other contributions to $S_{measured}$ in Equation 4.3. Figure 4.6 shows the experimental contact stiffness data for the walls as well as the results of the contact model in Equation 4.6, revealing quantitative agreement between the experiment and the contact mechanics solution.

Using theoretical contributions of the supports and the wedge tip contact, we correct the experimentally measured contact stiffness of the 3-point bending geometry (Fig 4.6c). In Figure 4.6d, we also correct the measured displacement- i.e., remove contributions from total measured displacement from indentation represented in Figure 4.5 by the δ. As expected, these corrections show stiffening in the elastic response of the specimen. The corrected data is used to calculate relevant fracture results in the following sections of this chapter.

Fracture Results of Silicon Specimen

In the silicon fracture specimen we introduce the initial notches of length a_0 oriented such that the crack is defined by the [110] plane and travels in the (100) direction. Our experiments revealed that the silicon specimens respond generally linear elastically up to a load of 3.28 ± 0.28 at a displacement of 106.9 ± 10.1 nm and then fail catastrophically as shown in Figure 4.7a and Supplemental Video 4. We calculate the linear elastic mode I stress intensity factor K from the load and specimen dimensions shown in Figure 4.4

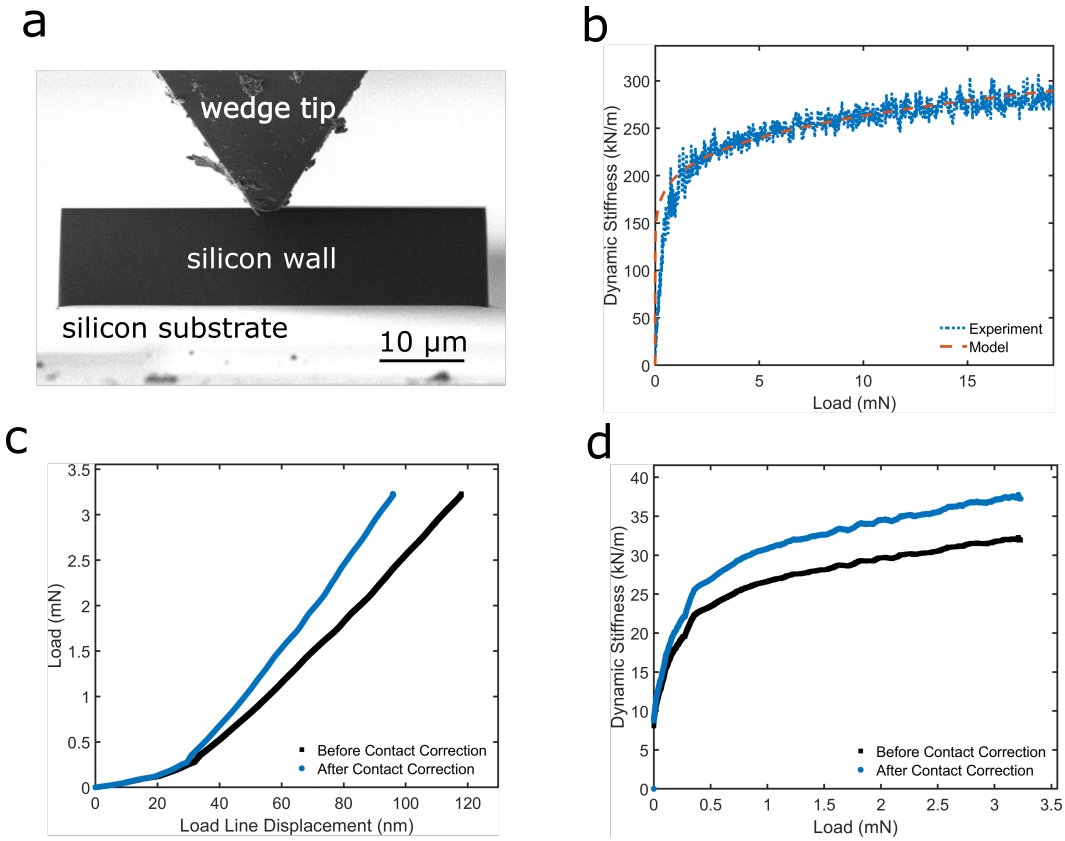

Figure 4.6: Silicon Contact Stiffness Corrections

$$K_{I(i)} = \frac{P_i S}{B W^{\frac{3}{2}}} f\left(\frac{a_i}{w}\right) \tag{4.7}$$

where P_i and a_i are the instantaneous load and crack length. In the present context $a_i = a_0$. The $f(a_i/w)$ dimension less geometry factor for the 3-point bend specimen is given by

$$f\left(\frac{a_i}{w}\right) = \frac{3\left(\frac{a_i}{w}\right)^{1/2}\left[1.99 - \left(\frac{a_i}{w}\right)1 - \left(\frac{a_i}{w}\right)\left(2.15 - 3.39\left(\frac{a_i}{w}\right) + 2.7\left(\frac{a_i}{W}\right)^3\right)\right]}{2\left(1 + 2\left(\frac{a_i}{w}\right)\right)\left(1 - \left(\frac{a_i}{w}\right)\right)^{3/2}} \tag{4.8}$$

Figure 4.7b shows the K_I results for the silicon specimens. We calculate a the crack initiation toughness or critical stress intensity, K_IC of 0.94 +- 0.08 MPa $m^{1/2}$. We discuss these results in the following section.

Recent work has evaluated the efficacy of proposed methodologies for measuring the toughness of micron-sized materials[74]. The most prevalent small-scale fracture

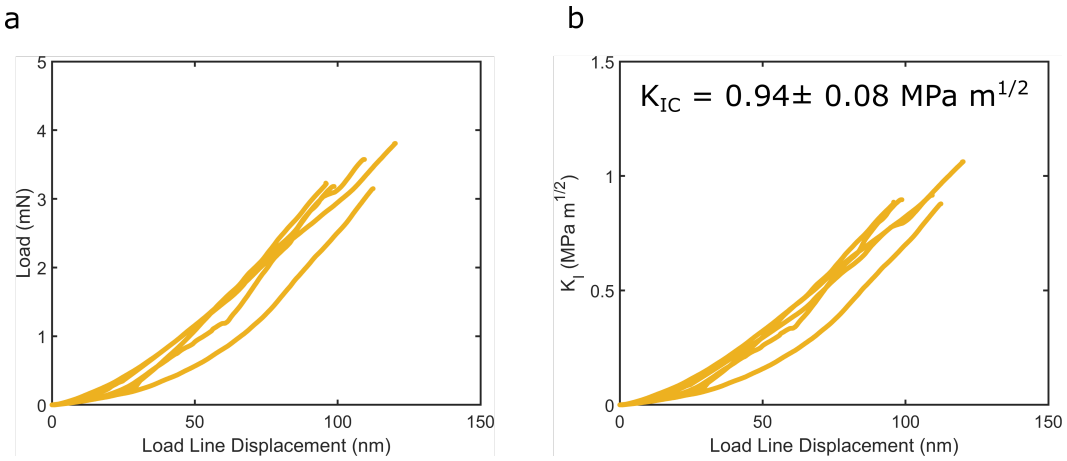

Figure 4.7: Silicon K_{IC}

geometry, a notched cantilever, was used to measure an average K_{IC} of 0.76 MPa $m^{1/2}$ in single crystal silicon [74] , a result in the lower range of 0.7-1.3 MPa $m^{1/2}$ reported in literature [77, 83]. The asymmetric loading about the notch tip in a cantilever geometry renders the K_{IC} reported from such experiments to be that of an inherently mixed-mode I and II fracture, not a true K_{IC}. In the cantilever geometry, the initial notch orientation β relative to the applied load changes as a function of the cantilever deflection angle, also β. Stress based mode mixity given by

$$\psi = \arctan \frac{K_{II}}{K_I} \tag{4.9}$$

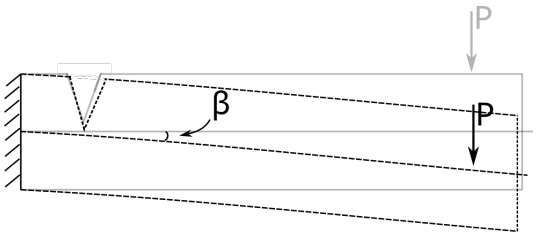

Figure 4.8: Cantilever Mode Mixity

As shown in Figure ,the mixed mode nature of the cantilever arises from the inherent evolution of a component of the applied load parallel to the notch orientation as the beam deflects with the angle β. The Ks are proportional to the directionally resolved component of the applied load P; this gives $K_{II} \sim \sin\beta$ and $K_I \sim \cos\beta$ and $\psi = \beta$ for the cantilever geometry often employed in literature. The symmetric loading of microscale 3-point beam bending method developed in this work allows

for measuring a pure mode I K_{IC} of 0.94 MPa $mm^{1/2}$, consistent with 1 MPa $mm^{1/2}$ reported from fracture experiments conducted on macroscale single crystal Si specimens [77, 83, 84].

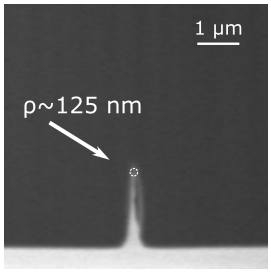

Figure 4.9: Notch Radius of Silicon Specimen

The fracture toughness was measured from specimens with finite notched radii ($\rho \leq 125nm$, 4.9a) rather than ones containing atomically sharp precracks necessary to measure a true toughness [76]. In a brittle material, the apparent toughness decreases with increasing crack tip radius [85, 86]. The Creager and Paris formulation of this concept estimates states $K_C \sim \sigma\sqrt{\pi a}(1 + \frac{\rho}{a})$,where a is the crack length, and σ is the remote applied tensile stress [85]. If ρ is relatively large the toughness becomes an irrelevant criteria, but in the limit of a relatively small radius, $\frac{\rho}{a} \rightarrow 0$, the Irwin criteria for sharp cracks is recovered, $K_C \sim \sigma\sqrt{\pi a}$. Silicon samples used to validate the experimental methodology in this work had a $\frac{\rho}{a} \leq 0.05$, which suggests that the toughness of notched silicon specimens should be within 5% of that of atomically-sharp precracked silicon, i.e., the error in the reported K_{IC} originating from a finite sized notch should be low. The pure mode I conditions of relatively small notch radii and free boundary conditions enabled by the methodology developed in this work allow the measurement of valid fracture toughness of micro-sized materials using established macroscale standards.

4.5 Crack Initiation Toughness of Bone Lamellae

Given the LEFM results from Section 4.4, we investigate crack initiation toughness of bone at the lamella length scale (3-7 μm). We first characterize the bone strength and elastic properties using the bending geometry, followed by a cursory description of the fatigue precracking procedure and the results of the crack initiation toughness.

Figure 4.10 shows the final specimens in the prespective of the trabecular bone architecture as well as the underlying fibril microstructure. We polish bone trabeculae in order to identify the lamellar structure in individual trabeculae as shown in Figure

4.10b. We then use the TEM liftout procedure described in Section 4.3 to carve out the bone specimen for the fracture experiment as shown in Figure 4.10c. The nominal orientation of collagen fibrils in the prepared samples was parallel to the span of the specimens, as shown in the transmission electron micrograph in Figure 4.10d. This is done to mimic the physiologically relevant "breaking" or crack-arresting orientation of bone [8, 70]. For the fracture experiments, a total of 10 samples were made; similar to the silicon specimens we patterned through-notches of length a_o 0.4W using Ga+ ion beam with the FIB in one half of the specimens. In the other specimens, we carved out shorter notches that were subsequently pre-cracked by fatiguing.

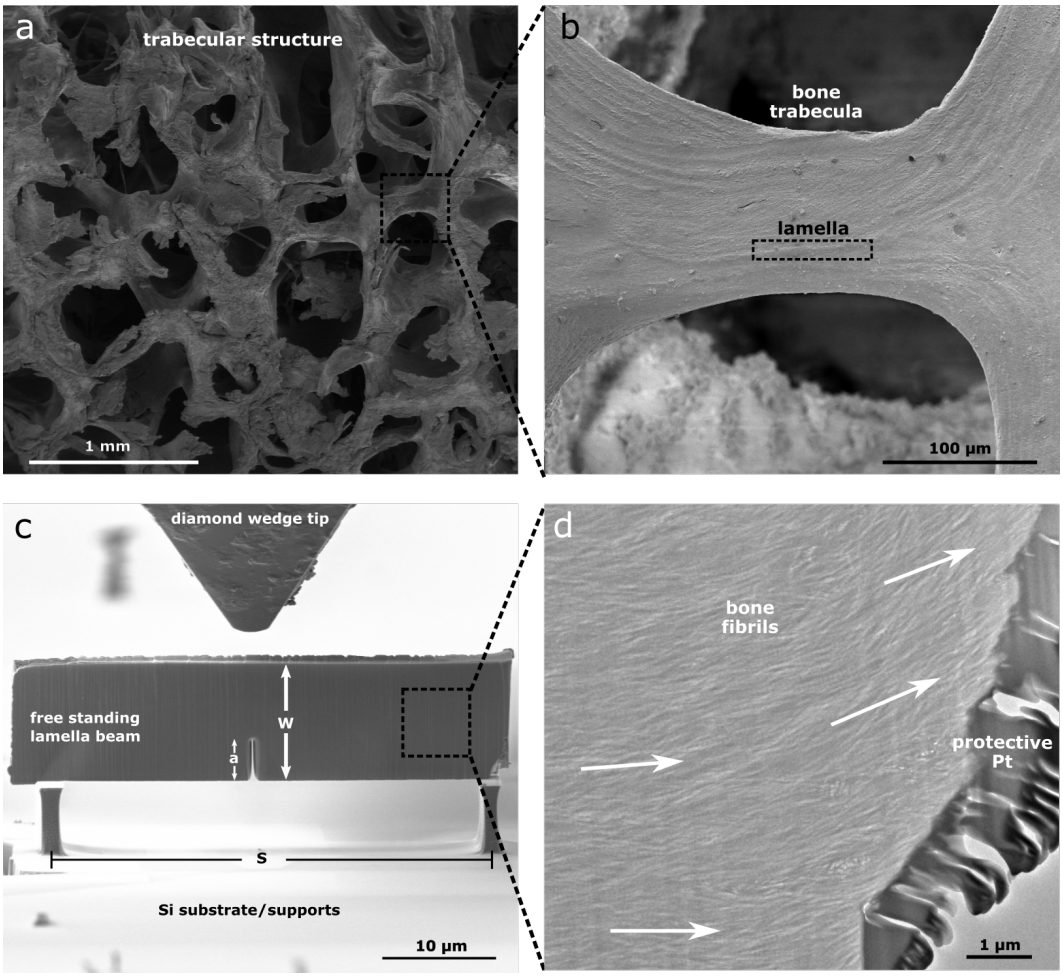

Figure 4.10: Bone Fracture Specimen and Microstructure a) Trabecular architechture from which specimen are extracted. b) Lamellae structure in individual trabeculae from which the fracture specimens are excised as shown in c). d) Transmission Electron Microscopy image showing fibril orientation is mostly aligned with the span of the bone fracture specimens, i.e the crack arresting orientation

Bending Modulus and Strength of Lamellae

We first characterize the bending modulus and strength of bone lamellae using the bending geometry. Figure 4.11a shows specimens prepared similarly to that shown in Figure 4.10, but without a notch. These specimens are loaded and fail catastrophically; Figure 4.11b shows the bending uniform deformation response prior to failure. Figure 4.11c shows the load vs load line displacement response from two specimens. We observe nominally linear elastic deformation with some settling events (indenter and support contacts). One of the specimens also exhibits deviation from linearity near maximum load. The stress vs strain response is plotted in 4.11c. The bending stress σ and strain ϵ are given by

$$\sigma = \frac{3}{2}\frac{PS}{BW^2} \tag{4.10}$$

$$\epsilon = 6uW/S^2 \tag{4.11}$$

where P is the load, u is the load line displacement and the remaining terms are dimensions of the specimen (Figure 4.4). Note this σ represent the maximum tensile and strain in the specimen, i.e., the stress and strain at the bottom of the specimen along the loading line. The elastic modulus is calculated by fitting the middle third of the stress vs strain data. We calculate 21.78 and 18.51 GPa. with an average of 20.15 GPa; these results are in agreement with the $\sim$ 20-27 GPa reported for bone when loaded in its stiffness orientation — parallel to the mineralized fibrils in micrometer specimen, or osteons in millimeter specimens [8, 49]. We measure the bending strength as 566 and 603 MPa. These results are higher than the strength measure for macroscale bending of bone from a variety of animals [39]. Those authors report bending strength ranging from 50-350 MPa using hydrated bone specimens extracted in animals ranging from alligators to elephants to reindeer, which would explain the wide spread in the literature. The results are are from dry bone specimens and thus would be expected to be stronger. Additionally the microstructure orientation of the fibrils in the specimens here are is such that the tensile and compressive forces are acting along the fibril axes (stiff orientation). Generally in brittle materials, a stiffer response correlates to a higher strength. In the present context we take the elastic modulus E as 20.15 $\pm$ 2.31 GPa and the strength as 585 $\pm$ 26 MPa.

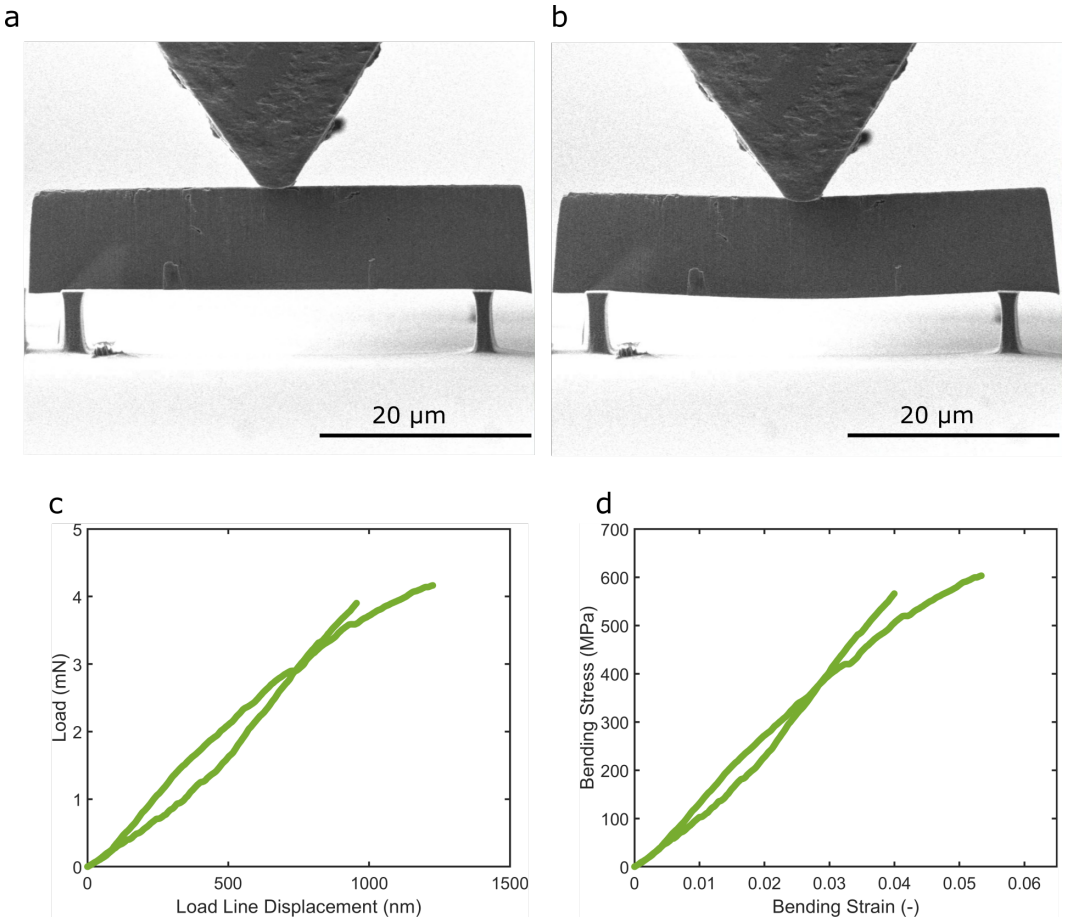

Figure 4.11: Bending Modulus and Strength of Lamellar Bone. a-b) The bending deformation response of unnotched bone specimen prepared in the similar manner with similar micro structural fibril orientation as the fracture specimen. c) Load vs displacement for two bending specimen. d) Stress vs strain of ending specimens with strength of 585 MPa and elastic modulus of 20.15 GPa

Fatigue Precracking Bone Specimens

In order to create a realistic or naturally sharp crack, half of the notched bone specimens are fatigue pre-cracked in accordance to the standards established for metals[76]. Specifically, the maximum load during fatiguing should not exceed a value P_m given by

$$P_m = \frac{1}{2}\frac{Bb_0^2}{S}\sigma_y \tag{4.12}$$

where b_0 is the uncracked ligament length given by $W - a_0$ and σ_y is the yield strength of an notched specimen. If we consider the nominal stress in a notched specimen as $\sigma = \frac{3}{2}\frac{PS}{Bb_0^2}$, and we plug in the criteria from Equation 4.12; the simple result is

states the nominal stress in the notched specimen during fatiguing cannot exceed 75 % of the yield stress of the material, i.e $\sigma_m \geq \sigma_y$. The beam bending experiments resulted in a bending strength of 585 MPa, giving us a maximum nominal stress of 439 MPa during fatiguing. Recall however that the specimen are free standing on the supports; fatiguing them with such boundary conditions would surely lead to losing the specimen. We thus fatigue precrack the specimen prior to freeing them from the sacrificial support during preparation as described in Section 4.4 and shown in 4.3. To determine an accurate maximum stress for fatiguing the specimens, we perform a bending experiment on a bone specimen that is still glued to the sacrificial support as shown in Figure 4.12a. The bone responds linear elastically to brittle failure and we calculate a nominal strength of 549 MPa. This is in agreement with the stress measured from the free standing specimen. We have a maximum nominal stress criteria of 400 MPa during fatiguing.

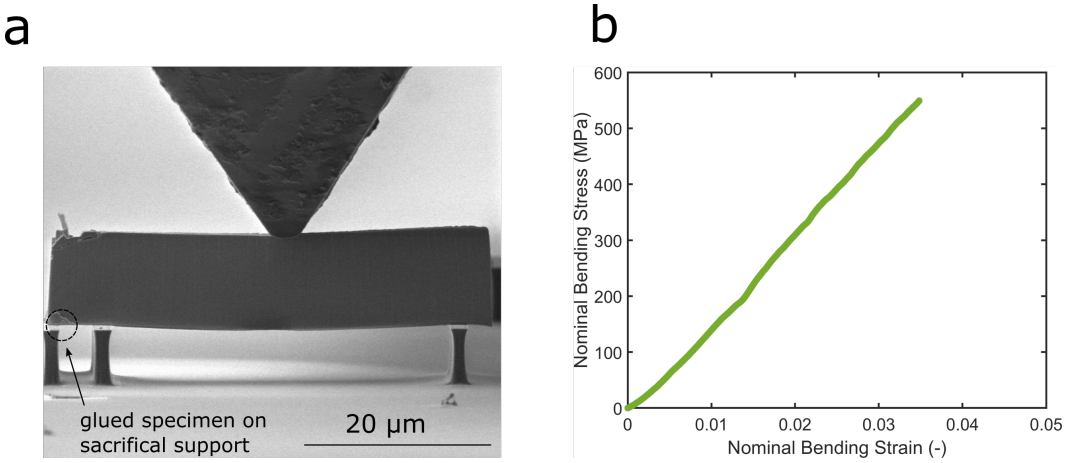

Figure 4.12: Bending Strength of Bone Specimen with Glued Boundary Condition

We fatigue precrack the specimens using the dynamical mechanical analysis capabilities of the nanoindenter. This is briefly described in Section 4.4 for applying a 2 nm oscillating load and tracking the stiffness (and thus compliance) of the specimen during a monotonic loading scheme. We use this functionality to apply a cyclic loading scheme at 50 Hz to notched specimens that are glued to the sacrificial support. Figure 4.13a shows the applied load scheme as a function of time; we monotonically load up to a static load which represents $\sim \frac{P_m}{2}$ and then we apply an oscillating load with an amplitude $\sim \frac{P_m}{2}$. We simultaneously track the dynamic stiffness of the specimen and set a condition that the cycling loading ends once the average stiffness drops by $\sim 1\%$. Figure 4.13b shows the same data as a function of cycles (time*50 Hz) starting at the oscillating scheme. In Figure 4.13c we show the

maximum nominal stress is within the calculated criteria. We reach the precracking condition on the order of $\sim 10^4$ cycles.

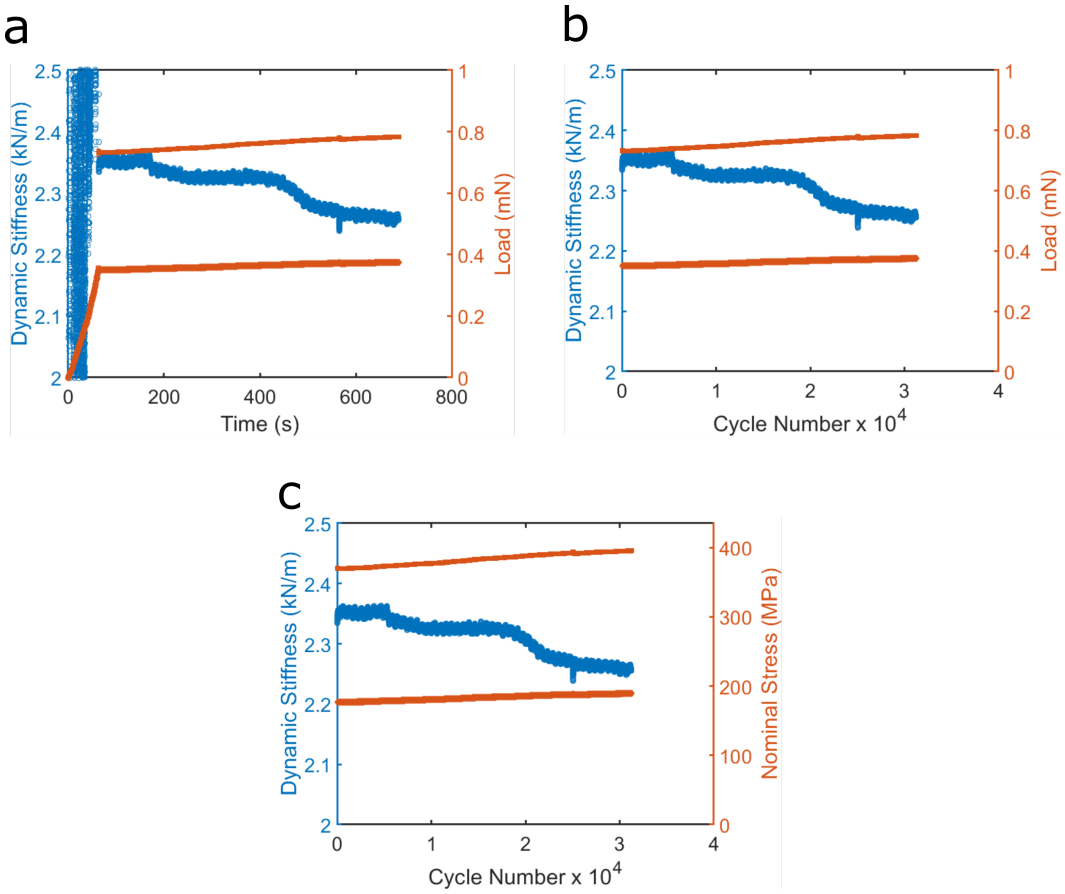

Figure 4.13: Fatigue Precracking Bone Specimens. a) shows the prescribed loading scheme up to some load with the upper and lower bound of the applied oscillatory load as a function of time. The dynamics stiffness is monitored and drops as a result of crack growth in the specimen. b) shows the same results as a function cycles and c) shows the nominal stress in the specimen as a function of cycle, remaining below 75% of the bending strength

Crack Initiation of Notched and Precracked Specimens

To quantify the crack initiation toughness of bone at the lamella length scale, we perform fracture experiments on both the as-notched and precracked from notched specimens. Figure 4.14 shows the conversion from load to the mode I stress intensity (K_I using Equation 4.7) as a function of the load line displacement for all specimens. Imperfect contact points in the experimental set up can lead to beam settling events that appear as deviations from linearity in the stress intensity data. These can be mistaken as crack initiation and make it difficult to determine the critical stress

intensity. As described in Section 4.4, we apply a dynamic oscillation of a 2 nm amplitude in order to track the instantaneous stiffness of specimen, thereby monitoring real crack initiation events. Figure 4.15 shows a examples of plots of the load to stress intensity conversion plotted with the simultaneously measured dynamic stiffness for a precracked 4.15a,b and a notched 4.15c,d specimen. The dynamic stiffness increases monotonically during the elastic load portion as the surfaces in contact during the settling into each other (i.e., contact area is increasing); The dynamic stiffness then begins to decrease; we find this decrease point correlates with the end of the linear elastic region in both the load and stress intensity vs load line displacement data. This is also evident from the synced videos that these events from crack initiation (Supplementary Videos 5 and 6). Figures 4.15b,d illustrates that the crack initiation toughness, or critical stress intensity K_{IC}, is taken as the stress intensity at which the dynamic stiffness begins to decrease.

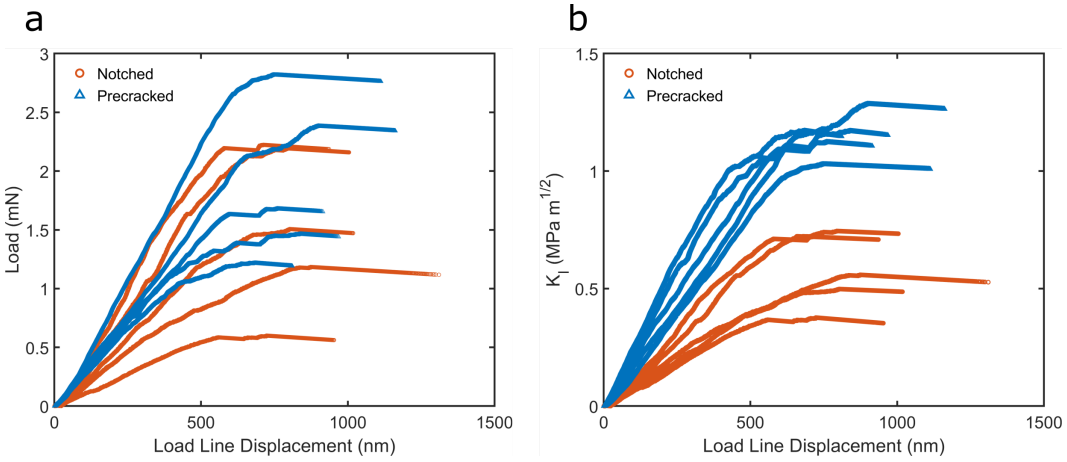

Figure 4.14: Loading response and K_{IC} of Bone Specimen. a) shows the load vs load line displacement data of the notched and precracked specimens and b) shows the mode I stress intensity calculated from the load data

The results indicate that the stress intensity in the notched specimen increases until the initiation of a crack at a K_IC of 0.54 ± 0.15 MPa $m^{1/2}$. Figures 4.16b-c show the corresponding bending response up to crack initiation, followed by stable crack growth (Figures 4.16c-d). The insets in Figures Figures 4.16b-d show magnified images of the notch tip, revealing the crack travels straight through the specimens without deflection. This is followed by catastrophic failure (Supplementary Video 5). Figures 4.17 shows the fracture behavior of the precracked bone specimens. The precrack surfaces first separate (4.17b-c, Supplemental Video 6) as the stress intensity increases linearly up to a crack initiation occurs at a K_{IC} of 1.08 +-.06 MPa

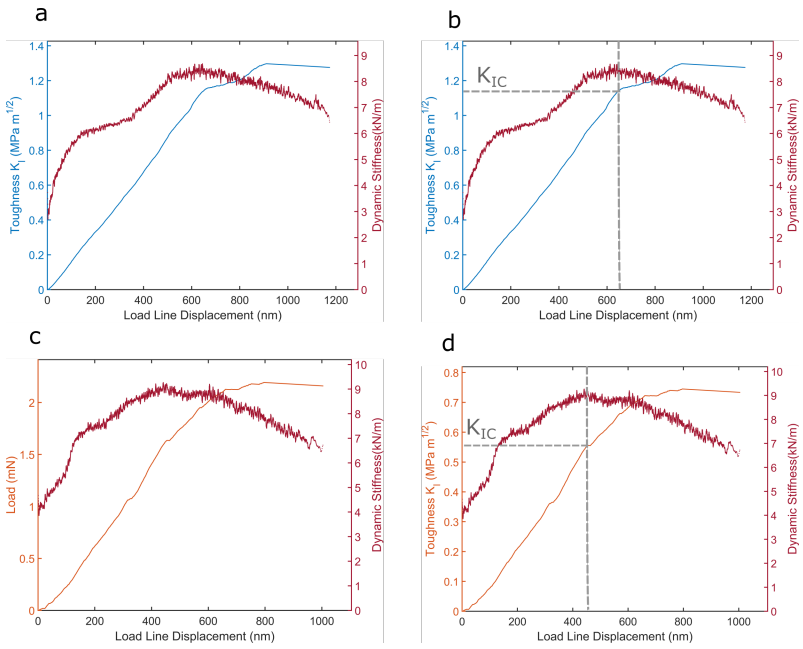

Figure 4.15: Measuring K_{IC} at end of elastic region denoted by end of increase on dynamic stiffness, i.e., crack initiation.

$m^{1/2}$. The crack continues to grow stably through the specimen until catastrophic failure (4.17c-d, Supplemental Video 6). Note that the stress intensities plotted in these figures are only valid up until crack initiation, as indicated by point "b" in both Figures 4.16 and 4.17.

A stochastically defined stress intensity for heterogeneous microstructure

We measure a 2-fold increase in the crack initiation toughness from notched to precracked bone specimens (0.54 to 1.08 MPa $m^{1/2}$). This result is counter to the failure criterion for brittle materials discussed at the end of Section 4.4, which generally states for a given failure material strength σ_0 the critical stress intensity scales with the crack tip radius. In the Creager and Paris formulation, the apparent toughness decreases linearly with crack tip radius $K_C \sim \sigma_0\sqrt{\pi a}\,(1 + \rho/a)$, where a is the crack length and ρ is the crack tip radius. Note that in certain geometries (i.e., penny shaped crack in 3D solid) this stress intensity can scale with the square root of the crack radius; in general, the relation of a lower apparent toughness for sharper crack tip is expected. This criterion assumes homogeneous material microstructure in front of the crack tip, and as a result, a deterministic failure strength, i.e., the materials fractures if stress locally reaches a σ_0. The heterogeneous microstructure of bone at the micrometer length scale, stemming from fibrils (Fig 4.10d) and

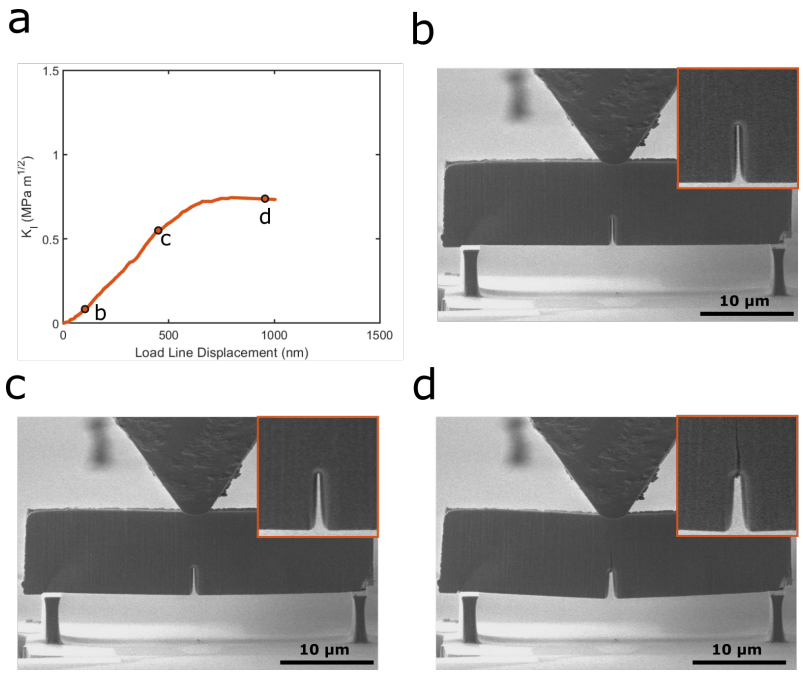

Figure 4.16: Fracture Response of Notched Specimen

porosity (as seen in Chapter 3) [70, 87], warrants a stochastic description of failure strength and toughness.

To investigate the relationship between toughness and crack radius for a material with a heterogeneous microstructure, we perform linear elastic Finite Element tension simulations on edge-cracked plates as shown in the schematics of Figure 4.18a,b . To simulate heterogeneity, the plates have varying Ritchie-Knott-Rice (RKR) characteristic microstructural length scales [88], r, and Weibull strength distributions with varying moduli, m.The RKR length scale was originally employed to describe a microstructural scale in which brittle cleavage fracture could occur at low temperatures in metals. As the tensile stresses in front of the crack tip drops off with the square root of the distance, the RKR length scale is that at which stress must still be greater than or equal to the tensile strength of the material for some brittle cleavage fracture to occur($\sim$ two grain sizes). The Weibull modulus describes the spread of the distribution of the material strength; a small m indicates a large spread or a more stochastic material[89]. In the present context, the material has a survival probability P_s given by

$$P_s = \exp\left[-\frac{1}{\pi r^2}\int\left(\frac{\sigma_{22}}{\sigma_0}\right)^m \mathrm{d}A\right] \tag{4.13}$$

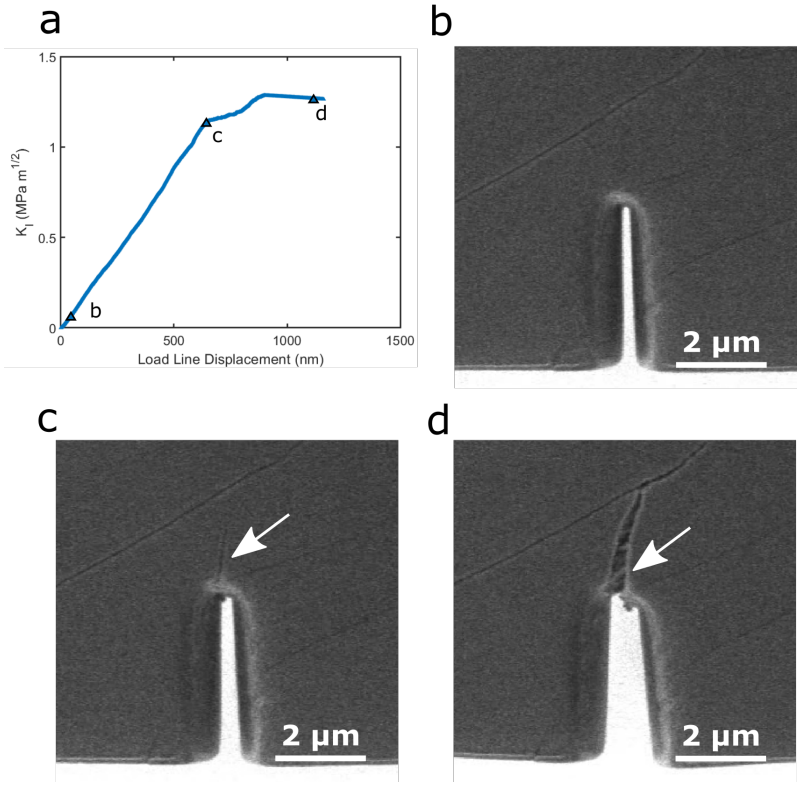

Figure 4.17: Fracture Response of Precracked Specimen

Here σ_{22} is the local tensile stress, σ_0 is the mean failure strength of the material and r is the RKR length scale. The critical stress intensity K_{IC} is calculated when the local stress gives $P_s = e^{-1}$, i.e., when the survival probability reaches to $\sim 63\%$.

Figure 4.18 shows the simulation results of the normalized toughness, $K_{IC}/(\sigma_0\sqrt{r})$, as a function of normalized crack radius (ρ/r). The results reveal that for $m > 4$, the toughness monotonically decreases with with crack tip radius, as expected in a deterministic brittle material. For $m \leq 4$ we observe a transition where a lower relative notch radius can give rise to a higher toughness. This uniquely occurs when the crack radius is comparable to the microstructural length scale ($\rho/r<1$).The schematics in Figure 4.18a,b illustrate the physical reasoning. In two plates with identical microstructural (or flaw) landscapes, a sharper crack will have higher stress concentrations, but the stress field of a blunter crack will extend further around the notch root. When the crack radius is roughly equal to the spacing between relevant microstructure, the stress field will interact more strongly with them than when the crack radius is much smaller than the microstructural features. Adopting the relevant microstructural scale in the bone specimens as the collagen fibril diameters (50-250

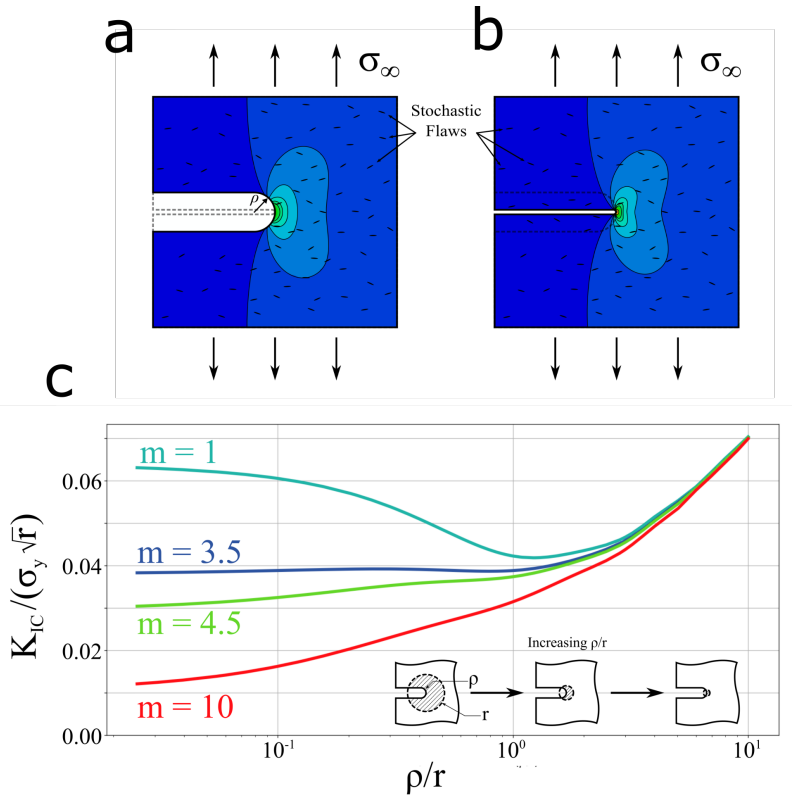

Figure 4.18: Loading response and K_{IC} of Bone Specimen.

nm) and the measured notch radii as $\sim$ 200nm, we calculate $\rho/r \leq$ in the present experiments. The reported Weibull modulus for bone ranges from 3.3-5.7 [90–92]. Estimating $m = 4.5$ as an average of this range, simulations suggests a heterogeneous material with relative notch radius in the $\rho/r \leq$ regime should have nearly constant (although still increasing in the deterministic sense) crack initiation toughness as a function of ρ/r, relative to those in the $\rho/r \geq 1$ (Fig 4.18c). These results suggest another mechanism is contributing to the higher toughness of precracked bone specimens.

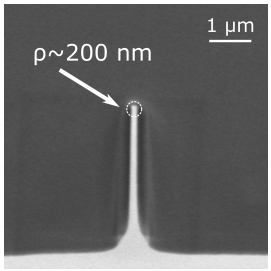

Figure 4.19: Radius of Notched Bone Specimen

Figures 4.17c,d and Supplemental Video 6 reveal mineralized collagen fibrils bridging the precrack surfaces of the specimens during linear elastic regime prior to crack initiation. In fiber-reinforced composites, this mechanism acts to shield the crack tip from remotely applied stress, effectively toughening the material [93]. The silicon micro-fracture results from Section 4.4 and FE simulations imply that when the relative crack tip radii are below unity ($\rho/a_0 \ll 1, \rho/r < 1$), the experiments on the bone specimen should result in a constant toughness; empirical measurements commonly have a constant toughness below some threshold radius in brittle materials [4, 94]. In the experiments presented here, we observe a 2 fold difference in K_{IC}, which can be attributed to the observed fibril bridging mechanism. This contributes an increase in toughness, ΔK_{IC}^{fibril}, of 0.54 MPa m$^{1/2}$. This mechanisms has been deemed inconsequential for toughening large cracks in bone ($a_o \sim 1\ mm$), in part because the fibril diameters are in the 50-250 nm range scale [95, 96]. However, fracture often initiation from microscale flaws. In bone these flaws are manifested as fibril-bridged microcracks that open by physiological cyclic loading or fatigue [97]. The results presented here demonstrate that mineralized collagen fibrils can prevent fracture initiation by doubling the critical driving force needed to open physiologically relevant flaws (fatigue precracks) in bone that are on the order of micrometers.

4.6 Crack Growth Resistance of Bone Lamellae

We quantified crack growth resistance by calculating the nonlinear elastic J-integral as a function of crack extension. Unlike the linear elastic stress intensity factor, the J-integral can account for the elastic and inelastic contributions to toughness during crack growth. We first describe the determination of crack extension and then the calculation and results of the crack growth resistance.

Calculating Crack Extension

The crack extension, Δa, is calculated from the dynamic stiffness measurements using an effective compliance calibration procedure [98]. The stiffness starting at crack extension - which is described as the maximum of the measured stiffness of the specimen - is inverted to acquire compliance of the specimen. The assumption here is that the minimum of the measured dynamic compliance represents the effective compliance, C_0, of the as fabricated specimen with initial crack length a_0. The relation between the load line compliance of a 3-, C, and the normalized crack length, a_i/W, of a 3-point bend fracture specimen specimen is given by

$$\frac{a_i}{W} = 0.997 - 3.58U - 1.51U^2 - 110U^3 + 1231^{U^4} - 4400U^5 \tag{4.14}$$

where

$$U = \frac{1}{(FC)^{\frac{1}{2}} + 1} \tag{4.15}$$

Here F is a calibration constant calculated by setting $\frac{a}{W} = a_0/W$ and $C = C_0$ [98, 99]. The crack extension at any instance is then calculated by solving for a_i/W for a measured C_i and subtracting from the initial crack length a_0. Figure 4.20 shows an example of the result of this procedure where Figure 4.20a shows the effective compliance from the stiffness (note the minimum compliance is take as the compliance prior to crack extension) and Figure 4.20b shows the calculated crack extension in correlation to the load response of the specimen.

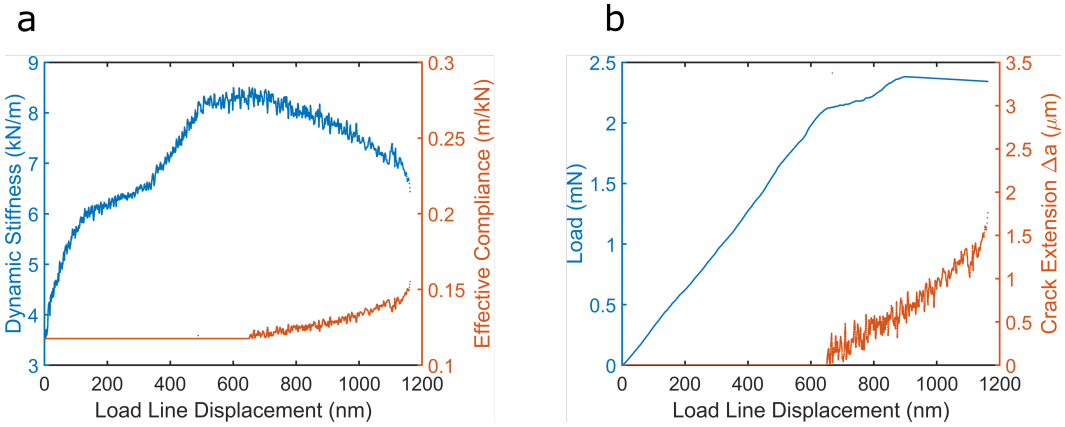

Figure 4.20: Radius of Notched Bone Specimen

Calculating J-Integral of 3-point bend specimen

In the present context, the J-integral is defined as

$$J_i = \frac{K_i^2\left(1-\nu^2\right)}{E} + J_{pl(i)} \tag{4.16}$$

Here the first term corresponds to the plane strain linear elastic equivalence between K and J where K_i is given by Equation 4.7. The second term is the plastic (inelastic) work contribution to the toughness. This is generally given by

$$J_{pl} = \frac{2A_p}{Bb} \tag{4.17}$$

where A_p is the plastic work and b is the length of the uncracked ligament (W-a). During crack growth the uncracked ligament is constantly increasing and an incremental definition of plastic work is given by the ASTM as follows:

$$J_{pl(i)} = \left[J_{pl(i-1)} + \left(\frac{\eta_{pl(i-1)}}{b_{i-1}}\right)\frac{\left(A_{pl(i)} - A_{pl(i-1)}\right)}{B}\right] * \left[1 - \frac{\gamma_{pl(i-1)}\left(a_i - a_{(i-1)}\right)}{b_{i-1}}\right] \tag{4.18}$$

Here η and γ are empirical constants equal to 1.9 and 0.9, respectively [76]. The $(a_i - a_{i-1})$ term is an incremental crack extension. The b_{i-1} term represents an uncracked ligament length such that b_i=$W - a_i$. An example of the incremental plastic area, A_{pl_i} , definition for this formulation in the present work is show in Figure 4.21. This incremental definition is applicable when steady crack growth is observed, as is with the bone specimens in the present work (Supplementary Videos 5 and 6).

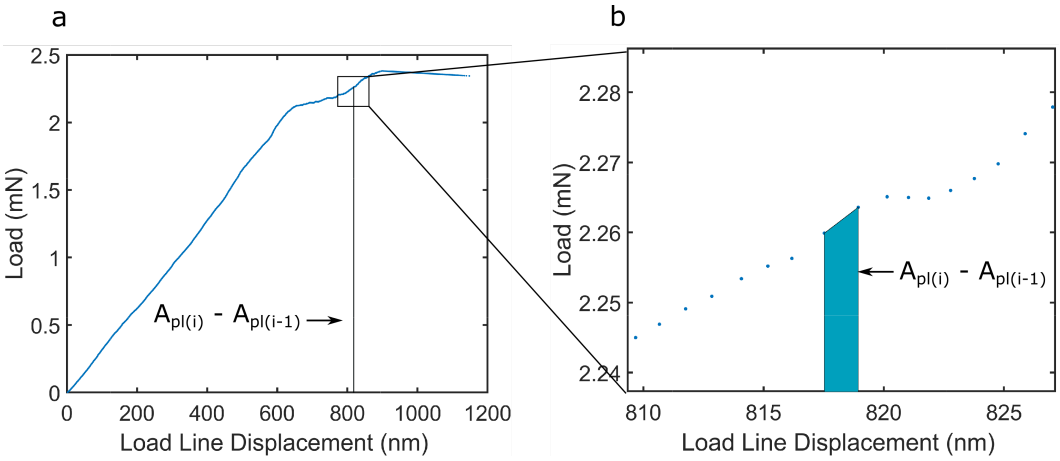

Figure 4.21: Incremental Plastic Area for J Integral calculation

Figure 4.22 shows the crack growth resistance of the precracked specimens up to ~ 1.5 um of stable crack growth. We measure an increase in toughness from an average initiation toughness of 52 to 120 J/m^2. In Figure 4.23 show images the fracture surfaces to identify the microstructural contributions to this fracture behavior. Figure 4.23b shows a fractured beam from a similar perspective as that of 4.23b; We observe fibrils with an average diameter of 51 ± 10 nm. Figure 4.23c shows a complementary fracture surface characterized by holes with an average diameter of 53 ± 10 nm.

This shows strong evidence of fibril bridging, and particularly, fibril pull-out during crack growth.

The macroscale toughness of bone is described primarily by its resistance to crack growth rather than by initiation. This macroscale toughening is mainly attributed to crack deflection and twist [8, 70]; at the microscopic lamellae length scales, the main toughening mechanisms have yet to be quantified. Post-mortem images of bone fracture surfaces in this work reveal a set of fibrils and holes on complementary surfaces, which suggests that fibril bridging contributes significantly to crack growth resistance at microscale crack extensions. In the following section, we discuss this toughness in the context of a bridging zone and propose a mechanistic relation between the fracture behavior and the length scale of the lamellae microstructure.

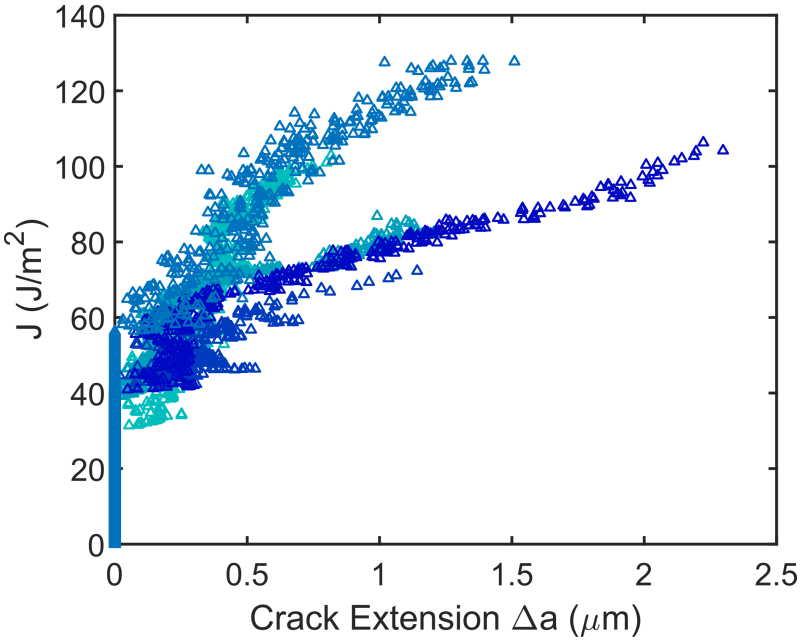

Figure 4.22: J Integral of Bone Lamellae

4.7 Bridging Zone and Characteristic Length

The fibril bridging mechanism observed in this work can be discussed using a cohesive zone model by drawing an analogy to the toughening behavior observed in fiber-reinforced engineering composites [6, 100]. Fiber-reinforced composites are often designed such that the matrix fractures prior to the fibers, resulting a "bridging zone" behind the crack tip in which fibers shield the tip from the remotely applied stress – similar to the mechanism observed within the bone specimens in the present work. The bridging zone is characterized by a bridging law, which

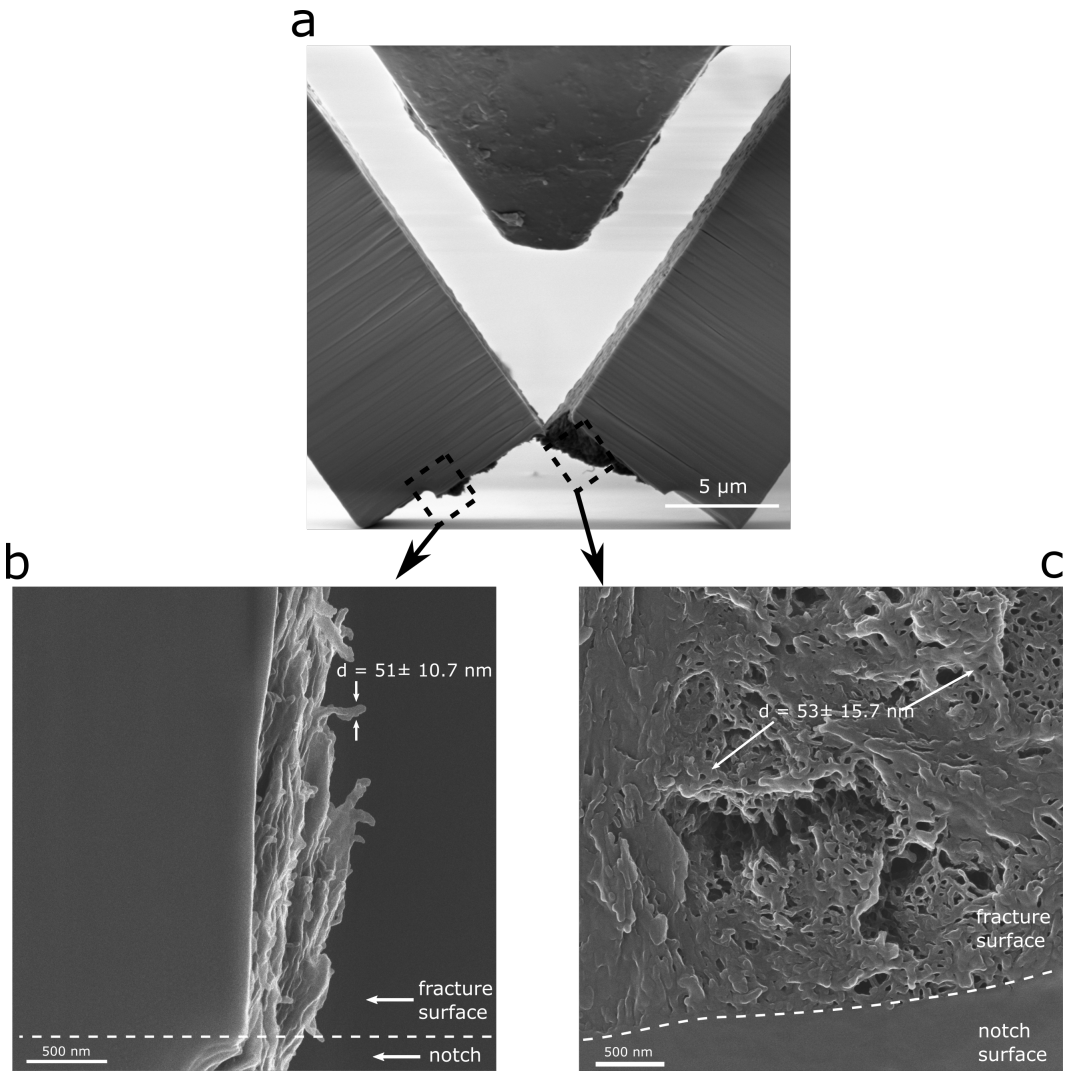

Figure 4.23: Evidence of Fibril Bridging in Bone Lamellae

describes the stress in the zone,σ, as a function of the separation of crack surfaces, denoted by δ [101]. Schematics of typical bridging law are shown in 4.24. The main characteristics of bridging laws are the max (or closure) stress σ_0, which represents the tensile strength of the material, and the maximum bridging zone opening δ_0. Specifically δ_0 is the opening at which the bridging elements in the crack wake can no longer apply closing tractions, i.e., cannot shield the crack tip from remotely applied stresses. The bridging law and the crack growth resistance are related by restating the J-integral in Equation 4.19.

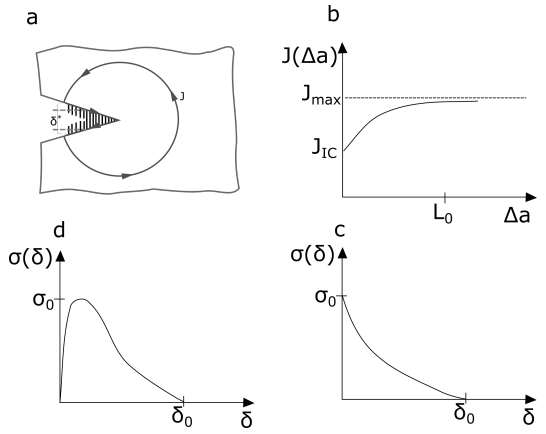

Figure 4.24: a) schematic of bridging zone. b) plateau toughness that arises after a charactertistic extension $l_{ch=L_0}$ c,d) hardening-softening bridging laws

$$\begin{aligned} J &= J_0 + \int^{\delta_0} \sigma(\delta)\mathrm{d}\delta \\ &= J_{IC} + \Delta J \end{aligned} \tag{4.19}$$

For brittle materials, the first term J_0 is equivalent to the linear elastic J_{IC}. The second term refers to the increase in toughness that occurs during crack growth. These are representative of the elastic and plastic components of the J-integral calculation as in ASTM formulation in 4.16. In this context, a characteristic length, l_{ch}, defines crack extension at which the material can no longer exhibits crack growth resistance. At a crack extension of l_ch , also described as the steady-state damage zone size, the material could fail catastrophically. Calculating the l_ch for the bone specimens in the present work could provide further insight into how fracture toughness arises from the bone hierarchy is at the lamellae length scale. In the context of bridging mechanisms the characteristic length is given by

$$l_{ch} = 0.366\frac{E\delta}{\sigma_0} \tag{4.20}$$

where E is the elastic modulus of the composite [101]. To calculate the l_{ch} of the bone specimens, it is necessary to first determine the bridging law $\sigma(\delta)$.

The specific functional form of $\sigma(\delta)$ is experimentally difficult to measure [6, 101, 102]. Often the tensile stress vs strain behavior of the 1) individual bridging (reinforcement) components or 2) notched composite is related to the bridging law but this is approach faces certain issues. A common issue is the appearance

of multiple cracks within the tension specimen which result in rotations of the specimen (due to bending moments). This causes mixed mode fracture and difficulty identifying crack tip openings[103]. An alternative approach for determining the bridging law is a J-integral approached proposed by [102]. This simply takes advantage of rewriting $\sigma(\delta)$ as the derivative of the J-integral. In the present work, taking the derivative of the experimentally calculated J as a function of δ can allow for the determination of an empirical bridging law. To determine $J(\delta)$ from the calculated $J(\Delta a)$, we employ *in situ* SEM videos of the experiments to determine the bridging zone opening δ. That process is breifly described before discussing the bridging law results.

$$\sigma(\delta) = \frac{\partial J(\delta)}{\partial \delta} \tag{4.21}$$

Measuring crack openings

The *in situ* experiments provide video frames (correlated to the measured load, displacement, and siffness data) that enable the visual measurement of the crack mouth opening displacement (CMOD or simply d hereafter). We wrote a custom Matlab script to track the crack mouth opening in the videos; in its simplest from, the script identifies the crack mouth by thresholding the video frames in a region of interest that includes the notch, similar to the region shown in Figure 4.25a. The result of this is shown in Supplementary Video 7, where the red outline shows successful identification of the initial notch geometry. In each frame, the measurement for d is made at 20% of the height of the identified notch height (denoted at n_0 for the initial configuration and n_i in Figure 4.25). This is done in order to have a consistent measurement of d devoid of any irregularities at the bottom of the identified notch stemming from contrast artifacts.

The bridging zone separation δ is taken as the crack opening at the initial crack tip; for the initial configuration $\delta = 0$ as shown in Fig 4.25a,c. This separation is then geometrically calculated; Figure 4.25d shows that as the crack grows by Δa_i and the crack mouth opens to a new value d_i, we can create two right triangles with bases $d_i/2$ and $\delta_i/2$. We note these are similar right triangles that share an angle θ_i so the dimensions are proportional. Thus we have

$$\delta_i = \left(\frac{d_i}{a_i - \frac{n_i}{5}} \right) \Delta a_i \tag{4.22}$$

This approximation assumes the crack tip openings vary linearly with crack extension; because we do not observe crack tip blunting and the bone is generally linear elastic and brittle under bending as shown in Section 4.5, this should be a reasonable assumption. As the δ_i are determined from d_i, they are also correlated to the calculated J-integral, and thus we have experimentally determined $J(\delta)$ data as shown in Figure 4.26 from which the bridging law can be calculated.

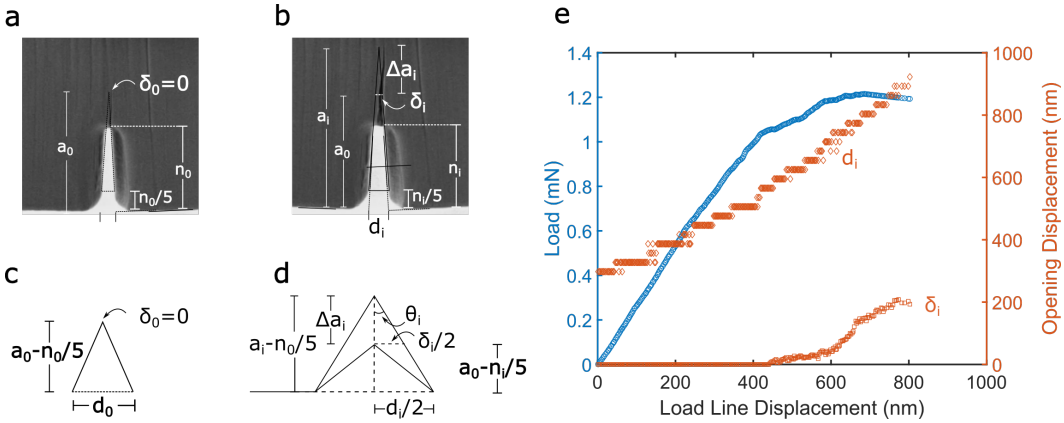

Figure 4.25: Estimating bridging crack opening through measurement of crack mouth opening and geometric argument.

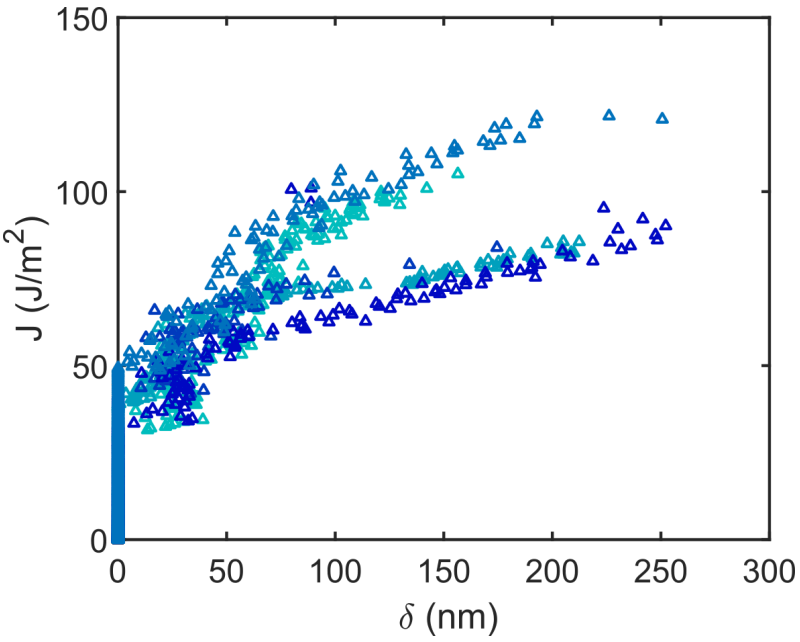

Figure 4.26: Toughness vs Bridging Zone Opening

To calculate the bridging law from the $J(\delta)$ data using Equation 4.21, the data is fit to a functional derived from Li et al [75, 104]. Those authors describe

a quadratic relation between the stress and crack opening (Eq 4.23) after crack initiation that empirically captures the pullout stress-separation behavior of various fiber-reinforced cementitious composites. We integrate this relation with respect to δ and get a cubic function for $J(\delta)$ as shown in Equation 4.24. Here σ_0) and δ_0 are the fitting parameters.

$$\sigma = \sigma_0 \left(1 - \frac{\delta}{\delta_0}\right)^2 \tag{4.23}$$

$$J(\delta) = \sigma_0 \left(\delta - \frac{\delta^2}{\delta_0} + \frac{\delta^3}{\delta_0}\right) \tag{4.24}$$

The fitting results of the experimentally determined increase in toughness ΔJ (the rising potion of $J(\delta)$) to Equation 4.24 are shown in 4.27a for two representative specimens showing a relatively good fits at small bridging zone openings, i.e., at $\delta > 100nm$ for one of the specimens the data starts to deviate from the cubic relation. We calculate an average strength σ_0 of 561 ± 75 MPa and a critical bridging zone of δ_0 427 ± 310 nm. The large spread in the δ_0 fit results is due to the accuracy of the cubic fit a larger δ values. Figure 4.27c shows the average experimental bridging law determined from these parameters. The dashed lines represent error bounds calculated from one standard deviation of the fitted σ_0 and δ_0. Due to the quadratic nature of the employed bridging law, the results exclusively capture a stress softening behavior. Mechanistically this was described by Aveston, Cooper, and Kelly as the relative slipping of unbonded fibers against the interfacial shear stress, i.e., fiber pullout after peak stress [5].

Physically in many bridging mechanisms, the stress increases sharply with small separations, indicating the activation of the debonding process[5]. We explore an exponential relation between J and δ employed to capture the initial Hookean stress-seperation behavior at small values of δ in more general cohesive zones models (see Fig 4.24c) [103]. A simplified form is derived from [102] as

$$J(\delta) = J_m - \left(J_m + J_m \frac{\delta}{\delta_{peak}}\right) \exp\left(-\frac{\delta}{\delta_{peak}}\right) \tag{4.25}$$

Here J_m is the plateau toughness of the bridging mechanism as shown in Figure 4.24b, and δ_{peak} is the peak stress. We calculate $J_m = 55.1 \pm 21.7$ and $\delta_{peak} = 31.85 \pm 10.67$. The results of the fit are show in Figure 4.27b for the same specimens;

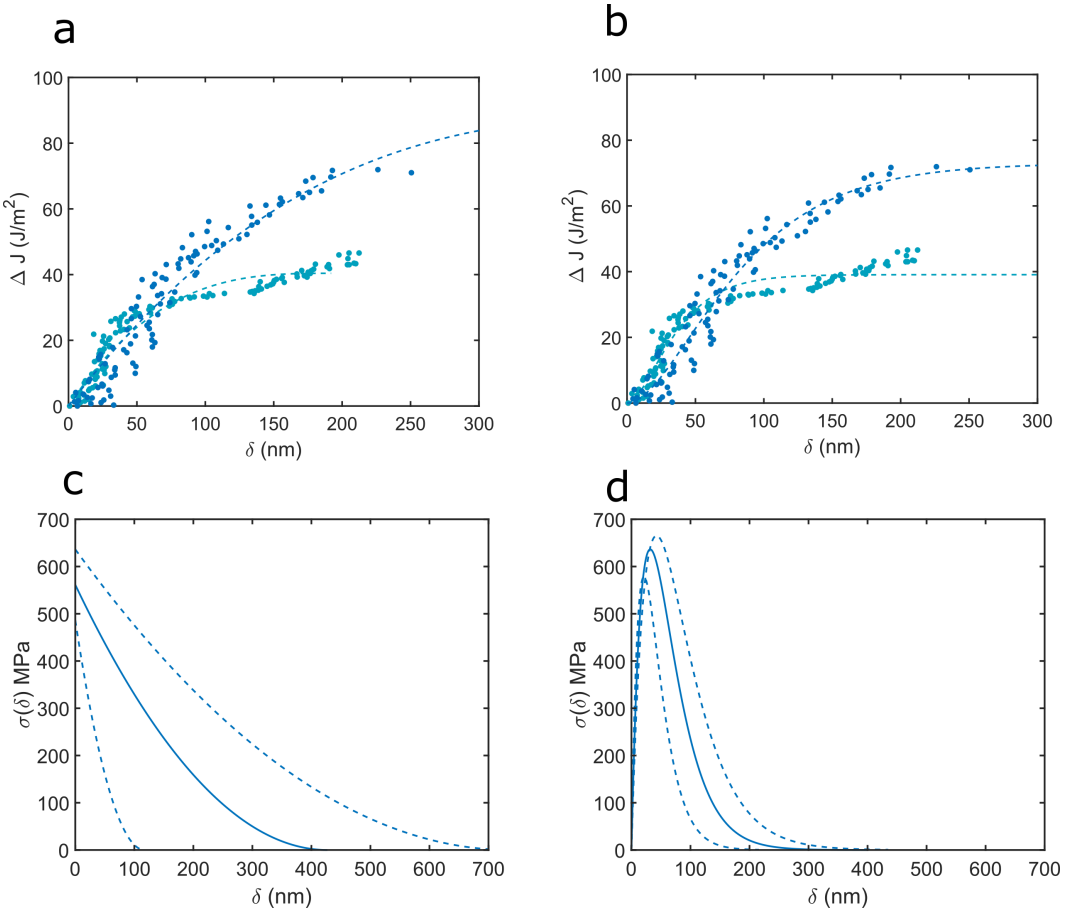

Figure 4.27: Toughness And Bridging Law vs Crack Opening for cubic model a,c) and exponential model b,d).

the exponential enforces a plateau in the $J(\delta)$ near the maximum of the measured toughness. The resulting bridging laws are shown in Figure 4.27d where we calculate a tensile strength $\sigma_0 = 636 \pm 44$ MPa. Within error, this is in agreement with the σ_0 calculated using the cubic fit as well as the bending experiments discussed in Section 4.5. This it has an aphysical property; due to the exponential functional decay, the σ_0 approaches but does not equal 0, thus we do no have a unique δ_0. However the steady state damage zone size l_{ch} can also be given by $\frac{EJ_c}{\sigma_o^2}$ [101]. Using this we now discuss results of l_{ch} from the cubic as well as exponential forms of $J(\delta)$.

We calculate and average steady state damage zone size , l_{ch}, of 5.59 μm (ranging from 1.7 to 8.5 μm) and 2.7 μm (ranging from 2 to 3.5 μm) for the cubic and exponential model fits respectively. Although the fitted σ_0 results in both fits are in great agreement, the wide range of the fitted results for δ_0 in the cubic model produces a much larger uncertainty l_{ch}. The calculated l_{ch} from the exponential

model has smaller span and lies within the bounds of the cubic model results. We take the average of the results $l_{ch} \sim 4\mu m$ as an effective steady state damage zone size. We can consider this result in relation to the relevant length scales of bone in the presently studied level of hierarchy.

As the lamellae of bone are 3-7 μm thick, the calculated l_{ch} suggests a mechanism for toughening related to the intrinsic dimensions of this level of the bone hierarchy. In a homogeneous brittle material with similar l_{ch}, as a crack grows up to ~4 μm, the driving force to continue crack growth should plateau and catastrophic failure would be imminent. In bone this crack would interact with the interfaces between the lamellae. This interface has been described as a disordered motif of bone mineralized collagen fibril composite [87]. At this interface the cracks would either deflect or require re initiation in the following lamella; the applied driving force would have to increase in order to continue crack growth, i.e., the material is toughened. This proposes a possible link between the intrinsic dimensions of the bone lamellae and the steady state damage zone size supported by fibril bridging mechanism observed in the experiments in the present work. Performing these experiments on larger specimens (~ 2x) would help confirm this.

4.8 Toughness of Bone Through Hierarchy

It is generally accepted that toughening mechanisms in hierarchical natural materials operate at different length scales but quantitative description of how and why this leads to a desired rising R-curve in bone had not been determined [105]. Figure 4.28 shows a juxtaposition of our experimental data of crack growth resistance in the 1 μm crack extension regime and that at 500 μm of crack extension from [8]. The effective toughness K_J is back calculated from the J integral as $K_J = (JE')^{1/2}$. The figure shows that at large crack lengths, crack deflection/twist at stiff interfaces of osteons, contribute most substantially to the R-curve of bone. By extrapolating the large crack R-curve down to small crack extensions relevant to this work using a standard power-law fit employed or metals (Appendix C), it significantly underestimates the toughness of micro-scale bone. We observe that by isolating the fibril microstructure in micron-sized beams, its toughness at ~ 1 μm of crack extension is ~ 30 times higher than that predicted from macroscale fracture experiments. Extrapolating the R-curve from present study shows an intersection with the macroscale experiments a crack extensions of ~70 μm. This is the same length scale as spacing between cement lines and is consistent with the ~100 μm of crack extension necessary to measuring the toughening effects of crack deflection in macroscopic fracture

experiments. These results enable a quantitative description of how the R-curve in bone changes as a function of crack growth in response to the salient levels of hierarchy.

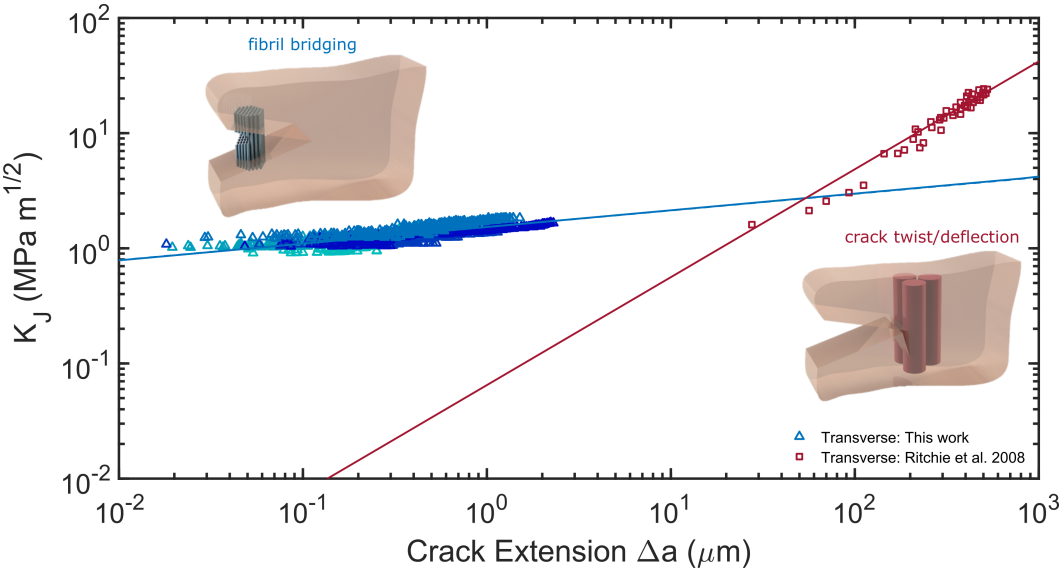

Figure 4.28: Scaling of Toughness in Bone Hierarchy

Revisiting the "R-Curve"

From a fundamental perspective, the beginning of the R-curve is often described as a flat or microstructure-independent component of the crack growth resistance[3]. A schematic of this type of R-curve is shown in 4.29. Brian Lawn describes this flat portion as the crack extension equal to the characteristic spacing of relevant microstructural components in a material that exhibits a rising R-curve behavior. In the context of a macroscale experiments, it is possible to measure an R-curve that is dominated by certain mechanisms, as shown in 4.28. If little is known about the microstructure of the material, the Lawn interpretation would lead us to believe the characteristic microstructural length scale is on the order of the crack extension at which the R-curve (measured from macroscale experiments) begins to rise. However with the development of the microscale methodology developed here, we uncover a rising or toughening component of the previously "flat" portion of the R-curve of a material. Although it does not contribute to the overall final toughness of the material prior to complete failure, it is fundamentally instrumental to giving rise to other mechanisms that dominate large length scales.

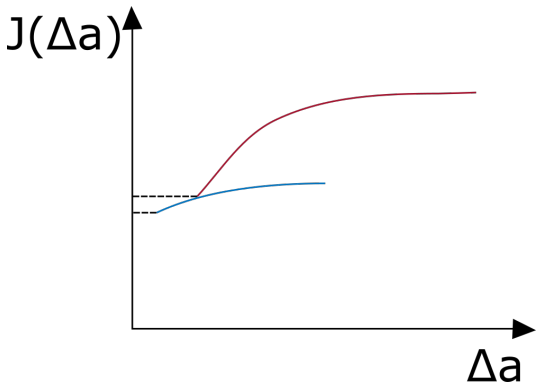

Figure 4.29: Revisiting the Curve. Red curve (and the corresponding black dashed segment) is representative of how we classically view crack growth resistance. With the ability to measure toughness at microscopic crack extensions we show that there is a fundamentally increase portion of the R-curve originating from microstructure that is not resolved in classical, large scale fracture experiments. In the context of bone, this microstructure is the 50-200nm mineralized collagen fibril.

Summary/Outlook

Studying and mimicking natural materials to achieve similar damage tolerance in engineered materials has gained substantial traction over the past decade [9, 10, 106]. The main biomimetic pursuits have been focused on designing and incorporating multi-scale material hierarchy, starting from nanoscale features to produce macroscale materials [11, 12, 107]. These biomimetic studies have focused on overcoming hierarchical manufacturing challenges; the questions of why nanoscale constituents and how to quantify the contributions of the underlying mechanisms at those length scales remain experimentally challenging to answer. The microscale fracture methodology, quantified nano-fibril toughening, and description of length scale dependent toughening in bone provide a new route to studying hierarchical materials as well as insight into designing damage tolerant bioinspired materials.

Chapter 5

SUMMARY AND OUTLOOK

This thesis has focused on understanding the relationship between the structure of bone and its mechanical behavior at length scales that specifically probe the response of the lamellae and the mineralized collagen fibrils. In bone, this range is $\sim 7\mu m$ and smaller. We started by first reporting a microstructure that had not yet be reported within the trabecular bone architecture in the literature. This was the result of the ability to probe the hierarchical structure with high spacial accuracy at length scales of the underlying microscopes. It also allowed us to establish the simple hierarchical picture of bone for the remainder of the work in the thesis.

Following this we borrowed from techniques used to characterize the strength and deformation of small scale metals to site specifically probe the strength and deformation of an ordered and disordered phase of bone via micro and nano-pillar compression experiments. We showed that as we decreased the size of the pillars towards the size of the mineralized collagen fibrils, a transition from ductile to brittle deformation. We also observe a corresponding increase in measured strength that we attribute to the decreased effect in stress concentrations from the reduced number of critical flaws at smaller sample dimensions. This falls in line with a smaller is stronger paradigm in the hierarchy of bone; as we reduce interfaces and heterogeneities that can concentrate stress or strain by reducing specimen dimensions (i.e., reducing complexity of the structure being mechanically loaded) the apparent strength increases.

Following this we explored the resistance to fracture in bone. Unlike probing the uniaxial deformation at small length scales, we developed a 3-point bending experimental approach for measure toughness in micron sized specimens. This build upon the ability to site specifically isolate micro structure in bone using a transmission electron microscopy sample preparation technique. We first show that the microscale fracture method is valid in a linear elastic frame work using silicon a reference material. We then show the effects of fibril bridging in the crack initiation and crack growth resistance of bone from realistically grown precracks. When placed in the context of engineering materials, we can consider bone to be be designed like a fiber composite at the micrometer length scale, which allows toughening small

cracks before they grow and encounter other obstacles at larger length scales (i.e., crack deflection and twist at osteons). This work is able to quantify this behavior and put it in a larger context, allowing for a quantitative comparison of how toughness arises from different levels of the bone hierarchy.

We were also able to experimentally determine the bridging law of a material. At these such small scales this has paves a route for modeling and predicting of fracture behavior of multiscale materials. Cohesive elements can be developed using the defining characteristics of a bridging law (or more generally a cohesive law). These elements can describe the fracture behavior of a hierarchical material in multi-scale simulations, especially those that incorporate homogenization schemes. This is a promising are to explore for modeling the mechanics of bone.

We hope the work presented in this thesis establishes an approach for probing the underlying structure-function relationship of this natural materials. The equally important question of how to create materials that outperform those found in nature in the context of weight and damage tolerance remains a significant challenge. This is a truly interesting direction for future work.

BIBLIOGRAPHY

[1] Ritchie, R. O. In pursuit of damage tolerance in engineering and biological materials. *MRS Bulletin* **39**, 880–890 (2014). URL http://www.journals.cambridge.org/abstract_S0883769414001973.

[2] Griffith, A. A. The Phenomena of Rupture and Flow in Solids (1921).

[3] Lawn, B. R. & Wilshaw, T. R. *Fracture of brittle solids* (Cambridge University Press, 1993).

[4] Sakai, M. & Bradt, R. C. Fracture toughness testing of brittle materials. *International Materials Reviews* **38**, 53–78 (1993). URL http://www.tandfonline.com/doi/full/10.1179/imr.1993.38.2.53.

[5] Aveston, J. & Kelly, A. Theory of multiple fracture of fibrous composites. *Journal of Materials Science* **8**, 352–362 (1973).

[6] Evans, A. G. & McMeeking, R. M. On the toughening of ceramics by strong reinforcements. *Acta Metallurgica* **34**, 2435–2441 (1986).

[7] Libonati, F., Buehler, M. J., Libonati, B. F. & Buehler, M. J. Advanced Structural Materials by Bioinspiration. *Advanced Engineering Materials* **19**, 1–19 (2017).

[8] Koester, K. J., Ager, J. W. & Ritchie, R. O. The true toughness of human cortical bone measured with realistically short cracks. *Nature materials* **7**, 672–677 (2008). URL http://www.ncbi.nlm.nih.gov/pubmed/18587403.

[9] Tanay, A. *et al.* Tough, Bio-Inspired Hybrid Materials 1516–1520 (2008).

[10] Gao, H., Ji, B., Jager, I. L., Arzt, E. & Fratzl, P. Materials become insensitive to flaws at nanoscale: lessons from nature. *Proceedings of the National Academy of Sciences of the United States of America* **100**, 5597–5600 (2003).

[11] Wegst, U. G. K. *et al.* Bioinspired structural materials. *Nature Materials* **14**, 23–36 (2014). URL http://www.sciencemag.org/content/319/5866/1053.shorthttp://www.nature.com/doifinder/10.1038/nmat4089http://www.sciencemag.org/content/319/5866/1053.short%5Cnhttp://www.nature.com/doifinder/10.1038/nmat4089%5Cnhttp://www.ncbi.nlm.nih.gov/pubmed/25344782.

[12] Bouville, F. *et al.* Strong, tough and stiff bioinspired ceramics from brittle constituents. *Nature Materials* **13**, 508–514 (2014). URL http://www.nature.com/articles/nmat3915.

[13] Le Ferrand, H., Bouville, F., Niebel, T. P. & Studart, A. R. Magnetically assisted slip casting of bioinspired heterogeneous composites. *Nature Materials* **14** (2015). URL http://www.nature.com/doifinder/10.1038/nmat4419.

[14] Chen, P. Y., McKittrick, J. & Meyers, M. A. Biological materials: Functional adaptations and bioinspired designs. *Progress in Materials Science* **57**, 1492–1704 (2012). URL http://dx.doi.org/10.1016/j.pmatsci.2012.03.001.

[15] Ortiz, C. & Boyce, M. C. Materials science. Bioinspired structural materials. *Science (New York, N.Y.)* **319**, 1053–1054 (2008).

[16] Currey, J. D. Hierarchies in Biomineral Structures. *Science* **309**, 253–254 (2005). URL http://www.sciencemag.org/cgi/doi/10.1126/science.1113954.

[17] Meyers, M. A., McKittrick, J. & Chen, P.-Y. Y. Structural Biological Materials: Critical Mechanics-Materials Connections. *Science* **339**, 773–779 (2013). URL http://www.sciencemag.org/cgi/doi/10.1126/science.1220854.

[18] Pasteris, J. D. *et al.* Lack of OH in nanocrystalline apatite as a function of degree of atomic order: Implications for bone and biomaterials. *Biomaterials* **25**, 229–238 (2004).

[19] Fantner, G. E. *et al.* Sacrificial bonds and hidden length dissipate energy as mineralized fibrils separate during bone fracture. *Nature materials* **4**, 612–616 (2005). URL http://www.ncbi.nlm.nih.gov/pubmed/16025123.

[20] Weiner, S., Traub, W. & Wagner, H. D. Lamellar bone: structure-function relations. *Journal of structural biology* **126**, 241–255 (1999).

[21] Gibson, L. J. Biomechanics of cellular solids. *Journal of Biomechanics* **38**, 377–399 (2005). URL http://www.ncbi.nlm.nih.gov/pubmed/15652536http://www.sciencedirect.com/science/article/pii/S0021929004004919.

[22] Gal, A., Weiner, S. & Addadi, L. A perspective on underlying crystal growth mechanisms in biomineralization: solution mediated growth versus nanosphere particle accretion. *CrystEngComm* **17**, 2606–2615 (2015). URL http://xlink.rsc.org/?DOI=C4CE01474J.

[23] Mahamid, J., Sharir, A., Addadi, L. & Weiner, S. Amorphous calcium phosphate is a major component of the forming fin bones of zebrafish: Indications for an amorphous precursor phase. *Proceedings of the National Academy of Sciences of the United States of America* **105**, 12748–12753 (2008).

[24] Mahamid, J. *et al.* Mapping amorphous calcium phosphate transformation into crystalline mineral from the cell to the bone in zebrafish fin rays. *Proceedings of the National Academy of Sciences of the United States of America* **107**, 6316–6321 (2010). URL http://www.pubmedcentral.nih.gov/articlerender.fcgi?artid=2851957&tool=pmcentrez&rendertype=abstract.

[25] Wu, Y. *et al.* Nuclear magnetic resonance spin-spin relaxation of the crystals of bone, dental enamel, and synthetic hydroxyapatites. *Journal of bone and mineral research : the official journal of the American Society for Bone and Mineral Research* **17**, 472–480 (2002).

[26] Wang, Y. *et al.* Water-mediated structuring of bone apatite. *Nature materials* **12**, 1144–53 (2013). URL http://www.ncbi.nlm.nih.gov/pubmed/24193662.

[27] Boskey, a. & Posner, a. Formation of Hydroxyapatite at Low Supersaturation. *The Jornal of Physical Cemistry* **80**, 40–45 (1976).

[28] Chen, P. Y., Toroian, D., Price, P. a. & McKittrick, J. Minerals form a continuum phase in mature cancellous bone. *Calcified Tissue International* **88**, 351–361 (2011). URL http://www.pubmedcentral.nih.gov/articlerender.fcgi?artid=3075393&tool=pmcentrez&rendertype=abstract.

[29] Hassenkam, T. *et al.* High-resolution AFM imaging of intact and fractured trabecular bone. *Bone* **35**, 4–10 (2004). URL http://www.ncbi.nlm.nih.gov/pubmed/15207735.

[30] Reznikov, N., Almany-Magal, R., Shahar, R. & Weiner, S. Three-dimensional imaging of collagen fibril organization in rat circumferential lamellar bone using a dual beam electron microscope reveals ordered and disordered sublamellar structures. *Bone* **52**, 676–683 (2013). URL http://www.ncbi.nlm.nih.gov/pubmed/23153959.

[31] Reznikov, N., Shahar, R. & Weiner, S. Three-dimensional structure of human lamellar bone: The presence of two different materials and new insights into the hierarchical organization. *Bone* **59**, 93–104 (2014). URL http://www.ncbi.nlm.nih.gov/pubmed/24211799.

[32] Reznikov, N., Chase, H., Brumfeld, V., Shahar, R. & Weiner, S. The 3D structure of the collagen fibril network in human trabecular bone: Relation to trabecular organization. *Bone* **71**, 189–195 (2015). URL http://linkinghub.elsevier.com/retrieve/pii/S8756328214003901.

[33] Nassif, N. *et al.* In vivo inspired conditions to synthesize biomimetic hydroxyapatite. *Chemistry of Materials* **22**, 3653–3663 (2010).

[34] Giraud Guille, M. M. Liquid crystallinity in condensed type I collagen solutions. A clue to the packing of collagen in extracellular matrices. *Journal of molecular biology* **224**, 861–73 (1992). URL http://www.ncbi.nlm.nih.gov/pubmed/1569562.

[35] Wang, Y. *et al.* The predominant role of collagen in the nucleation, growth, structure and orientation of bone apatite. *Nature Materials* **11**, 724–733 (2012). URL http://www.ncbi.nlm.nih.gov/pubmed/22751179.

[36] Nudelman, F. *et al.* The role of collagen in bone apatite formation in the presence of hydroxyapatite nucleation inhibitors. *Nature materials* **9**, 1004–1009 (2010). URL http://dx.doi.org/10.1038/nmat2875.

[37] Nudelman, F., Lausch, A. J., Sommerdijk, N. A. J. M. & Sone, E. D. In vitro models of collagen biomineralization. *Journal of Structural Biology* **183**, 258–269 (2013). URL http://dx.doi.org/10.1016/j.jsb.2013.04.003.

[38] Alexander, B. *et al.* The nanometre-scale physiology of bone: steric modelling and scanning transmission electron microscopy of collagen-mineral structure. *Journal of The Royal Society Interface* **9**, 1774–1786 (2012).

[39] Currey, J. D. What determines the bending strength of compact bone? *The Journal of experimental biology* **202**, 2495–2503 (1999).

[40] Zimmermann, E. a. & Ritchie, R. O. Bone as a Structural Material. *Advanced Healthcare Materials* n/a–n/a (2015). URL http://doi.wiley.com/10.1002/adhm.201500070.

[41] Jäger, I. & Fratzl, P. Mineralized collagen fibrils: a mechanical model with a staggered arrangement of mineral particles. *Biophysical journal* **79**, 1737–1746 (2000). URL http://www.sciencedirect.com/science/article/pii/S0006349500764265.

[42] Greer, J. R., Oliver, W. C. & Nix, W. D. Size dependence of mechanical properties of gold at the micron scale in the absence of strain gradients. *Acta Materialia* **53**, 1821–1830 (2005). URL http://linkinghub.elsevier.com/retrieve/pii/S1359645404007670http://www.sciencedirect.com/science/article/pii/S1359645404007670.

[43] Greer, J. R. & De Hosson, J. T. M. Plasticity in small-sized metallic systems: Intrinsic versus extrinsic size effect. *Progress in Materials Science* **56**, 654–724 (2011). URL http://linkinghub.elsevier.com/retrieve/pii/S0079642511000065http://www.sciencedirect.com/science/article/pii/S0079642511000065.

[44] Johnson, K. L. *Contact Mechanics* (Cambridge University Press, New York City, 1994).

[45] Oliver, W. & Pharr, G. Measurement of hardness and elastic modulus by instrumented indentation: Advances in understanding and refinements to methodology. *Journal of Materials Research* **19**, 3–20 (2004).

[46] Gupta, H. S. *et al.* Nanoscale deformation mechanisms in bone. *Nano Letters* **5**, 2108–2111 (2005).

[47] Gupta, H. S. *et al.* Cooperative deformation of mineral and collagen in bone at the nanoscale. *Proceedings of the National Academy of Sciences of the United States of America* **103**, 17741–17746 (2006). URL http://www.pnas.org/cgi/doi/10.1073/pnas.0604237103http://www.pubmedcentral.nih.gov/articlerender.fcgi?artid=1635545&tool=pmcentrez&rendertype=abstract.

[48] Gupta, H. S. *et al.* Fibrillar level fracture in bone beyond the yield point. *International Journal of Fracture* **139**, 425–436 (2006).

[49] Schwiedrzik, J. *et al.* In situ micropillar compression reveals superior strength and ductility but an absence of damage in lamellar bone. *Nature materials* **13**, 1–8 (2014). URL http://www.ncbi.nlm.nih.gov/pubmed/24907926.

[50] Faingold, a. *et al.* The effect of hydration on mechanical anisotropy, topography and fibril organization of the osteonal lamellae. *Journal of Biomechanics* **47**, 367–372 (2014). URL http://www.ncbi.nlm.nih.gov/pubmed/24332267.

[51] Daniel, M. I. & Ishai, O. *Engineering Mechanics of Composite Materials* (Oxfored University Press, Inc., New York City, 2006), 2 edn.

[52] Thurner, P. J. *et al.* High-speed photography of compressed human trabecular bone correlates whitening to microscopic damage. *Engineering Fracture Mechanics* **74**, 1928–1941 (2007). URL http://linkinghub.elsevier.com/retrieve/pii/S0013794406002128.

[53] Lees, S., Prostak, K. S., Ingle, V. K. & Kjoller, K. The loci of mineral in turkey leg tendon as seen by atomic force microscope and electron microscopy. *Calcified Tissue International* **55**, 180–189 (1994).

[54] Nikolov, S. & Raabe, D. Hierarchical Modeling of the Elastic Properties of Bone at Submicron Scales : The Role of Extrafibrillar Mineralization. *Biophysical Journal* **94**, 4220–4232 (2008). URL http://dx.doi.org/10.1529/biophysj.107.125567.

[55] Nair, A. K., Gautieri, A., Chang, S.-W. & Buehler, M. J. Molecular mechanics of mineralized collagen fibrils in bone. *Nature Communications* **4**, 1724 (2013). URL http://www.nature.com/doifinder/10.1038/ncomms2720.

[56] Hamed, E., Jasiuk, I., Yoo, a., Lee, Y. & Liszka, T. Multi-scale modelling of elastic moduli of trabecular bone. *Journal of The Royal Society Interface* **9**, 1654–1673 (2012). URL http://www.pubmedcentral.nih.gov/articlerender.fcgi?artid=3367819&tool=pmcentrez&rendertype=abstract.

[57] Bonar, L. C., Lees, S. & Mook, H. A. Neutron diffraction studies of collagen in fully mineralized bone. *Journal of Molecular Biology* **181**, 265–270 (1985).

[58] Wenger, M. P. E., Bozec, L., Horton, M. A. & Mesquida, P. Mechanical properties of collagen fibrils. *Biophysical journal* **93**, 1255–63 (2007). URL http://www.pubmedcentral.nih.gov/articlerender.fcgi?artid=1929027&tool=pmcentrez&rendertype=abstract.

[59] Cusack, S. & Miller, A. Determination of the elastic constants of collagen by Brillouin light scattering. *Journal of Molecular Biology* **135**, 39–51 (1979).

[60] Li, S. X. *et al.* Maximum packing densities of basic 3D objects. *Chinese Science Bulletin* **55**, 114–119 (2010).

[61] Timoshenko, S. & Goodier, J. N. *Theory of Elasticity* (McGraw-Hill Book Company, New York City, 1970).

[62] Turner, C. H., Rho, J., Takano, Y., Tsui, T. Y. & Pharr, G. M. The elastic properties of trabecular and cortical bone tissues are similar: Results from two microscopic measurement techniques. *Journal of Biomechanics* **32**, 437–441 (1999). URL http://www.sciencedirect.com/science/article/pii/S0021929098001778.

[63] Inglis, C. E. Stresses in a plate due to the presnce of cracks and sharp corners (1913).

[64] Parthasarathy, T. a., Rao, S. I., Dimiduk, D. M., Uchic, M. D. & Trinkle, D. R. Contribution to size effect of yield strength from the stochastics of dislocation source lengths in finite samples. *Scripta Materialia* **56**, 313–316 (2007).

[65] Hansma, P. K. *et al.* Sacrificial bonds in the interfibrillar matrix of bone. *Journal of Musculoskeletal Neuronal Interactions* **5**, 313–315 (2005). URL http://www.ncbi.nlm.nih.gov/pubmed/16340118.

[66] Thompson, J. B. *et al.* Bone indentation recovery time correlates with bond reforming time. *Nature* **414**, 773–776 (2001). URL http://www.ncbi.nlm.nih.gov/pubmed/11742405.

[67] Currey, J. D. The structure and mechanics of bone. *Journal of Materials Science* **47**, 41–54 (2012).

[68] Nassif, N. *et al.* Self Assembled Collagen Apatite Matrix with Bone like Hierarchy. *Chemistry of Materials* **22**, 3307–3309 (2010). URL http://pubs.acs.org/doi/abs/10.1021/cm903594n.

[69] Currey, J. D. *Bones: Structure and Mechanics* (Princeton University Review, 1984).

[70] Peterlik, H., Roschger, P., Klaushofer, K. & Fratzl, P. From brittle to ductile fracture of bone. *Nature materials* **5**, 52–55 (2006). URL http://www.ncbi.nlm.nih.gov/pubmed/16341218.

[71] Launey, M. E., Chen, P. Y., McKittrick, J. & Ritchie, R. O. Mechanistic aspects of the fracture toughness of elk antler bone. *Acta Biomaterialia* **6**, 1505–1514 (2010). URL http://dx.doi.org/10.1016/j.actbio.2009.11.026.

[72] Uchic, M., Dimiduk, D. M., Florando, J. N. & Nix, W. D. Sample dimension influence strength and crystal plasticity. *Science* **305**, 986–989 (2004).

[73] Jaya, B. N. & Jayaram, V. Crack stability in edge-notched clamped beam specimens: Modeling and experiments. *International Journal of Fracture* **188**, 213–228 (2014).

[74] Jaya, B. N., Kirchlechner, C. & Dehm, G. Can microscale fracture tests provide reliable fracture toughness values? A case study in silicon. *Journal of Materials Research* **30**, 686–698 (2015). URL http://www.journals.cambridge.org/abstract_S0884291415000023.

[75] Li, V. C., Stang, H. & Krenchel, H. Micromechanics of crack bridging in fiber reinforced concrete. *Materials and Structures, 26* 486–494 (1993).

[76] ASTM. E 1820-15 Standard Test Method for Measurement of Fracture Toughness. *Annual Book of ASTM Standards* 1–56 (2015).

[77] Chen, C. P. & Leipold, M. H. Fracture Toughness of Silicon. *American Ceramic Society Bulletin* **59**, 469–472 (1980).

[78] Ritchie, R. O., Buehler, M. J. & Hansma, P. K. Plasticity and toughness in bone. *Physics Today* **62**, 41–47 (2009). URL http://www2.lbl.gov/ritchie/Library/PDF/PhysicsTodayJune2009.pdf.

[79] DelRio, F. W., Cook, R. F. & Boyce, B. L. Fracture strength of micro- and nano-scale silicon components. *Applied Physics Reviews* **2**, 021303 (2015). URL http://aip.scitation.org/doi/10.1063/1.4919540.

[80] Wright, W. J., Maloney, A. R. & Nix, W. D. An improved analysis for viscoelastic damping in dynamic nanoindentation. *International Journal of Surface Science and Engineering* **1**, 274 (2007).

[81] Norden, B. N. On the compression of a cylinder in contact with a plane surface. *Interagency Report* 73–243 (1973).

[82] Hopcroft, M. A., Nix, W. D. & Kenny, T. W. What is the Young ' s Modulus of Silicon ? *Journal of Microelctromechanical Systems* **19**, 229–238 (2010).

[83] Fitzgerald, A., Dauskardt, R. & Kenny, T. Fracture toughness and crack growth phenomena of plasma-etched single crystal silicon. *Sensors and Actuators A: Physical* **83**, 194–199 (2000). URL `http://linkinghub.elsevier.com/retrieve/pii/S0924424799003830`.

[84] Tsai, Y. L. & Mecholsky, J. J. Fractal fracture of single crystal silicon. *Journal of Materials Research* **6**, 1248–1263 (1991).

[85] Creager, M. & Paris, P. C. Elastic field equations for blunt cracks with reference to stress corrosion cracking. *International Journal of Fracture Mechanics* **3**, 247–252 (1967).

[86] Gómez, F. J. & Elices, M. A fracture criterion for blunted V-notched samples. *International Journal of Fracture* **127**, 239–264 (2004).

[87] Reznikov, N., Bilton, M., Lari, L., Stevens, M. M. & Kröger, R. Fractal-like hierarchical organization of bone begins at the nanoscale. *Science* **360** (2018).

[88] Ritchie, R. O., Knott, J. F. & Rice, J. R. On the relationship between critical tensile stress and fracture toughness in mild steel. *Journal of the Mechanics and Physics of Solids* **21**, 395–410 (1973).

[89] Weibull, W. Wide applicability. *Journal of applied mechanics* **103**, 293–297 (1951).

[90] Khandaker, M. & Ekwaro-Osire, S. Weibull analysis of fracture test data on bovine cortical bone: Influence of orientation. *International Journal of Biomaterials* **2013** (2013).

[91] Pithioux, M., Subit, D. & Chabrand, P. Comparison of compact bone failure under two different loading rates: Experimental and modelling approaches. *Medical Engineering and Physics* **26**, 647–653 (2004).

[92] Novitskaya, E. *et al.* Anisotropy in the compressive mechanical properties of bovine cortical bone and the mineral and protein constituents. *Acta Biomaterialia* **7**, 3170–3177 (2011). URL `http://dx.doi.org/10.1016/j.actbio.2011.04.025`.

[93] Budiansky, B., Hutchinson, J. W., Evans, A. G., Budiansky, B. & Evans, A. G. Matrix Fracture in Faber-Reinforces. *J. Mech. Phys. Solids* **34**, 167–189 (1986).

[94] Nishida, T., Hanaki, T. & Pezzotti, G. Effect of root notch radius on the fracture toughness of a fine-grained alumina. *J. Am. Ceram. Soc.* **77**, 606–608 (1994).

[95] Nalla, R. K., Kinney, J. H. & Ritchie, R. O. Mechanistic fracture criteria for the failure of human cortical bone. *Nature Materials* **2**, 164–168 (2003).

[96] Nalla, R. K. *et al.* Ultrastructural examination of dentin using focused ion-beam cross-sectioning and transmission electron microscopy. *Micron* **36**, 672–680 (2005).

[97] Acevedo, C., Stadelmann, V. A., Pioletti, D. P., Alliston, T. & Ritchie, R. O. Fatigue as the missing link between bone fragility and fracture. *Nature Biomedical Engineering* **2**, 62–71 (2018). URL http://dx.doi.org/10.1038/s41551-017-0183-9.

[98] Launey, M. E., Buehler, M. J. & Ritchie, R. O. On the Mechanistic Origins of Toughness in Bone. *Annual Review of Materials Research* **40**, 25–53 (2010). URL http://www.annualreviews.org/doi/10.1146/annurev-matsci-070909-104427.

[99] Haggag, F. M. & Underwood, J. H. Compliance of a three-point bend specimen at load line. *International Journal of Fracture* **26** (1984).

[100] Kim, J.-k. & Mai, Y.-W. High strength, high fracture toughness fibre composites with interface control - a review. *Composite Science and Technology* **41**, 333–378 (1991).

[101] Bao, G. & Suo, Z. Remarks on Crack-Bridging Concepts. *Applied Mechanics Reviews* **45**, 355 (1992). URL http://appliedmechanicsreviews.asmedigitalcollection.asme.org/article.aspx?articleid=1394654.

[102] Li, V. C., Chan, C.-M. & Leung, C. K. Experimental determination of the tension-softening relations for cementitious composites. *Cement and Concrete Research* **17**, 441–452 (1987). URL http://linkinghub.elsevier.com/retrieve/pii/0008884687900081.

[103] Elices, M., Guinea, G. V., Gómez, F. & Planas, J. The cohesive zone model: advantages, limitations and challenges. *Engineering Fracture Mechanics* **69**, 137–163 (2002). URL http://linkinghub.elsevier.com/retrieve/pii/S0013794401000832.

[104] Li, V. Postcrack Scaling Relations for Fiber Reinforced Cementitious Composites. *Journal of Materials in Civil Engineering* **4**, 41–57 (1992). URL http://ascelibrary.org/doi/10.1061/%28ASCE%290899-1561%281992%294%3A1%2841%29.

[105] Fratzl, P. & Weinkamer, R. Nature's hierarchical materials. *Progress in Materials Science* **52**, 1263–1334 (2007). URL http://linkinghub.elsevier.com/retrieve/pii/S007964250700045Xhttp://www.sciencedirect.com/science/article/pii/S007964250700045X.

[106] Eldridge, J. J. *et al.* Greatly Increased Toughness of Infiltrated Spider Silk. *Science* **324**, 488–493 (2012). URL http://science.sciencemag.org/content/324/5926/488.

[107] Pan, X.-f. *et al.* Transforming ground mica into high-performance biomimetic polymeric mica film. *Nature Communications* **9**, 1–8. URL https://www.nature.com/articles/s41467-018-05355-6http://dx.doi.org/10.1038/s41467-018-05355-6.

Appendix A

POROSITY ADJUSTED PARAMETERS FOR ELASTIC COMPOSITE MODELS

Re-adjusted (adj) volume fractions to account for ϕ_{flaws}^{EFM}. These are the values reported in Table 3.5 without the "adj" added for simplicity.

$$\phi_{Min,adj} = \phi_{Min}\left(\phi_{IF}^{Min} + \phi_{EF}^{Min}\left(1 - \phi_{flaws}^{EFM}\right)\right)$$

$$\phi_{EF}^{Min,adj} = \frac{\phi_{EF}^{Min}\left(1 - \phi_{flaws}^{EFM}\right)}{\phi_{Min}^{adj}}$$

$$\phi_{IF}^{Min,adj} = 1 - \phi_{EF}^{Min,adj}$$

$$\phi_{Min,adj}^{EFM} = \phi_{Min}^{EFM}\left(1 - \phi_{flaws}^{EFM}\right)$$

$$\phi_{NCP,adj}^{EFM} = 1 - \phi_{Min,adj}^{EFM} - \phi_{flaws}^{EFM}$$

$$\phi_{NCP,adj} = \phi_{NCP,adj}^{EFM}\phi_{EFM}$$

Appendix B

ETCHING OF SILICON FOR MICROSCALE FRACTURE EXPERIMENTS

The etching of the silicon structures in this thesis was accomplished in the Kavli Nanoscience Institute. This refers to 1) the supports that hold the specimens and 2) the silicon specimens.

Supports

The masks for the supports are fabricated by using a 2 photon lithography system (Nanoscribe Gmbh) to create 2x2x2 μm polymer masks that create each individual support. Two of these are spaced 40 μm apart with a third sacrificial support 2 μm from one of these. The 40 μm determines the span of during the fracture experiment thus the spacing can be adjusted for differently sized specimens. The supports are etched in a reactive ion etcher (RIE) at 10 mT and 20 sccm of SF_6 for about 17 mins. This produces a tapered support profile. Figure B.1 shows the process of etching multiple silicon supports from a mask array of span and support dimensions (Fig B.1a) to the support profile (Fig B.1b) and the resulting supports of different dimensions (Fig B.1c,d). If taller, straighter supports are desired (as seen in Supplementary Video 5), the etching can be done in a more controlled deep reactive ion etcher (DRIE). This is the process employed for etching the silicon beams and will be described next.

Si Beams

The masks for the silicon beams are fabricated using e-beam lithography in the nano-pattern generation system (NPGS) on the Quanta. A two layer PMMA recipe (courtesy of Dagny Fleischman) is employed as follows:

- 3 min acetone wafer clean
- 3 min methenol wafer clean
- 180^o c hot plate (2-5 min)
- cool for 1 min
- spin 495 A4 PMMA at 3500 RPM (1 min)
  - gives ~ 195 nm per Filmetrics measurement
  - 5 min hot plate at 180^o C

  - cool 1 min

- spin 950 A2 PMMA at 3500 RPM
  - 5 min hot plate at 180^{o} C
  - cool 1 min

The resist is patterned using the NPGS with doses ranging from 500 to 750 $\mu c/cm^2$. Next the resist is developed in a room temperature solution of 1 to 3, methyl isobutyl ketone to isopropanol (1:3 MIBK:IPA) for 45 seconds. The development is arrested by placing the wafer in IPA for 30 seconds. We deposit 100 nm of alumina into the pattern using e-beam evaporation (TES Evaporator). Note that it is important to monitor the temperature increase in the chamber when depositing ceramics. If the temperature rises above the glass transition of the resist, the pattern will be damaged.

Following deposition, liftoff of the sacrificial PMMA and alumina layer is accomplished by placing the wafer in acetone overnight. A couple of hours can be sufficient. Placing the sample vertically in the acetone bath can considerably improve liftoff quality by preventing redeposition of alumina that are flakes floating in solution back onto the wafer. For similar reasons, it is also highly recommended to remove the wafer from acetone liftoff bath with the etched surface facing down towards the

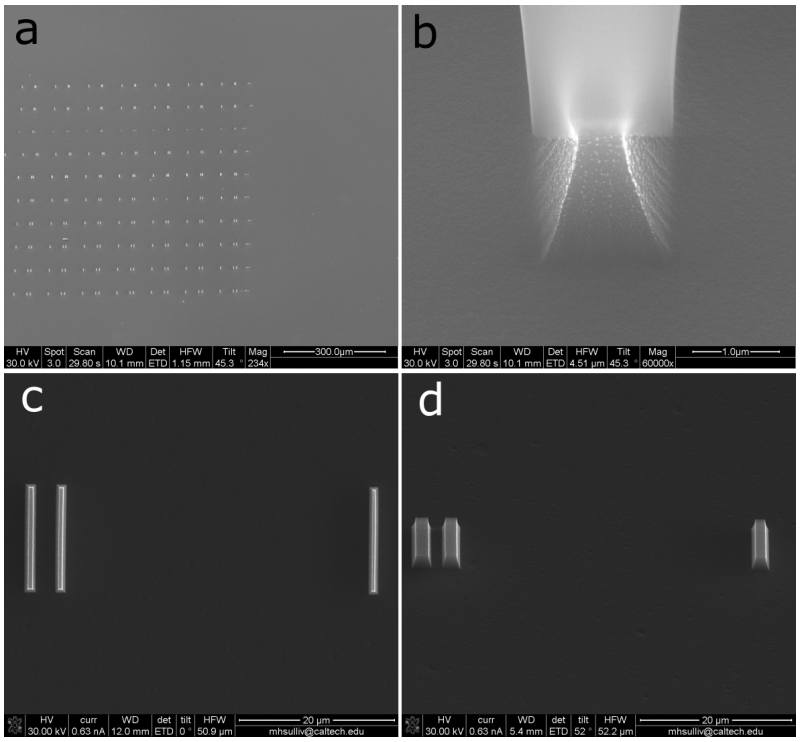

Figure B.1: Etching of 3-point bend supports

bottom of the container (beaker, petri dish, etc...). The sample is next rinsed in an new acetone bath, followed by an isopropanol bath.

The results of the masking process are shown in the top images of Figures B.2a,b. Figure B.2a shows a mask created from a single PMMA 950 A2 spin while Figure B.2b shows a mask from the dual resist procedure described above. We observe a significant improvement in roughness of the edges of the mask by employing a dual resist procedure.

To etch the beams we employ a pseudo-Bosch process in the Oxford III-V DRIE. This involves simultaneously flowing SF_6 to chemically etch and C_4F_8 to protect the silicon. Tunning the ratio of the gases allows control of the profile of the etch. Here we run 22/35 sccm of SF_6/C_4F_8. The capacitively coupled power (or "direct power") is set to 22 W and the inductive power is set to 1250 W. The etch rate with these conditions is $\sim$ 250 nm/min. The results of the etching on the to alumina masks are shown in the bottom images of Figures B.2a and b. The roughness of the mask is transferred onto the walls of the structures; this shows the dual resist process yields smoother structures.

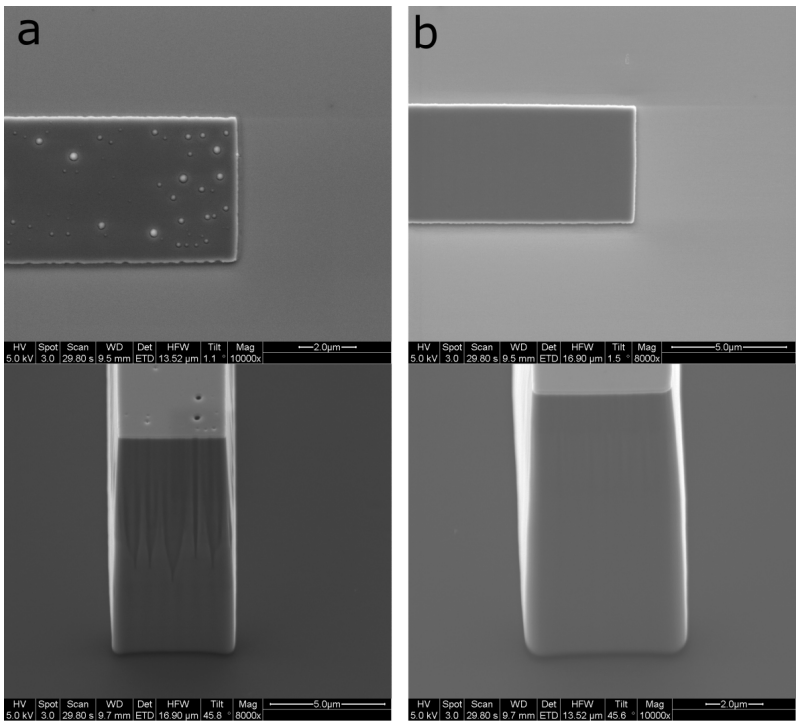

Figure B.2: Si Beam Masks

Appendix C

POWER-LAW FITTING OF TOUGHNESS

The effective toughness during crack growth denoted as K_J is calculated back from the J-integral using the linear elastic relation $K_J = (JE)^{1/2}$ [8]. This allows for comparison with other toughness values reported for bone in literature. For metals J-integral can be fit to a power-law with respect to the crack extension. In macroscopic experiments this power law fit is generally given by

$$J = C_1 \left(\frac{\Delta a}{k} \right)^{c_2} \tag{C.1}$$

where the C terms are fitting parameters and k is prescribed as 1 mm [76]. This power law is employed to gain a functional form with which to determine a crack tip blunting line and thus an effective J_C. However, that is not mechanistically relevant in the present experiments. In the present context, for simplicity, we absorb the k^{-c_2} constant into the C_1 parameter and rewrite the fit function as

$$J = \alpha \Delta a^{\beta} \tag{C.2}$$

Considering the relation between J and K_J, we can write the power law fit or K_J as

$$\begin{aligned} K_J &= \left(\alpha \Delta a^{\beta} E' \right)^{1/2} \\ &= \alpha_K \Delta a^{\beta_k} \end{aligned} \tag{C.3}$$

where $\alpha_K = (\alpha E')^{1/2}$ and $\beta_K = \beta/2$. The results of the fit are show in Figure 4 in the main text.

Appendix D

LEGEND OF SUPPLEMENTAL VIDEOS

Supplemental Video 1
Pillar fabrication via FIB

Supplemental Video 2
Cross Sections of post-mortem pillar to identify micro structural origin of failure

Supplemental Video 3
Tomographic sections of disordered bone for model parameters in Chapter 3

Supplemental Video 4
Fracture of silicon specimen

Supplemental Video 5
Fracture of notched bone specimen

Supplemental Video 6
Fracture of precracked bone specimen

Supplemental Video 7
Tracking crack mouth opening in precracked specimen